Ab initio molecular dynamics study on the influence of water on methanol conversion in H-SAPO-34

Simon Bailleul

Supervisors: Prof. dr. ir. Veronique Van Speybroeck, Prof. dr. ir. Karen Hemelsoet
Counsellors: Kristof De Wispelaere, Jeroen Van der Mynsbrugge

Master's dissertation submitted in order to obtain the academic degree of
Master of Science in Chemical Engineering

Department of Applied Physics
Chairman: Prof. dr. ir. Christophe Leys
Faculty of Engineering and Architecture
Academic year 2014-2015

UNIVERSITEIT
GENT

Center for
Molecular Modeling

This research was conducted at the Center for Molecular Modeling.

Preface

You can never write a thesis on your own, therefore I would like to express my gratitude to the people who helped.

Firstly, I would like to thank both of my supervisors, prof. dr. ir. Veronique Van Speybroeck and prof. dr. ir. Karen Hemelsoet, for the given opportunity to conduct this research at the Center for Molecular Modeling. They were always prepared to provide personal advice and guidance. Furthermore, I would like to thank them for the opportunity to join the NCCC at Noordwijkerhout, where I got to present the results of my research. This was a unique and instructive experience.

I like to express particular gratitude to Kristof and Jeroen, who were always available for assistance and helped to overcome every possible barrier. Without their help, this project would have never ended successfully.

Furthermore, I would like to thank all employees of the CMM for the great atmosphere and the help in solving the encountered problems.

Subsequently, I would like to thank my friends. Especially, Bavo and Margot, who also did their thesis at the CMM and helped crushing every obstacle that came across.

Lastly, I would like to thank my family for their support during this challenging time. Furthermore, I would like to thank them for the opportunities given to me during my entire life.

Simon Bailleul
Gent, 22 mei 2015

Simon Bailleul
Gent, 22 mei 2015

Ab initio molecular dynamics study on the influence of water on methanol conversion in H-SAPO-34

Simon Bailleul

Master's dissertation submitted in order to obtain the academic degree of
Master of Science in Chemical Engineering
Academic year 2014–2015
Supervisors: prof. dr. ir. Veronique Van Speybroeck, prof. dr. ir. Karen Hemelsoet
Counsellors: ir. Kristof De Wispelaere, dr. ir. Jeroen Van der Mynsbrugge

Faculty of Engineering and Architecture – Ghent University

Center for Molecular Modeling

Abstract

Due to the growing relevance of renewable resources, interest in the methanol-to-olefin (MTO) process has grown since it is one of the most prominent technologies to bypass crude oil in the production of light olefins. Studies on the reaction mechanism governing this MTO process have been ongoing for years. Nowadays, reaction mechanisms based on hydrocarbon pool (HP) species that co-catalyze the reactions have been generally accepted for the olefin production via the MTO process. H-SAPO-34 is an important industrial catalyst for this process, due to its high selectivity to light olefins. Two main mechanisms based on hexamethylbenzene as a HP species have been proposed for the production of olefins in H-SAPO-34, namely the paring and side-chain mechanism. Water has an important influence on the MTO process, since it is a byproduct of both the methanol synthesis and the MTO process. The addition of water to the methanol feed is known to reduce the rate of coke formation and maximize selectivity to light olefins. In this thesis, the influence of water on the framework flexibility, proton mobility and stability of the aromatic intermediates of the side-chain mechanism is investigated in H-SAPO-34 by means of ab initio molecular dynamics simulations. Furthermore, the dependence of the free energy barrier of the reactions of the side-chain cycle on the water loading is investigated via metadynamics simulations.

Keywords: MTO, ab initio molecular dynamics, metadynamics, side-chain mechanism, water

Ab initio molecular dynamics study on the influence of water on methanol conversion in H-SAPO-34

Simon Bailleul

Supervisors: prof. dr. ir. Veronique Van Speybroeck, prof. dr. ir. Karen Hemelsoet
Counsellors: ir. Kristof De Wispelaere, dr. ir. Jeroen Van der Mynsbrugge

Abstract— **Due to the growing relevance of renewable resources, interest in the methanol-to-olefin (MTO) process has grown since it is one of the most prominent technologies to bypass crude oil in the production of light olefins. Studies on the reaction mechanism governing this MTO process have been ongoing for years. Nowadays, reaction mechanisms based on hydrocarbon pool (HP) species that co-catalyze the reactions have been generally accepted for the olefin production via the MTO process. H-SAPO-34 is an important industrial catalyst for this process, due to its high selectivity to light olefins. Two main mechanisms based on hexamethylbenzene as a HP species have been proposed for the production of olefins in H-SAPO-34, namely the paring and side-chain mechanism. Water has an important influence on the MTO process, since it is a byproduct of both the methanol synthesis and the MTO process. The addition of water to the methanol feed is known to reduce the rate of coke formation and maximize selectivity to light olefins. In this thesis, the influence of water on the framework flexibility, proton mobility and stability of the aromatic intermediates of the side-chain mechanism is investigated in H-SAPO-34 by means of ab initio molecular dynamics simulations. Furthermore, the dependence of the free energy barrier of the reactions of the side-chain cycle on the water loading is investigated via metadynamics simulations.**

Keywords— **MTO, ab initio molecular dynamics, metadynamics, side-chain mechanism, water**

I. INTRODUCTION

DUE to depleting oil reserves and the increasing demand for base chemicals such as ethylene and propylene, the search for processes based on alternative feedstock is an active research area from an industrial and academic perspective. Interesting alternative routes are those starting from methanol, because it can be produced from any gasifiable carbon-rich feedstock. In the methanol-to-olefin (MTO) process, methanol is transformed into valuable base chemicals. The chabazite-structured H-SAPO-34 catalyst is of particular industrial interest as it shows a high selectivity to light olefins.[1]

Studies on the reaction mechanism governing the complex MTO process have been ongoing for years. Various experimental techniques have been used to unravel the mechanism, but due to the large number of reactions that take place simultaneously, it is difficult to get insights into individual reaction steps. These limitations can be overcome by theoretical simulations, since these are capable to accurately predict the adsorption and reactivity of crucial reaction intermediates.[2] The combination of experimental and theoretical research resulted in the general acceptance of the hydrocarbon pool mechanism governing the MTO process. Herein, an organic compound is trapped in the catalyst framework and acts as a co-catalyst. In H-SAPO-34 and H-SSZ-13, which both exhibit the chabazite topology, polymethylbenzenes have been identified as the dominant HP species.[3] Based on these aromatic intermediates two reaction cycles are proposed, namely the side-chain and paring mechanism, depicted in Figure 1.

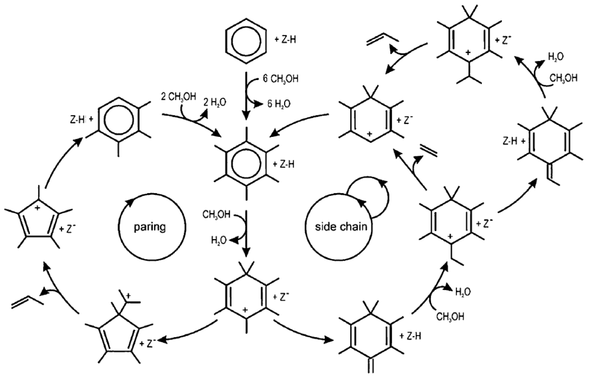

Fig. 1: The proposed side-chain and paring mechanism for ethylene and propylene formation starting from hexamethylbenzene (HMB).[4]

Recently, a low-barrier side-chain cycle for ethylene and propylene formation in H-SAPO-34 was found based on a first principle kinetic study with hexamethylbenzene (HMB) as a co-catalyst. The olefin elimination steps, which were found to be the main bottleneck in earlier theoretical studies [4, 5], exhibit low free energy barriers due to a subtle interplay between an sp^3 carbon center of the organic intermediate, stabilizing non-bonding interactions and assisting water molecules.[6]

Water is an important byproduct of both the methanol production and the MTO process itself. Experimental research has shown that the addition of water to the feed leads to a reduced

---

S. Bailleul is with the Center for Molecular Modeling, Ghent University (UGent), Gent, Belgium. E-mail: Simon.Bailleul@UGent.be.

coking rate and maximized selectivity to light olefins. An optimal water to methanol molar ratio around 3-4 has been reported.[7] However, to date the influence of water on the overall MTO reaction mechanism is still poorly understood.

In this dissertation the influence of water on elementary steps in the MTO process is investigated on a molecular level via theoretical calculations. Firstly, the effect of water on the mobility and stability of the aromatic intermediates in the proposed side-chain cycle for ethylene formation (listed in Table I) is assessed via ab initio molecular dynamics (AIMD) simulations. Subsequently, the dependence of the free energy barriers between the intermediates on the water content of the catalyst is evaluated by means of metadynamics (MTD) simulations.

TABLE I: Abbreviations used for the intermediates of the side-chain mechanism.

Abbreviation	**Description**
HMB	hexamethylbenzene
heptaMB^{+}	heptamethylbenzenium cation
HMMC	1,2,3,3,4,5-hexamethyl-6-methylene-1,4-cyclohexadiene
R$_{JMe1}$	Reactant of the first methyl jump
R$_{JMe2}$	Reactant of the second methyl jump
R$_{JMe3}$	Reactant of the third methyl jump
R$_{EthEli}$	Reactant of the ethylene elimination

II. THEORETICAL METHODS

Simulations are performed with the CP2K simulation package using the revised PBE functional with additional Grimme D3 dispersion corrections, combined with the DZVP-GTH basis set. The calculations are applied to a fully periodic catalyst model. For the simulations use is made of an H-SAPO-34 unit cell containing 110 atoms. The catalyst framework is activated by the introduction of two Si substitutional defects and charge compensating protons, leading to two Brønsted acid sites (BAS) per unit cell.

To analyze the stability and mobility of the aromatic intermediates in the side-chain mechanism, ab initio molecular dynamics simulations are used. Dynamic simulations have the advantage of accounting for temperature effects, entropic effects and the influence of surrounding solvent molecules, in contrast to static calculations. The simulations are performed in the NPT ensemble at 623 K and 1 atm. The system is equilibrated for 1.25 ps using the canonical sampling with velocity rescaling (CSVR) algorithm. These simulations are subsequently followed by a production run of 50 ps in which the temperature is controlled by a chain of five Nosé -Hoover thermostats and the pressure by an MTK barostat.

To examine the free energy barriers in the side-chain cycle metadynamics simulations are performed. These simulations are started from the equilibrated systems obtained from the 50 ps AIMD production runs. The MTD simulations are performed in the NVT ensemble at 623 K. The temperature is again controlled by a chain of five Nosé -Hoover thermostats.

III. RESULTS AND DISCUSSION

The influence of water on the stability and mobility of the aromatic intermediates is assessed via the analysis of several phenomena, namely the framework flexibility, the behavior of the aromatic intermediate in the chabazite cage, the deprotonation probability of the framework and the relative stability of the intermediates.

The analysis of the framework flexibility of H-SAPO-34 is started by assessing the influence of the addition of molecules to the catalyst pores on the unit cell parameters and volume. For this AIMD simulations of HMB in the four cases given in Table II are compared.

TABLE II: The four loadings considered to unravel the influence of water on the MTO reactions.

Name	Initial loading (aromatic:methanol:water)
Case 1: reference	1:0:0
Case 2: no water content	1:1:0
Case 3: low water content	1:2:1
Case 4: high water content	1:2:9

The resulting unit cell parameter and volume changes compared to an empty unit cell are depicted in Figure 2. The introduction of HMB in the catalyst framework induces a volume expansion of 4 % compared to the empty unit cell. A subsequent addition of a methanol molecule leads to an extra expansion of 0.2 %. In contrast, the addition of eight water molecules leads to a contraction of the unit cell volume of 1.2 %. When looking at the corresponding changes in the unit cell parameters, the volume variations are found to be anisotropic, since the main changes are along the c-axis. These asymmetric unit cell variations might be because the more flexible 8-ring windows are directed parallel to the c-axis, while the more rigid 6-ring windows are perpendicular to this axis. These results are in line with the experimental XRD results of Wragg et al.[8]

Subsequently, the influence of the unit cell contraction due to water adsorption on the behavior of the aromatic intermediates

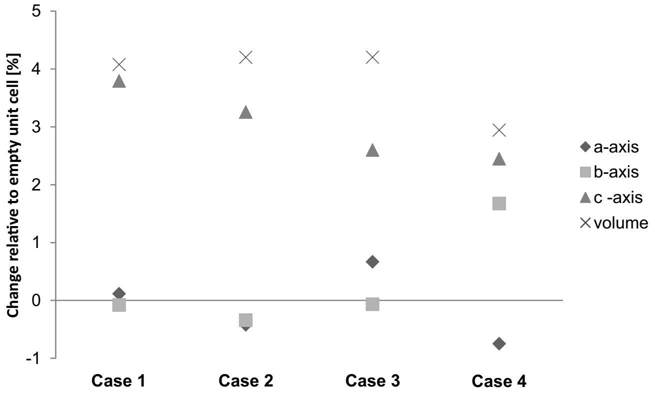

Fig. 2: Average variation of the unit cell parameters and volume, relative to an empty H-SAPO-34 unit cell, over the 50 ps production run, at 623 K and 1 atm, of HMB.

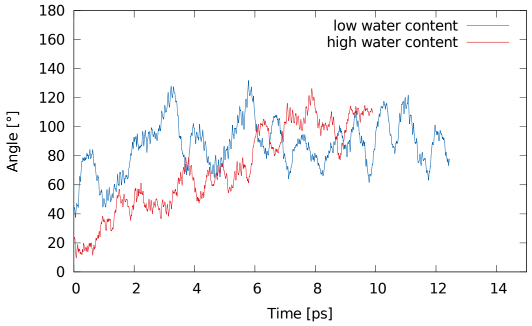

Fig. 4: Angle between the normal of the plane of the aromatic ring and the normal of the plane of the catalyst framework indicated in Figure 3, as function of time for the AIMD simulation of heptaMB$^+$ at 623 K and 1 atm in the H-SAPO-34 framework.

is evaluated. All intermediates of the side-chain mechanism are found to rotate during the AIMD simulations to take advantage of the full length of the chabazite cage. Therefore, it might be interesting to analyze the dependence of this tendency to rotate on the water loading. The rotation can be quantified by following the angle between the two vectors depicted in Figure 3.

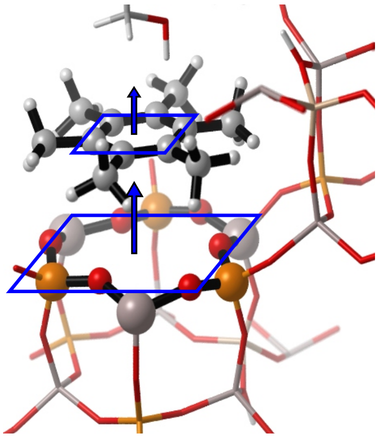

Fig. 3: Representation of both normal vectors used in the analysis of the rotation of the aromatic species.

The result for the rotation of heptaMB$^+$ is shown in Figure 4. Similar results are obtained for the other intermediates, suggesting that there is no direct influence of the higher water loading on the rotation of the aromatic intermediates.

The BAS is an important characteristic of the MTO catalyst.[9] High methanol or water loadings are known to be able to deprotonate the BAS.[10] Therefore, the influence of water on the probability for the framework to deprotonate is analyzed. These probabilities are depicted in Figure 5. First of all, it should be noted that no 50 ps production runs for HMMC are available, since HMMC is protonated to form heptaMB$^+$ during the AIMD simulations. This suggests that HMMC is an unstable intermediate at the simulated reaction conditions. The obtained results show a clear difference between HMB and the cationic intermediates, because one BAS is consumed during the formation of the cationic intermediate, at most one BAS remains in the simulations of the cationic intermediates. Furthermore, an increase of the water content clearly leads to an increase of the probability for framework deprotonation. Two simulations are found to deviate, namely R$_{JMe1}$ at low water content and R$_{JMe2}$ at high water content. In these simulations the BAS is blocked by the aromatic intermediate, making deprotonation impossible.

Additionally, the influence of the water loading on the probability to protonate methanol is considered for the simulation of HMB, since water and methanol, which needs to be protonated for the methylation reaction[11], are found to adsorb competitively. The results are depicted in Figure 6, showing a clear decrease of methanol protonation at higher water loading.

Before calculating the free energy barriers for the reactions in the side-chain cycle, it is instructive to inspect the relative stability of the intermediates. This can be done based on the average potential energies of the aromatic intermediates obtained via the AIMD simulations relative to the corresponding simulation of HMB. These are depicted in Figure 7 together with the enthalpy obtained via the static calculations reported by De Wispelaere et al.[6] Comparison of the dynamic with the static results shows a significant difference: the static results suggest a destabilization of the cationic intermediates compared to HMB, while the dynamic results suggest the opposite. Furthermore, the addition of eight water molecules to the unit cell is found to destabilize

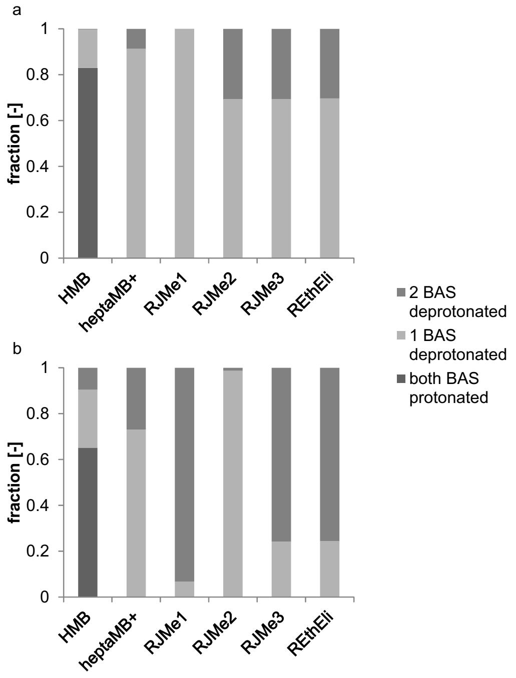

Fig. 5: Fraction of the 50 ps AIMD simulation at 623 K and 1 atm in which the Brønsted acid sites of the H-SAPO-34 framework are (de)protonated for low water content (a) and high water content (b).

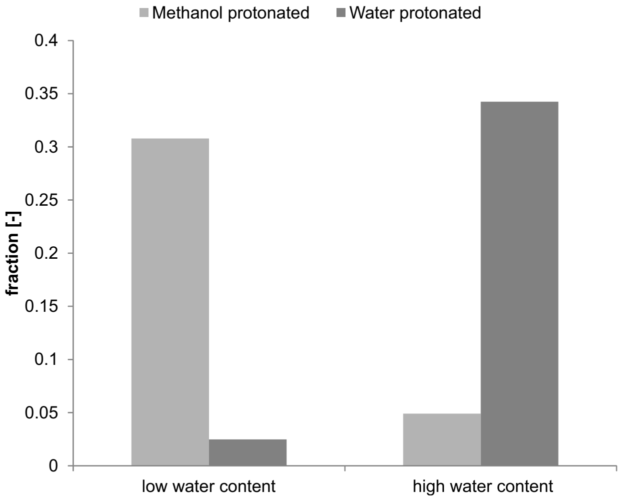

Fig. 6: Fraction of time in the AIMD simulation of HMB at 623 K and 1 atm for which methanol and water are protonated at low and high water content.

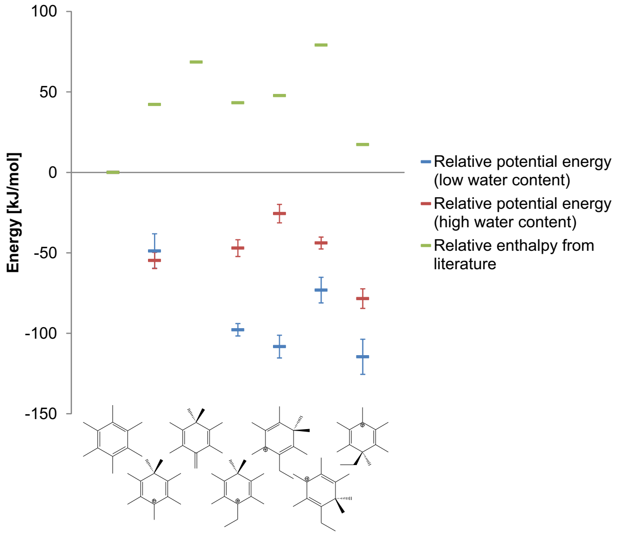

Fig. 7: Average potential energy of the different intermediates relative to HMB for the low and high water content case combined with the enthalpy from literature.[6] The average potential energies are taken over the 50 ps AIMD simulations at 623 K and 1 atm. The static calculations from literature were executed with the B3LYP functional in an extended cluster with one BAS.[6]

the cationic intermediates, except for heptaMB$^+$.

Subsequently, the influence of water on the free energy barriers between the aromatic intermediates is determined based on the results of the metadynamics simulations. Furthermore, the dependence of the competition between the side-chain mechanism and the paring mechanism on the water loading is analyzed by additionally considering the free energy barrier for the onset reaction of the paring mechanism.

The first reaction in both the side-chain and the paring mechanism is the methylation of HMB, to form heptaMB$^+$. The free energy barrier obtained via the MTD simulations is found to decrease from 91 kJ/mol with no water loading, via 82 kJ/mol at low water content, to 72 kJ/mol at high water loading. This reduction in the barrier might be because methanol is kept protonated during the methylation reaction and protonated methanol is destabilized at higher water content, as shown in Figure 6. This destabilization increases the energy of the reactant state, which might explain the decrease of the barrier. Since two mechanisms are suggested for the methylation reaction, namely concerted and stepwise, competition between both can be evaluated via simulations in which the mechanism is not imposed. Therefore, additional simulations have been executed with three collective variables to take the formation of methoxide species into account, which is the intermediate in the stepwise mechanism. Though the simulations have not yet completely converged, the available results suggest the methoxide species as a viable intermediate and thus the stepwise mechanism as possible methylation route.

In the subsequent reaction the side-chain and paring mechanism differ. While a deprotonation of heptaMB$^+$ occurs in the side-chain mechanism, a ring contraction takes place in the paring mechanism. For the deprotonation of heptaMB$^+$ a reduction of the free energy barrier from 91 kJ/mol at low water content to 77 kJ/mol at high water content is found, which might be due to the stabilization of the formed H_3O^+ by formation of a water cluster with the additional water, as can be seen in Figure 8.

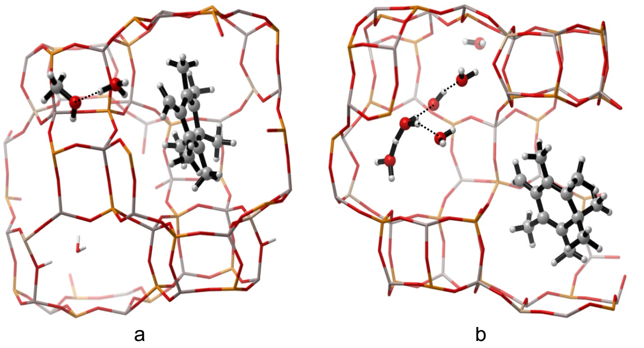

Fig. 8: Snapshot of the product state in the MTD simulation of the deprotonation of heptaMB$^+$ at 623 at low (a) and high (b) water content, showing the behavior of the formed H_3O^+. At low water content, H_3O^+ is only stabilized by one methanol, while at high water content a water cluster is formed.

The competing reaction of the paring mechanism is the ring contraction of heptaMB$^+$, which is suggested to be a two step reaction. First, the 6-ring contracts to form a 3- and 5-ring. Subsequently, one of the bonds of the 3-ring breaks, forming a isopropyl side chain on the 5-ring. Only the first step is considered in the calculation of the free energy barrier, though some interference of the second reaction step is found in the 1D simulations which possibly led to a spurious decrease of the reaction barrier at high water content. Nevertheless, an estimate of the forward free energy barrier could be obtained from the 2D simulations at high water content. Here, a barrier of 124 kJ/mol is found, which is high compared to the 77 kJ/mol barrier of the competing deprotonation of heptaMB$^+$, suggesting the side-chain mechanism as the prevailing cycle in H-SAPO-34.

Subsequently, the free energy barrier of the following reaction in the side-chain mechanism is discussed, which is the methylation of HMMC. The influence of water on this reaction could not be determined, since results at high water content are not yet obtained. Nevertheless, the competition between a stepwise and concerted methylation can be discussed, since both methylation with methanol and a methoxide species are sampled. Both reactions exhibit a similar free energy barrier, namely 34 kJ/mol for methanol and 38 kJ/mol for the methoxide species, which again suggests that the methoxide species can be a viable intermediate. Furthermore, the low free energy barriers confirm the instability of HMMC at the simulated conditions.

Next in the side-chain cycle, the gem-methyl group (in para position with respect to the ethyl group) migrates via three methyl jumps to the ethyl group, weakening the C-C bond that breaks in the subsequent reaction. The free energy barriers of the reaction and the relative stability of the intermediates are found to change by the addition of water, though a direct (de)stabilization is not found, since the water molecules do not diffuse into the cage where the aromatic intermediate reacts.

Lastly, the ethylene elimination reaction is considered. The three characteristics for a low barrier proposed by De Wispelaere et al.[6] are analyzed. The three suggested features, depicted in Figure 9, are (1) an sp^3 carbon center of the organic intermediate weakening the breaking C-C bond, (2) stabilizing non-bonding interactions forming an alkylbenzene-like complex and (3) assisting water molecules. Characteristic (1) and (2) are examined by comparing the results of the AIMD simulations of R_{JMe1} and R_{EthEli}. For the first characteristic, the average length of the breaking C-C bond is calculated. For R_{JMe1} an average bond length of 1.51 ± 0.05 Å is found for both low and high water content, while an average bond length of 1.62 ± 0.08 Å is found for R_{EthEli} at both water loadings. These results clearly show a weakening of the C-C bond due to sp^3 hybridization.

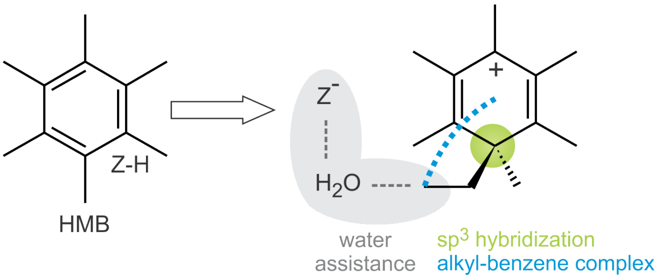

Fig. 9: Representation of the conditions for a low barrier for olefin elimination found by De Wispelaere et al.[6]

To evaluate the second characteristic, the dihedral angles between C1, C2, C3 and C4 depicted in Figure 10 is considered for both reactants. The results show that while the dihedral angle of R_{JMe1} can vary from -180° to 180°, the angle for R_{EthEli} remains between -50° and 50°. This limitation of the dihedral angle corresponds with an orientation of the ethyl group to the aromatic ring, in agreement with the characteristic necessary for the low free energy barrier.

The last feature, the assistance of water, could be evaluated by comparing the free energy barrier at low and high water content. Unfortunately, an ethyl adsorbed at the BAS is found as a stable

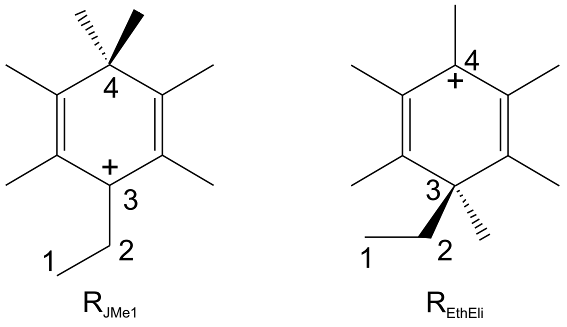

Fig. 10: Representation of the dihedral angles which are analyzed to see the formation of the alkylbenzene-like complex.

intermediate at low water content, which leads to an unphysical decrease of the free energy barrier. Nevertheless, an estimate of the barrier can be obtained from the free energy profile after the first crossing, before the adsorbed ethyl is encountered. This leads to a barrier of 141 kJ/mol. At high water content, the ethyl intermediate is not found and the barrier can be calculated from more converged results. The obtained barrier of 116 kJ/mol is clearly lower than at low water content. This decrease is not attributed to a water assistance, rather the loss of orientation between the ethyl chain and the aromatic ring at low water content is suggested to increase the barrier.

IV. Conclusion

This ab initio molecular dynamics study shows the influence of water on the reaction mechanism governing the MTO process. Due to the loading of water in the H-SAPO-34 environment, a contraction of the framework is found. This contraction is not found to have an influence on the mobility of the aromatic intermediate in the catalyst cage. In contrast, the increased water content leads to proton mobility, leading to a higher framework deprotonation probability. Furthermore, a decreased probability for the formation of protonated methanol is found, which might lead to a delay in the methylation of HMB. On the other hand, water stabilizes H_3O^+ formed during the deprotonation of heptaMB$^+$, leading to a decreased free energy barrier and thus possible increased rate for this reaction. Water therefore has both promoting and delaying effects. Finally, the results confirm the static calculations, since all free energy barriers are sufficiently low, and provide complementary insights due to the dynamic approach.

Acknowledgments

The computational resources (Stevin Supercomputer Infrastructure) and services used in this work were provided by the VSC (Flemish Supercomputer Center), funded by Ghent University, the Hercules Foundation and the Flemish Government - department EWI.

References

[1] J. Q. Chen, A. Bozzano, B. Glover, T. Fuglerud, and S. Kvisle, “Recent advancements in ethylene and propylene production using the UOP/Hydro MTO process,” *Catalysis Today*, vol. 106, no. 1–4, pp. 103–107, 2005.

[2] V. V. Speybroeck, K. D. Wispelaere, J. V. d. Mynsbrugge, M. Vandichel, K. Hemelsoet, and M. Waroquier, “First principle chemical kinetics in zeolites: the methanol-to-olefin process as a case study,” *Chem. Soc. Rev.*, vol. 43, no. 21, pp. 7326–7357, 2014.

[3] B. P. C. Hereijgers, F. Bleken, M. H. Nilsen, S. Svelle, K.-P. Lillerud, M. Bjørgen, B. M. Weckhuysen, and U. Olsbye, “Product shape selectivity dominates the Methanol-to-Olefins (MTO) reaction over H-SAPO-34 catalysts,” *Journal of Catalysis*, vol. 264, no. 1, pp. 77–87, 2009.

[4] D. Lesthaeghe, A. Horré, M. Waroquier, G. B. Marin, and V. Van Speybroeck, “Theoretical Insights on Methylbenzene Side-Chain Growth in ZSM-5 Zeolites for Methanol-to-Olefin Conversion,” *Chem. Eur. J.*, vol. 15, no. 41, pp. 10803–10808, 2009.

[5] C.-M. Wang, Y.-D. Wang, Z.-K. Xie, and Z.-P. Liu, “Methanol to Olefin Conversion on HSAPO-34 Zeolite from Periodic Density Functional Theory Calculations: A Complete Cycle of Side Chain Hydrocarbon Pool Mechanism,” *J. Phys. Chem. C*, vol. 113, no. 11, pp. 4584–4591, 2009.

[6] K. De Wispelaere, K. Hemelsoet, M. Waroquier, and V. Van Speybroeck, “Complete low-barrier side-chain route for olefin formation during methanol conversion in H-SAPO-34,” *Journal of Catalysis*, vol. 305, pp. 76–80, 2013.

[7] A. Taheri Najafabadi, S. Fatemi, M. Sohrabi, and M. Salmasi, “Kinetic modeling and optimization of the operating condition of MTO process on SAPO-34 catalyst,” *Journal of Industrial and Engineering Chemistry*, vol. 18, pp. 29–37, Jan. 2012.

[8] D. S. Wragg, R. E. Johnsen, P. Norby, and H. Fjellvåg, “The adsorption of methanol and water on SAPO-34: in situ and ex situ X-ray diffraction studies,” *Microporous and Mesoporous Materials*, vol. 134, no. 1–3, pp. 210–215, 2010.

[9] K. Hemelsoet, J. Van der Mynsbrugge, K. De Wispelaere, M. Waroquier, and V. Van Speybroeck, “Unraveling the Reaction Mechanisms Governing Methanol-to-Olefins Catalysis by Theory and Experiment,” *ChemPhysChem*, vol. 14, no. 8, pp. 1526–1545, 2013.

[10] K. De Wispelaere, B. Ensing, A. Ghysels, E. J. Meijer, and V. Van Speybroeck, “Complex Reaction Environments and Competing Reaction Mechanisms in Zeolite Catalysis: Insights from Advanced Molecular Dynamics,” *Chem. Eur. J.*, pp. n/a–n/a, 2015.

[11] S. L. C. Moors, K. De Wispelaere, J. Van der Mynsbrugge, M. Waroquier, and V. Van Speybroeck, “Molecular Dynamics Kinetic Study on the Zeolite-Catalyzed Benzene Methylation in ZSM-5,” *ACS Catal.*, vol. 3, no. 11, pp. 2556–2567, 2013.

Contents

List of abbreviations

AIMD	Ab initio molecular dynamics
AO	Atomic orbital
BAS	Brønsted acid site
BFB	Bubbling fluidized bed
BO	Born-Oppenheimer
bpd	Barrel per day
$C_2^=$	Ethylene
$C_3^=$	Propylene
$C_4^=$	Isobutene
CFB	Circulating fluidized bed
CHA	Chabazite
CN	Coordination number
CSVR	Canonical sampling through velocity rescaling
CV	Collective variable
DFB	Dual fluidized bed
DFT	Density functional theory
DME	Dimethyl ether
DOMY	Dimethyl oxonium methylide
EDMO	Ethyldimethyl oxonium ion
ETO	Ethanol-to-olefin
FES	Free energy surface
GGA	Generalized gradient approximation
GPW	Gaussian plane wave
GTO	Gaussian type orbital
heptaMB$^+$	Heptamethylbenzenium cation
HMB	Hexamethylbenzene
HMMC	1,2,3,3,4,5-hexamethyl-6-methylene-1,4-cyclohexadiene
HP	Hydrocarbon pool
LDA	Local density approximation
LFEP	Lowest free energy path

MD	Molecular dynamics
MEE	Methylethyl ether
MGGA	Meta-generalized gradient approximation
MM	Molecular mechanics
MOMY	Methyl oxonium methylide
MTD	Metadynamics
MTG	Methanol-to-gasoline
MTH	Methanol-to-hydrocarbon
MTO	Methanol-to-olefin
MTP	Methanol-to-propylene
NQE	Nuclear quantum effects
OCP	Olefin cracking process
PW	Plane wave
QM	Quantum mechanics
R_{EthEli}	Reactant of the ethylene elimination
R_{JMe1}	Reactant of the first methyl jump
R_{JMe2}	Reactant of the second methyl jump
R_{JMe3}	Reactant of the third methyl jump
SCF	Self consistent field
SN	Stoichiometric number
STO	Slater type orbital
TDDFT	Time-dependent density functional theory
TMO	Trimethyl oxonium ion

List of symbols

$\overrightarrow{a_I}$	m s^{-2}	Acceleration of the nuclei
β	J $^{-2}$	Thermodynamic beta
$\overrightarrow{F_I}$	N	Forces on the nuclei
$F(s)$	kJ mol^{-1}	Free energy surface
$\Delta G^\ddagger$	kJ mol^{-1}	Free energy barrier
$\Delta \overrightarrow{G}^\ddagger$	kJ mol^{-1}	Forward free energy barrier
$\Delta \overleftarrow{G}^\ddagger$	kJ mol^{-1}	Backward free energy barrier
ΔG_r	kJ mol^{-1}	Reaction free energy
$\Delta_r H^0$	kJ mol^{-1}	Heat of reaction
k_B	J K^{-1}	Boltzmann constant
M_I	kg	Mass of the nuclei
R	J mol^{-1} K^{-1}	Universal gas constant
r_0	Å	Reference bond distance
T	K	Temperature
V	J	Potential
V_G	kJ mol^{-1}	Bias potential

Chapter 1

Introduction

Nowadays, the depleting oil reserves are a well-known problem in industry. Not only the use of fossil fuels will be affected, but also the availability of carbon based chemicals will drop significantly.[1] Furthermore, the crude oil prices are high, as depicted in Figure 1.1. Therefore, other sources for the production of fuels and chemicals need to be found. These considerations, together with the more stringent environmental policies, have directed the attention of researchers to the use of biomass as a resource for fuels and chemicals in the last few years.[2] There are a lot of potential routes to convert biomass into chemicals and fuels. Some possibilities are fermentation, fast pyrolysis, gasification to synthesis gas etc.[3] The syngas that can be produced by gasification has different possible conversion routes to valuable chemicals and fuels.[4] One of these possible production routes is the methanol-to-olefin (MTO) process, which is the subject of this master dissertation.

1.1 Production of Syngas

Syngas is a gaseous mixture, mainly consisting of CO, H_2, CH_4 and CO_2. The production of syngas was already introduced in the 1800s. At that time, coal gasification was used for lighting and heating. In the beginning of the 20th century, the process was first used for the production of fuels and chemicals. Nowadays, syngas can be produced from any carbon rich feedstock, including natural gas, naphtha, coal and biomass.[4]

The production of syngas from these feedstock is done via gasification, one of the three possible pyrolysis modes. This is a high temperature partial oxidation process where the carbonaceous feedstock is converted into the gaseous mixture by the use of a gasifying agent. The reactions taking place in the gasification process are:[6]

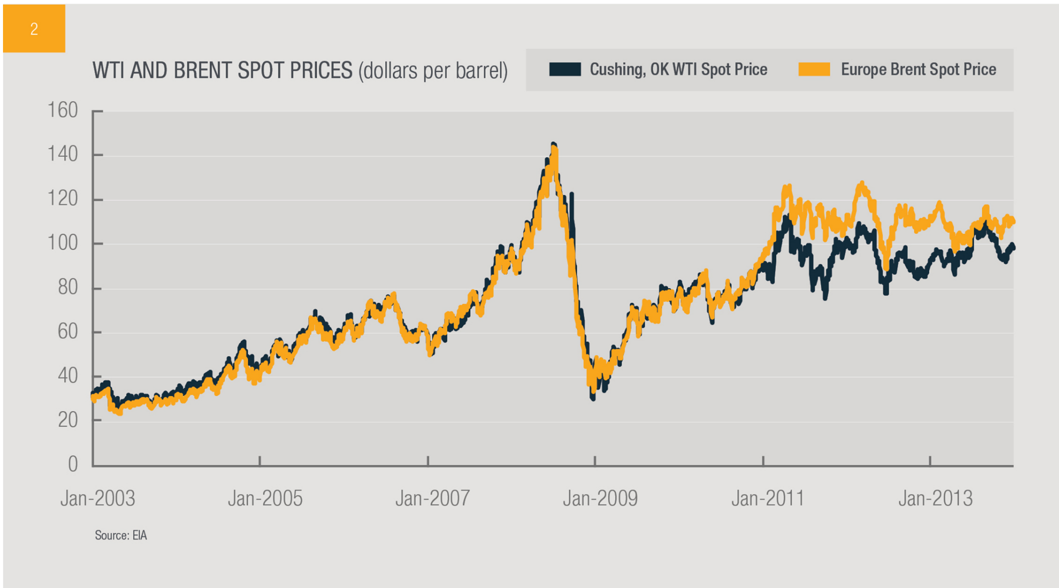

Source: EIA

Figure 1.1: The evolution of the American and European oil prices.[5]

$$\begin{array}{lllllll}
C & + & 1/2\ O_2 & \rightleftharpoons & CO & & & \Delta_r H^0 = \text{-268 kJ mol}^{-1} \\
C & + & O_2 & \rightleftharpoons & CO_2 & & & \Delta_r H^0 = \text{-406 kJ mol}^{-1} \\
C & + & H_2O & \rightleftharpoons & CO & + & H_2 & \Delta_r H^0 = +118\text{ kJ mol}^{-1} \\
CO & + & H_2O & \rightleftharpoons & CO_2 & + & H_2 & \Delta_r H^0 = \text{-42 kJ mol}^{-1} \\
CO & + & 3\ H_2 & \rightleftharpoons & CH_4 & + & H_2O & \Delta_r H^0 = \text{-88 kJ mol}^{-1}
\end{array}$$

There are a number of possible gasifying agents available. Examples are air, pure oxygen, carbon dioxide, etc. The emphasis of gasification is to maximize the gas yield, which is in contrast with the other modes of pyrolysis, namely fast pyrolysis for a high liquid yield and carbonization for a high char yield.[7] The different operation parameters of the gasification process, such as the flow rate, the composition, the moisture content, etc. influence the performance of the gasification.[8] There are three main configurations of gasifiers, namely fixed bed, fluidized bed and entrained flow gasifiers.[7,9]

1.1.1 Fixed bed gasifiers

This first type of gasifier has been the traditional process used for gasification at a temperature of 1000 °C. The fixed bed gasifiers can be classified into three types based on the direction of the airflow, namely updraft, downdraft and cross flow. The updraft and downdraft configurations are represented in Figure 1.2. In the updraft configuration, the feed is added at the top of the gasifier, while the oxidizing agent is added at the bottom. In the lower part, the combustion chamber, the char, which is the solid remainder of the feed, is combusted to reach the high temperature. The hot gas passes upwards through the gasifier and pyrolyzes the biomass in the devolatilization zone. Because the biomass is also dried by the hot gas, the temperature of the outlet gas stream is around 200-300 °C. In the downdraft design, both the feed and the air move in the same direction. Because the product gases have to pass through the hot zone, the formed tar, which is the liquid phase, is partially cracked, giving a lower tar content in the product gas. The disadvantages of this configuration are the lower heat efficiency and the higher particulates content. In the cross flow design, biomass moves downwards while the oxidizing agent is introduced from the side. The disadvantages of this configuration are the low energy efficiency and the high tar content.[6]

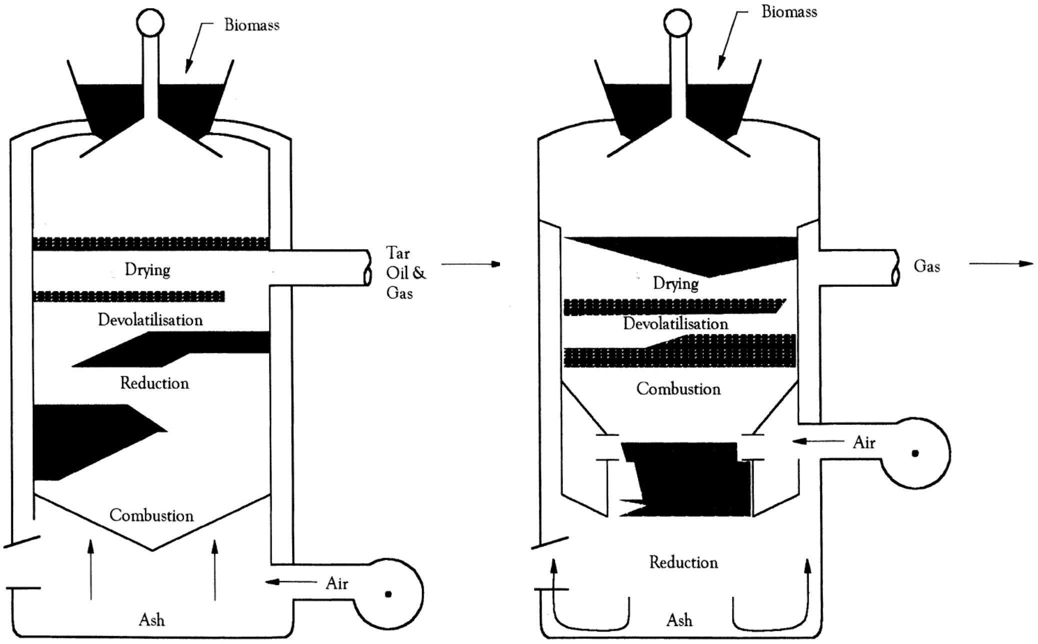

Figure 1.2: Representation of an updraft (left) and downdraft (right) gasifier.[6]

1.1.2 Fluidized bed gasifiers

One of the main disadvantages of the fixed bed gasifier is the wide temperature distribution leading to a limitation in the scale-up of this gasifier configuration.[10] This problem is solved by using a fluidized bed gasifier instead. At the same time, a disadvantage is introduced, namely the higher particulates content compared to a fixed bed gasifier. In this type of reactor, the uniformity of temperature is achieved using a bed of fine grained material into which air is introduced, fluidizing the bed material and ensuring intimate mixing of the different streams. There are three types of fluidized bed gasifiers available, namely bubbling (BFB), circulating (CFB) and dual (DFB) fluidized bed. A bubbling fluidized bed, depicted in Figure 1.3 at the left, consists of a vessel with a grate at the bottom through which air is introduced to fluidize the fine grained material and biomass feed. The temperature in the reactor is controlled via the air/biomass ratio to obtain a constant temperature in the 700-900 °C range.[6] In a circulating fluidized bed, the bed material is circulated between the reaction vessel and a cyclone separator, where the solids are removed and returned to the reaction vessel. This type of reactor configuration, depicted in Figure 1.3 at the right, has the advantage of high throughput capacity.[6]

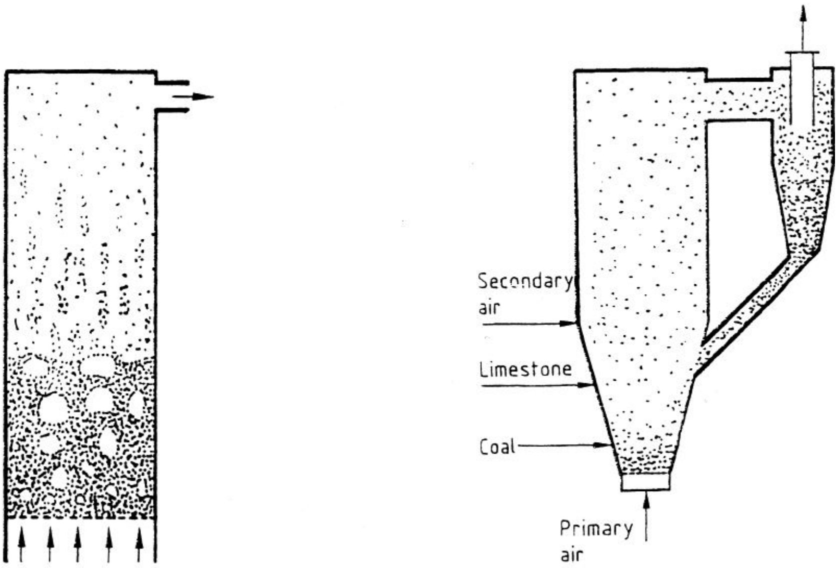

Figure 1.3: Representation of a bubbling fluidized bed (left) and circulating fluidized bed (right) gasifier.[10]

The third type of fluidized bed gasifier is a more recent developed configuration, namely the DFB, depicted in Figure 1.4. This type of reactor combines the advantages of both other fluidized bed techniques. It consists of two fluidized bed reactors that are interconnected with circulated heat carrier particles. In this way the pyrolysis and gasification is separated from the combustion of the unreacted char to avoid dilution of the product gas.[11] This reactor technology is not available yet in large scale plants, since the scale-up still needs to be examined further.[11,12]

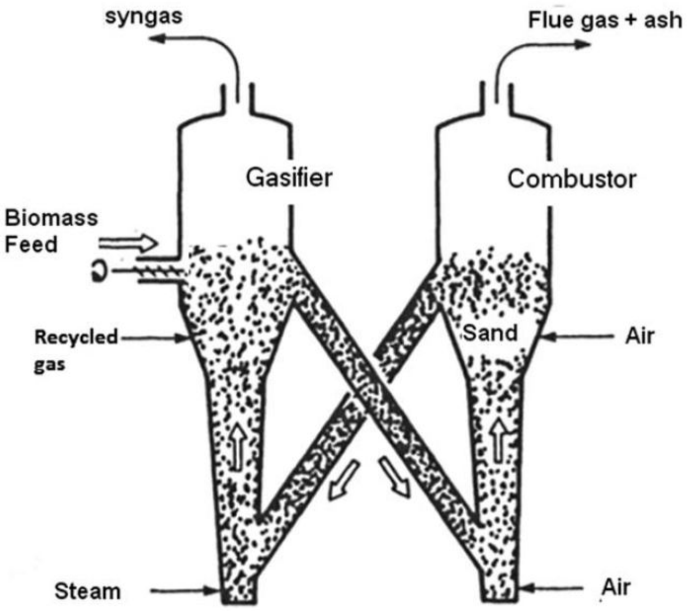

Figure 1.4: Representation of a dual fluidized bed gasifier.[12]

1.1.3 Entrained flow gasifiers

The third type of gasifier is the entrained flow configuration, depicted in Figure 1.5, which are the most widely used gasifiers.[9] This reactor type has the advantage to have the largest flow through capacities among the different designs. In this reactor design, the feed is preprocessed to obtain a slurry, which is a suspension with a relatively high water content up to 30 %. This slurry is then fed to the reactor in co-current with the oxidizing agent. The gasifier is operated at high temperatures between 1200 and 2000 °C, which guarantees high carbon conversion rates at short residence times. Another advantage of the high temperature is the low tar content in the product gas.[13]

1.2 From syngas to methanol

The syngas that can be obtained from biomass via the gasifiers described in Section 1.1 can be used in the synthesis of methanol. This process, for which a simplified scheme is shown in Figure 1.6, was first introduced as a high-temperature, high-pressure synthesis over ZnO/Cr_2O_3 catalysts. This process was operated at 350 °C and at a pressure between 250 and 350 bar. Over the years, the removal of impurities, such as sulfur, chlorine and metals, was gradually improved. This led to the renewed interest in Cu catalysts for methanol synthesis, since this catalyst is easily poisoned. In 1966, a new $Cu/ZnO/Al_2O_3$ catalyst led to the development of a new generation of methanol

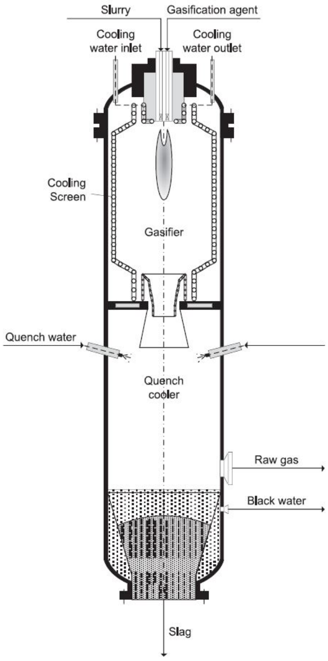

Figure 1.5: Representation of an entrained flow gasifier.[13]

synthesis processes at low temperature (220-275 °C) and low pressure (50-100 bar). To obtain catalyst life times of 2-5 years, gas phase concentration of sulfur needs to be kept under 1 ppm, while the HCl content needs to be below 1 ppb.[4]

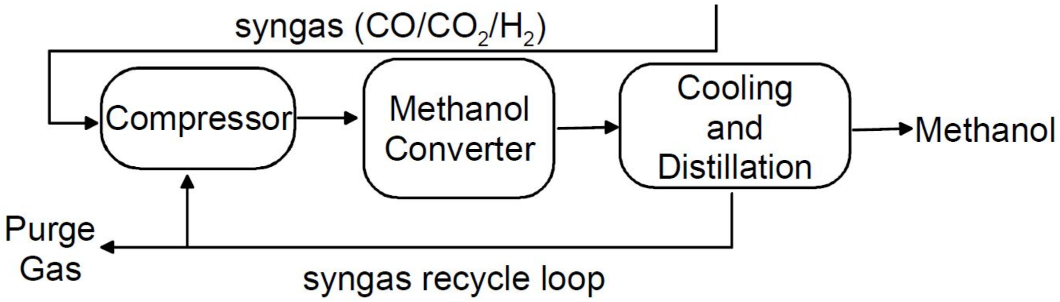

Figure 1.6: Simplified block diagram for the production of methanol from syngas.[4]

As seen in the reactions shown below[14], the formation of methanol from syngas is very exothermic, so lower temperatures will lead to higher conversions. On the other hand, the catalyst becomes less active at lower temperatures, so therefore the reactor temperature is selected while considering these two effects. There are two types of methanol converters, namely the isothermal reactors and the adiabatic reactors. Isothermal reactors operate similarly as a heat exchanger, since heat is continuously removed, e.g. the Lurgi Methanol Converter.[4] Adiabatic reactors on the other hand mostly consist of multiple catalyst beds with heat exchangers in between. An example is the adiabatic methanol converter developed by Kellogg, Brown and Root.[4]

$$\begin{array}{llllllll}
CO & + & 2\,H_2 & \rightleftharpoons & CH_3OH & & & \Delta_r H^0 = \text{-90.55 kJ mol}^{-1} \\
CO_2 & + & 3\,H_2 & \rightleftharpoons & CH_3OH & + & H_2O & \Delta_r H^0 = \text{-49.33 kJ mol}^{-1} \\
CO_2 & + & H_2 & \rightleftharpoons & CO & + & H_2O & \Delta_r H^0 = \text{+41.12 kJ mol}^{-1}
\end{array}$$

An important design specification for the fresh syngas fed to the reactor is that the molar concentrations in the reactor should have a stoichiometric number (SN) equal to 2. The SN is calculated by:

$$SN = \frac{[H_2] - [CO_2]}{[CO] + [CO_2]} \tag{1.1}$$

in which [-] is the molar concentration of that component.[14]

1.3 History of the methanol-to-hydrocarbons processes

The methanol-to-gasoline (MTG) process, where methanol is converted to gasoline over the synthetic zeolite H-ZSM-5, was accidentally discovered by Mobil.[15] In 1985 this process was commercialized in New Zealand where a 14500 bpd (barrel per day) plant was built based on natural gas.[16] In this first MTG process design a fixed bed reactor was used for which a simplified block diagram is given in Figure 1.7.[17]

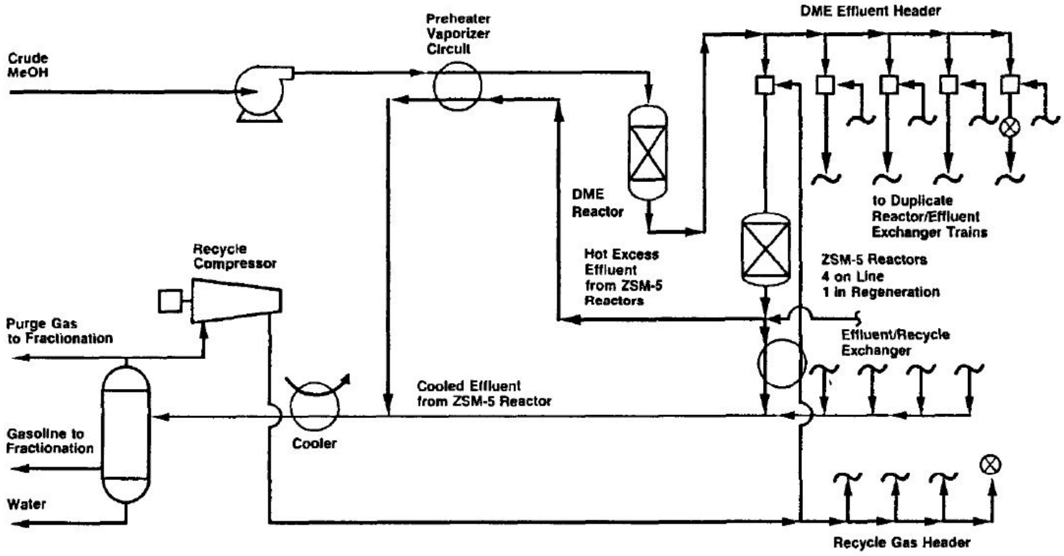

Figure 1.7: Simplified block diagram for methanol-to-gasoline process using a fixed bed reactor.[17]

In this process, methanol is first dehydrated to an equilibrium mixture of methanol, water and dimethyl ether (DME). Subsequently, the mixture enters the gasoline reactor in which it is converted to C_1-C_{11} hydrocarbons. The reaction is again exothermic and the temperature of the reactor is controlled by diluting the feed by recycling the light products. A typical temperature in the reactor lies between 350 and 410 °C and the pressure is 20 bar. The H-ZSM-5 catalyst used in the reactor deactivates due to cokes formation. Therefore, the catalyst must be regenerated, which is why parallel reactors are used for intermittent regeneration.[16] Later, a fluidized bed set up has been developed for continuous removal and subsequent regeneration of the catalyst. Afterwards, the regenerated catalyst can be recycled into the reactor. The flow sheet of the use of a fluidized bed reactor in the MTG process is depicted in Figure 1.8.[17] Some advantages of the fluidized bed reactor compared to the fixed bed process are:[15]

- Good heat transfer properties leading to easy steam generation.
- Continuous regeneration of the catalyst and uniform bed temperature resulting in a constant gasoline quality.
- Higher specific throughput.
- Higher octane number and lower durene content.
- Lower specific investment.

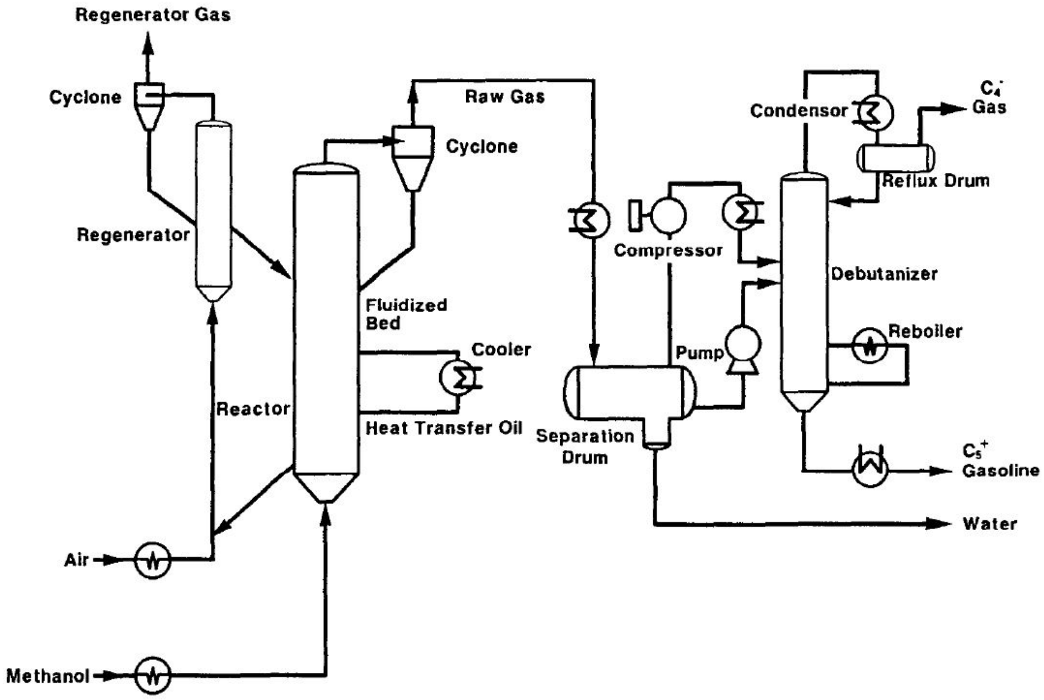

Figure 1.8: Simplified block diagram for methanol-to-gasoline process using a fluidized bed reactor.[17]

Another process where H-ZSM-5 is used as a catalyst is the methanol-to-propylene

(MTP) process developed by Lurgi. In this process, undesired products are simply recycled to the conversion reactor. The reaction is executed in a parallel fixed bed quench reactor close to atmospheric pressure and at temperatures around 460-480 °C.[16]

Mobil also developed other processes that convert methanol into hydrocarbons. One of them is the MTO process, in which the reaction conditions are modified to obtain a high yield of light olefins (ethylene/propylene). This was obtained by using a higher reaction temperature (500 °C), a lower pressure and lower catalyst acidity.[4] This process is no longer commercially used, but UOP and Hydro introduced their own MTO process based on another synthetic catalyst, namely H-SAPO-34. Due to its chabazite (CHA) structure consisting of large cavities connected by 8-rings, the diffusion of heavy and/or branched hydrocarbons is restricted and a high selectivity to light olefins is obtained. The obtained ethylene to propylene ratio can be varied between 0.5 and 1.5.[18] The deactivation of this catalyst due to coking is even faster than for the H-ZSM-5 catalyst. Therefore, continuous regeneration using a low-pressure fluidized bed reactor design needs to be used as depicted in Figure 1.9. By burning the coke with air for the regeneration of a portion of the used catalyst, constant catalyst activity and product composition can be maintained.[18]

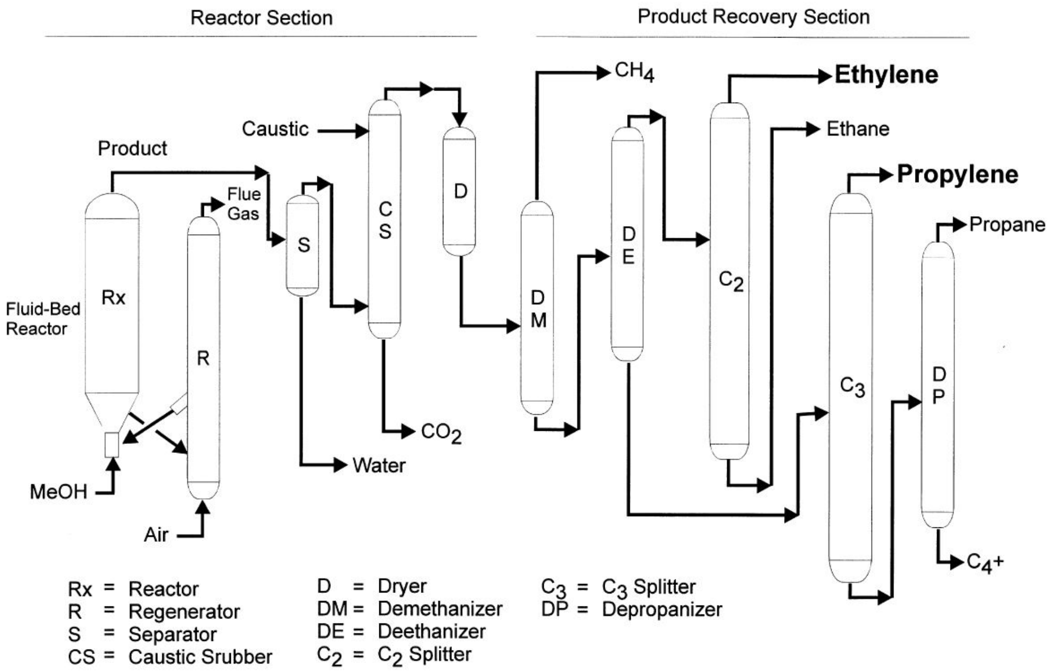

Figure 1.9: Simplified block diagram for the methanol-to-olefin process.[15]

The fluidized bed also provides flexibility to adjust operating conditions and better heat recovery from the exothermic MTO reactions. The reactor operating conditions can be adjusted to obtain the desired product requirements. Lower methanol partial pressure leads to a higher selectivity of light olefins, especially ethylene. Therefore, yield advantage can be obtained by using crude methanol which contains around 20 wt.% of water. Another operating condition that can be changed to alter the product yields is temperature. Higher temperature leads to increased ethylene yields, but too high temperatures will lead to lower total light olefin yields due to excessive cokes formation.[18] Optimal operating conditions for the MTO process are dependent on whether a maximum yield of ethylene or propylene is targeted. Operating temperatures are in a range of 390-425 °C, pressure is around 1 bar and water to methanol molar ratio is between 3-4.[19] The reactor effluent is cooled, compressed and sent through a caustic scrubber to remove CO_2 and to a dryer to remove water. Subsequently, the effluent is sent to the product recovery section which consists of a demethanizer, a deethanizer, a C_2 splitter, a C_3 splitter and a depropanizer.[15] The yield of light olefins can be improved even further by combining this process with the olefin cracking process (OCP) introduced by Total Petrochemicals and UOP as illustrated in Figure 1.10.[16] In this process C_{4+} olefins, which are byproducts of the MTO process, are fed to the olefin cracking unit where they are cracked to mainly propylene and also ethylene. This integrated process can lead to an increase of the carbon selectivity of methanol to ethylene and propylene to about 85-90 %.[18]

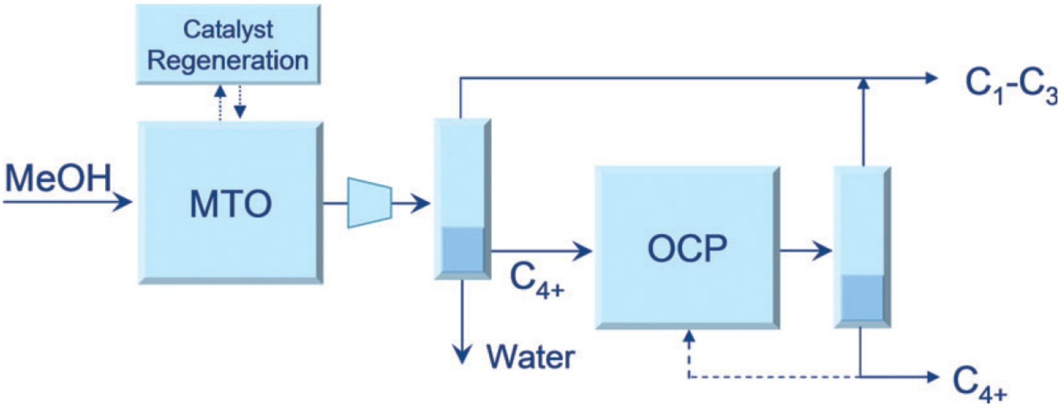

Figure 1.10: Simplified block diagram for methanol-to-olefin process combined with the olefin cracking process.[16]

A variant of the MTO process is developed by researchers at Dalian Institute of Chemical Physics. The process, called DMTO, is also applied in a fluidized bed reactor, but it includes a recycle of the C_{4+} stream to maximize ethylene and propylene production.[16]

Chapter 2

MTO reaction mechanisms

After the discovery of the methanol-to-hydrocarbon (MTH) processes, research on the governing mechanism started immediately. It was found that different stages occur during the overall methanol conversion process by Haw et al.[20] The different stages are schematically depicted in Figure 2.1.[21]

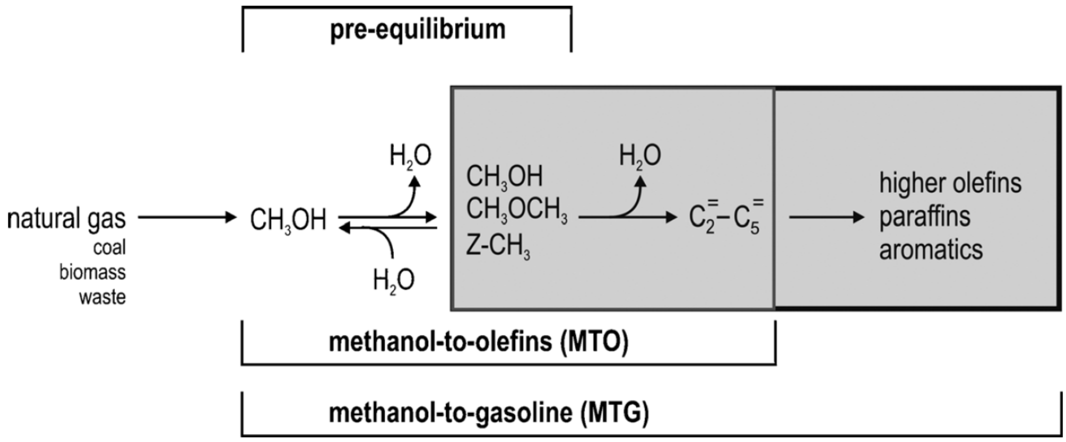

Figure 2.1: Schematic representation of the different stages occurring during methanol conversion.[20,21]

As a first step in the reaction, an equilibrium is reached between methanol, dimethyl ether (DME) and water. Subsequently, an induction period occurs after which the first hydrocarbon products are produced. Finally, the light olefin products are converted into secondary reactions to cokes species that deactivate the catalyst.[20,21]

The reaction mechanism governing the MTH processes has been the subject of a lot of discussion and research. Various experimental techniques have been used to study this mechanism, but due the occurrence of many simultaneous reactions, it is difficult to translate the kinetic data to individual reaction steps and mechanistic insight.[22] In contrast, theoretical simulation offer the advantage of isolating individual elementary steps and separating the influence of distinct properties such as catalyst topology and chemical composition. Therefore, the combination of theory and experiment provide a means to obtain a detailed description of the reaction mechanisms and corresponding intermediates.[21]

Initially, a direct C-C coupling from C_1 units as methanol and dimethyl ether was proposed. More than 20 direct mechanisms were proposed based on different intermediates[23], but none of the propositions were found to explain the induction period[20] or led to a route to light olefins with acceptable reaction barriers.[24,25] This failure of the direct mechanism will be explained in more detail in Section 2.1.

Since the direct mechanism fails to explain the observed kinetic induction period, it was believed that a relatively inefficient direct mechanism functions only as the induction reaction which is followed by more efficient autocatalytic reactions through olefin chain growth and cracking.[20] This indirect mechanism was first proposed by Dessau et al.[26,27] In the same period, Mole et al.[28] found an enhanced rate of methanol conversion when adding aromatics to the feed. Similarly, Langner[29] found improved conversion rates when co-feeding cyclohexanol with methanol. All these findings led to the introduction of the indirect mechanism formulated by Dahl and Kolboe[30–32], depicted in Figure 2.2.

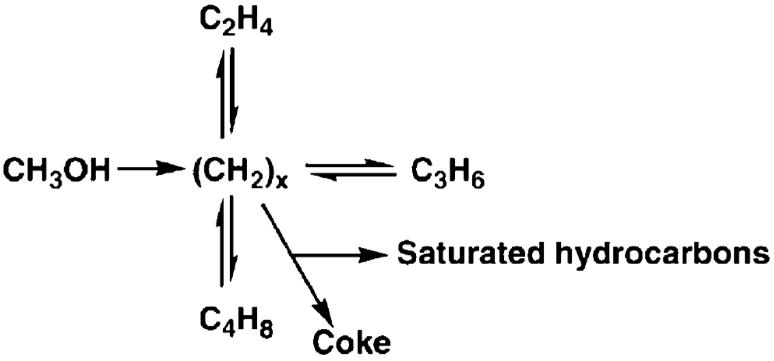

Figure 2.2: Hydrocarbon pool mechanism proposed Dahl and Kolboe.[32]

In this mechanism hydrocarbons that are present in the zeolite pores act as a co-catalyst for the MTH reactions. Since the co-feeding experiments of ethylene or propylene with methanol by Dahl and Kolboe[31,32] led to the conclusion that these alkenes are mostly not reactive, other hydrocarbon co-catalysts needed to be found. The first work was carried out by Mikkelsen et al.[33] where ^{13}C-methanol and toluene were co-reacted over different zeolite catalysts leading to arenes adsorbed within the zeolite cavities as being important participants in the MTH reaction. Based on this work, Arstad and Kolboe decided to extend the work by studying the molecules that are retained within te catalyst cavities when H-SAPO-34 is used as catalyst in the MTO reaction.[34,35] By combining the analysis of the retained molecules with isotopic labeling it was virtually proven that polymethylbenzenes are the "catalytic engine" in the MTO reaction in H-SAPO-34.[35] These findings led to the introduction of the concept of a supramolecular catalyst by Haw et al.[36], which is depicted in Figure 2.3. The reaction mechanisms based on hydrocarbon pool (HP) species proposed so far, are discussed in more detail in Section 2.2.

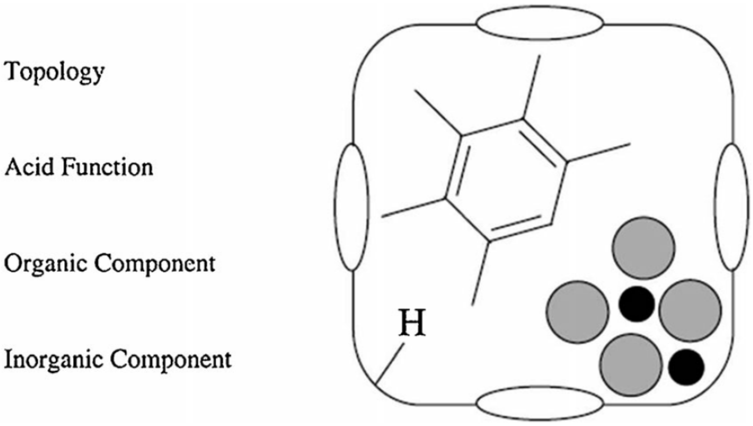

Figure 2.3: Representation of the supramolecular catalyst concept introduced by Haw et al.[36] together with the four key features that influence the MTO reaction.

Although the HP reaction mechanism governing the active stage of the MTH process is generally accepted, the origin of the HP remains a puzzling question. The direct C-C coupling suggested by Haw et al.[20] to play a role during the induction period was disproved by the experiments performed by Song et al.[37] This paper reports dedicated experimental work using highly purified reagents and catalysts showing that methanol/dimethyl ether is not reactive on either of the two most important catalysts in the absence of a primordial hydrocarbon pool. They propose that instead, the HP grows from carbonaceous impurities present in regular methanol feed and/or zeolite catalysts. This proposition was subsequently disproved by the observation of Jiang et al.[38] where traces of impurities in the methanol feed were not found to influence the formation of primary hydrocarbons from surface methoxy groups. More recently, a plausible but experimentally not proven route has been proposed for the formation of HP species in H-ZSM-5 starting from small hydrocarbon fragments and methanol.[21,39]

2.1 Direct mechanisms

As stated before, over 20 distinct mechanisms have been proposed for the formation of the first C-C bond, based on the direct formation of small olefins from only methanol or dimethyl ether.[23] Due to improvement of computational facilities, the experimentally suggested mechanisms could be theoretically tested. When the theoretical contributions were considered separately, they all seemed to provide evidence for partial pathways of the commonly proposed direct mechanisms. When all these individual reactions were combined by Lesthaeghe et al. as depicted in Figure 2.4, theoretically obtained rate coefficients turned out to show the exact opposite.[24,25] Their conclusions will be summarized in this paragraph.

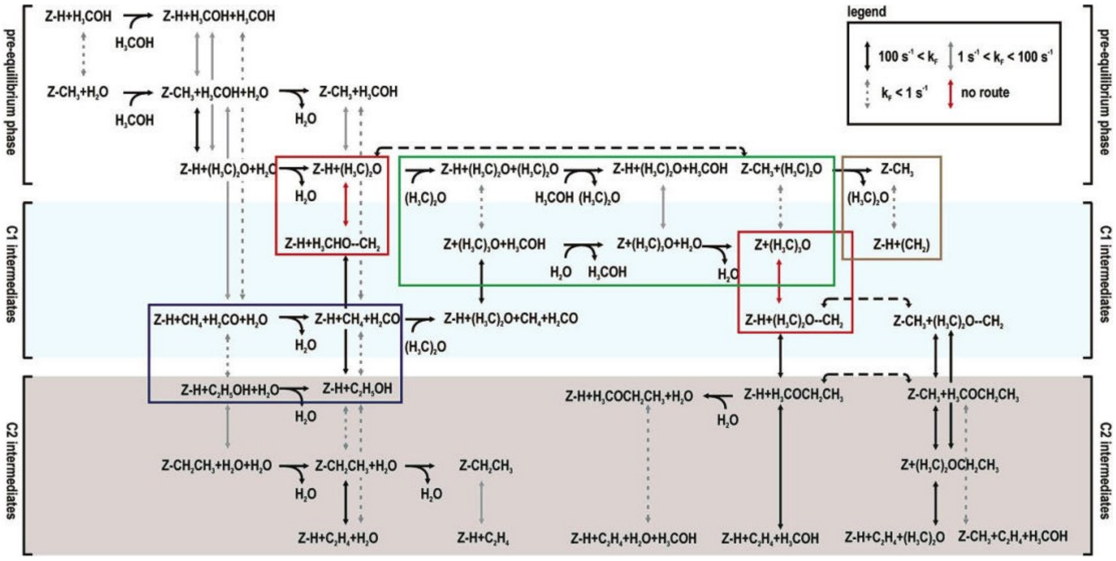

Figure 2.4: Overview of all direct reactions from methanol to ethylene combined by Lesthaeghe et al.[25]

These theoretical results confirm the development of the first equilibration between methanol, dimethyl ether and water, as well as other C_1-species. There are however three bottlenecks found that prevent the direct C-C coupling of these C_1-species.[25]

One of the important C_1 species formed from the initial mixture is the trimethyl oxonium ion (TMO). The proposed mechanisms for the formation of TMO are represented in the green rectangle in Figure 2.4. These steps were studied by Blaszkowski et al.[40] and Tajima et al.[41] Furthermore, it was found that the positively charged TMO forms an ion-pair with the negative aluminum defect and can thus not be adequately described in the small cluster approach. Calculations on larger clusters demonstrated that TMO is stabilized by the zeolite framework.[42] The problems with this intermediate arise when TMO is converted in the next step. Oxonium ylides (a carbene group coordinated to methanol or DME) are suggested as subsequent intermediates. TMO might for example be deprotonated to form dimethyl oxonium methylide (DOMY) which might subsequently react to methylethyl ether (MEE) via Stevens' rearrangement or to ethyldimethyl oxonium ion (EDMO) via intermolecular methylation. However, it was shown that there is no possible route from TMO to DOMY.[42] Another possible intermediate which could be formed from TMO is methyl oxonium methylide (MOMY) which can subsequently react via a Stevens-type rearrangement to ethanol. Again the formation of MOMY from TMO was found to be non-existing.[42] These unstable ylide intermediates form the first bottleneck for the direct mechanism in the MTO process.

Another possible route for the direct C-C coupling is via the intermediate methane and formaldehyde. These components can be formed via several routes, namely from two methanol molecules, from a surface methoxy species and methanol or from TMO joinly adsorbed with methanol.[25] This route has been investigated by Tajima et al.[41] and Lo et al.[43,44] Methanol and formaldehyde can react to form ethanol, from which ethylene can quite rapidly be formed as depicted in the blue rectangle in Figure 2.4. Nevertheless, the conversion from methanol and formaldehyde is very slow. In this case, the slow reaction is not due to a high activation energy, but due to a small pre-exponential factor, because of the decrease in entropy.[25] The failure of this route to form C_2-species is considered the second bottleneck for the direct mechanism.

A third possible group of paths for the direct C-C coupling are the concerted reaction mechanisms as generally represented in the left part of Figure 2.5. In this scheme, the step with the high energy barrier is represented. In this step, a hydrogen abstraction from a methanol or DME methyl group by a zeolite basic oxygen bridge is combined with the formation of a carbon-carbon bond with a methanol, DME, TMO or framework bound methylgroup. These concerted steps were first analyzed by Blaskzkowski et al.[40] and later by Lesthaeghe et al.[24] This mechanism fails, because the unprotonated oxygen bridge lacks the strong basic character needed to activate the highly covalent carbon-hydrogen bond. An equally strong carbon-hydrogen bond is preferably formed, so any perturbation of the transition state leads to an automatic evolution of the system to a nearby transition state, forming methane instead, as depicted in the right part of Figure 2.5. This formation of methane is a similar observation as for Lo et al.[43,44] and cannot react further to ethylene as stated before, leading to the third bottleneck.[25] Due to the failure of the direct mechanisms, alternative indirect mechanisms based on HP species were proposed. These mechanism are further discussed in Section 2.2.

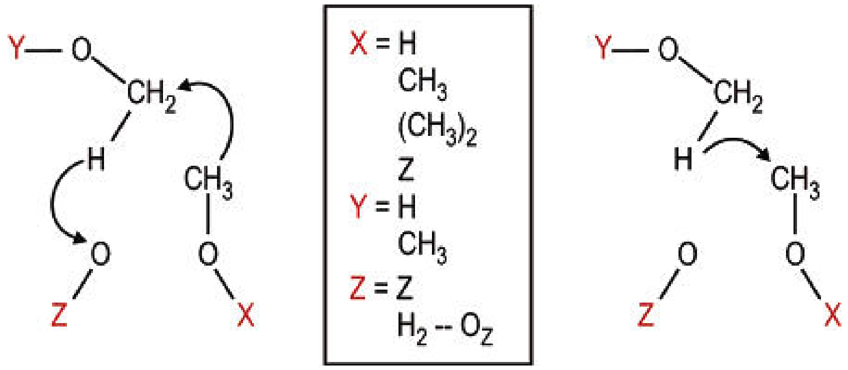

Figure 2.5: Concerted carbon-carbon coupling (left) and methane formation (right)[25]

2.2 Hydrocarbon pool mechanism

Already in the late 70s it was found that an autocatalytic mechanism plays an important role during the H-ZSM-5 catalyzed transformation of methanol to hydrocarbons.[45] Nowadays, this autocatalytic effect has generally been linked to the hydrocarbon pool mechanism.[20] This autocatalytic effect has been illustrated by Olsbye et al.[16] as depicted in Figure 2.6. The upper graph shows the variation of the hydrocarbon yield due to the increase and decrease of the flow through the reactor. As can be seen, an increase in the flow leads to an decrease of the hydrocarbon yield. When the flow is decreased again, the hydrocarbon yield increases again. This variation in found because the HP species responsible for the autocatalytic effect disappear upon increasing the flow and must be assembled again when the flow is lowered.[16]

The lower graph in Figure 2.6 shows the yield of methanol, dimethyl ether and hydrocarbons as function of a representative of the contact time (the catalyst weight to flow ratio). This yields an S-shaped curve for the hydrocarbon yield, which is characteristic for autocatalytic reactions. The S-shaped curve results from a reaction where the hydrocarbon formation is initiated with a slow formation of HP species and then accelerated by a much faster reaction of methanol with these HP species.[16] Although the HP mechanism is generally accepted, there is still a challenge in identifying the actual catalytic cycles leading to the formation of olefins from methanol. This search for catalytic cycles is complicated even more due to the fact that different catalyst topologies and compositions lead to different product distributions as depicted in Figure 2.7. Therefore, different reaction mechanisms are proposed for methanol conversion in H-SAPO-34 and H-ZSM-5. In H-SAPO-34, methylbenzenes were found to be the key components of the hydrocarbon pool.[34,35] Based on these methylbenzenes as co-catalyst, the paring and side-chain reaction cycles were proposed, which are discussed in detail in paragraph 2.2.1. For H-ZSM-5 on the other hand, the observed product distribution could not be explained based on an aromatic HP alone, so it was concluded that a different mecha-

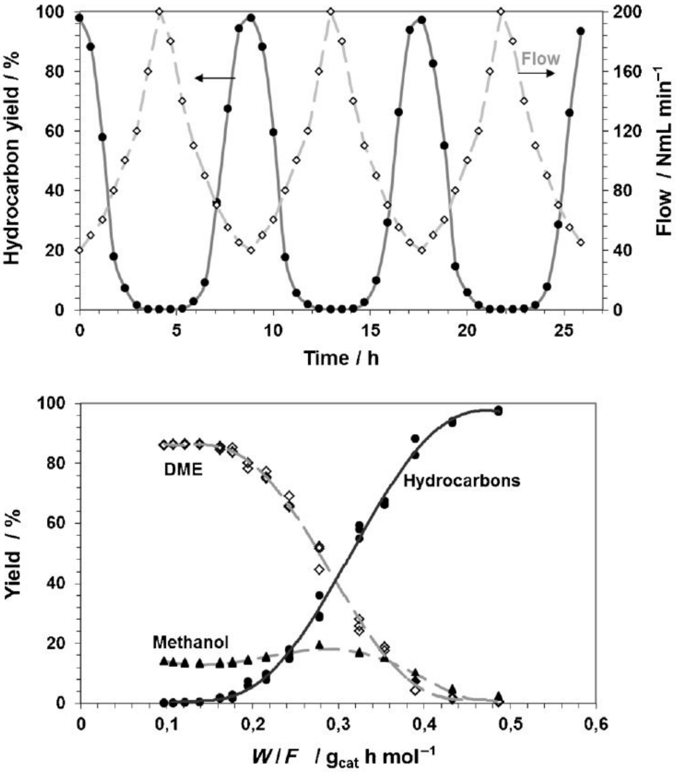

Figure 2.6: Illustration of the autocatalytic effect for the conversion of methanol over H-ZSM-5 at 350 °C and atmospheric pressure.[16]

nism must lie at the basis of the product formation.[21] The proposition for an alternative mechanism is based on the observation that ethylene and propylene are reactive when co-fed with methanol on H-ZSM-5[46,47], but not on H-SAPO-34.[30,31] Furthermore, two different product groups were observed in a more detailed ^{13}C labeling study[48], leading to the idea that two different mechanisms are operating. This led to the introduction of the dual cycle mechanism for MTH conversion on H-ZSM-5, which is discussed in more detail in paragraph 2.2.2.

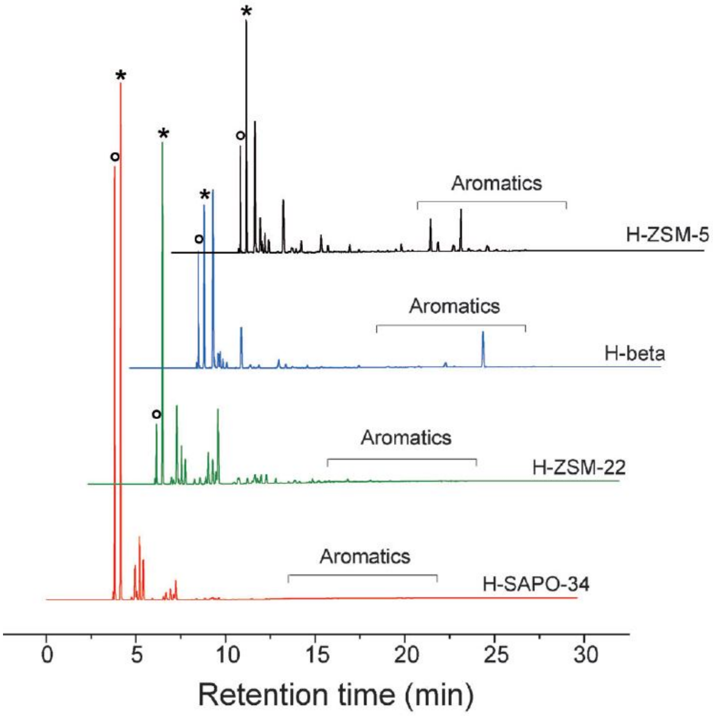

Figure 2.7: GC-FID chromatograms for different zeolite topologies at a temperature of 400 °C and a weight hourly space velocity of 2 g $g^{-1}h^{-1}$ with the ethylene peak indicated by o and the propylene peak by *.[49]

2.2.1 Paring and side-chain mechanism

The reaction cycles based on polymethylbenzenes, called the paring and side-chain mechanism, are depicted in Figure 2.8. The paring reaction cycle is based on a mechanism first introduced by Sullivan et al. in 1961.[50] In this cycle, the aromatic ring contracts, followed by the elimination of an olefin and the expansion back to the original 6-ring aromatic structure. An indication for this mechanism was the exchange of ^{12}C of the aromatic ring and ^{13}C of the labeled methanol.[51] The side-chain cycle on the other hand was proposed by Mole et al.[28,52] and further elaborated by Sassi et al.[53,54] In this mechanism an exocyclic bond in formed by deprotonation followed by side-chain methylation and subsequent elimination.

As can be seen in the reaction scheme shown in Figure 2.8, both mechanisms start with repeated methylations of the aromatic ring until a gem-methylated species is formed. Methylation reactions are in general accepted to be important in all mechanistic proposals for the MTO mechanism.[21] Different methylation mechanisms exist, namely the direct or concerted mechanism and the stepwise route as depicted in Figure 2.9.[56] In the upper part, the stepwise route is shown, in which first a methanol molecule is ph-

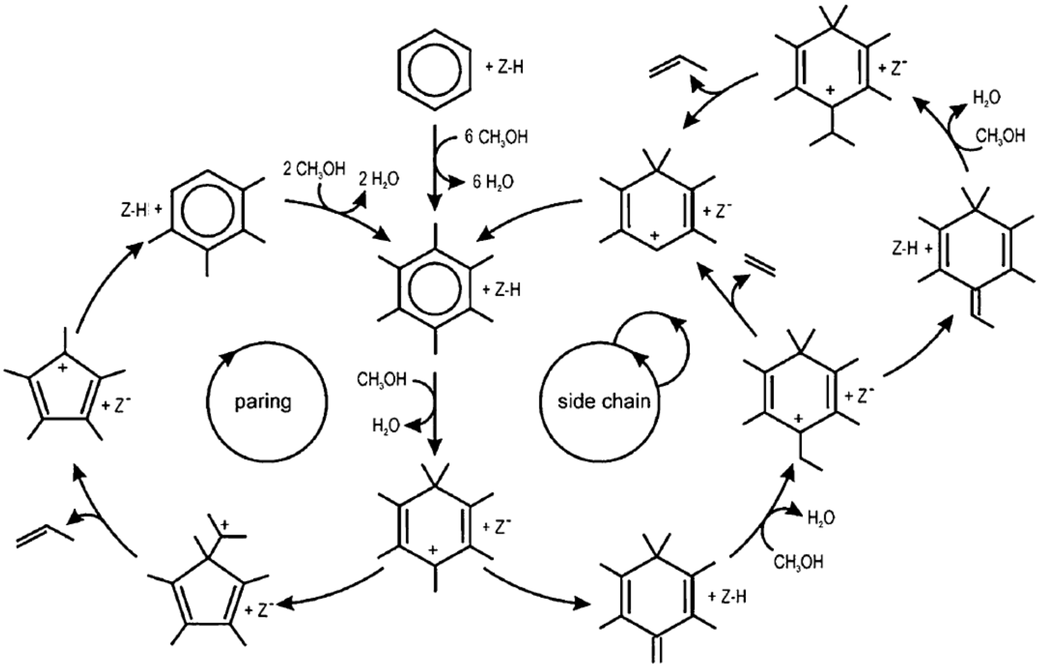

Figure 2.8: Schematic representation of the paring and side-chain mechanism for MTO conversion based on polymethylbenzenes.[55]

ysisorbed on a acid site through a hydrogen bond and subsequently a surface methoxide species is formed. As a last step, this methoxide intermediate can methylate a HP species. In the concerted mechanism, methanol is also physisorbed, but this methanol will now immediately interact with the HP species that can be methylated. Studies of the methylations of hydrocarbons by theoretical calculations are also found in literature. For example, a good agreement between theoretical and experimental data was obtained for the methylations of alkenes in H-ZSM-5.[57,58] Furthermore, molecular dynamics simulations kinetic studies showed that both stepwise and concerted routes may be followed in the methylation of benzene in H-ZSM-5.[59]

Since the aromatic cycles are mainly proposed for H-SAPO-34, it is interesting to look further into the studies of these mechanisms in this catalyst. First, the influence of the number of methyl groups on the aromatic ring on the product distribution was analyzed. This study was executed by Song et al.[60] and Arstad et al.[35] and led to the conclusion that both the reactivity and the selectivity towards propylene increases with the number of methyl substituents. They reported that propylene is favored by methylbenzenes with four to six methyl groups but ethylene is predominant obtained from those with two or three methyl groups. These variation were also found based on theoretical DFT-based studies executed by Van Speybroeck et al.[61] In contrast, DFT calculations by Wang et al.[62] resulted in the observation that the activity of the methylbenzenes is not

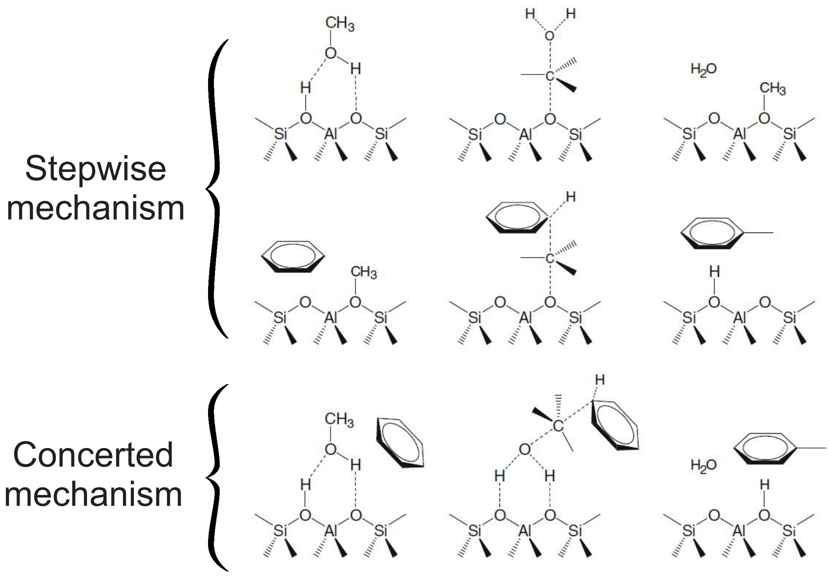

Figure 2.9: Schematic representation of the stepwise (upper two lines) and the concerted (lower line) mechanism for methylation of benzene.[56]

influenced by the number of methyl groups. More recently, a full low-barrier side-chain cycle for ethylene and propylene formation was found based on a first principle kinetic study with hexamethylbenzene as co-catalyst. The olefin elimination steps, which were the main bottleneck in earlier attempts[55,63], exhibit low free energy barriers due to a subtle interplay between an sp^3 carbon center of the organic intermediate, stabilizing non-bonding interactions and assisting water molecules.[64]

2.2.2 Dual cycle mechanism

Similar complete catalytic cycles based on lower methylated aromatics were found for the paring mechanism in H-ZSM-5[65], but not for the side-chain mechanism.[55] Furthermore, the observed product distribution of H-ZSM-5 could not be explained based on a HP route[21], so a different mechanism needed to be proposed. The proposition for an alternative reaction cycle is based on the observation that ethylene and propylene are reactive when co-fed with methanol on H-ZSM-5[46,47], but not on H-SAPO-34.[30,31] Furthermore, two different product groups were observed in a more detailed ^{13}C labeling study by Svelle et al.[48] This supported the conclusion that a different mechanism governs the methanol conversion in H-ZSM-5. Based on their observations, the authors proposed a mechanism consisting of two interconnected cycles, namely one cycle based on polymethylbenzenes yielding mainly ethylene and a second autocatalytic alkene cycle yielding mostly propylene. This mechansim, called the dual cycle mechanism, is represented in Figure 2.10.

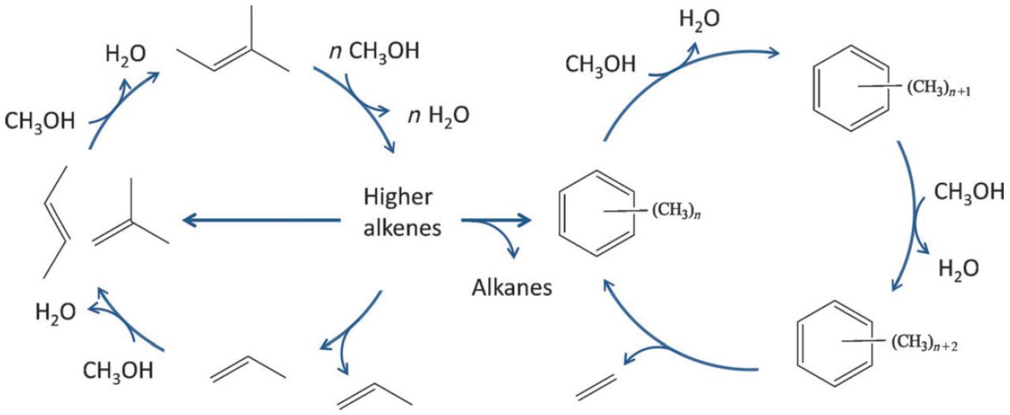

Figure 2.10: Schematic representation of the dual cycle mechanism proposed for the methanol conversion in H-ZSM-5.[16]

The two cycles are interconnected because the methylbenzene cycle can also produce propylene[66], which can act as a co-catalyst in the alkene cycle, in contrast to ethylene. This was found by Svelle et al. since ^{13}C scrambling was not found for ethylene, but it was found for the higher alkenes.[48] In the other direction, alkenes can undergo secondary reaction, like oligomerization and cyclization, leading to the formation of extra methylbenzenes. The proposed alkene cycle is similar to the homologation proposed by Dessau et al.[26,27] with as major distinction that ethylene is not included. The alkene mechanism mainly consists of methylations of the lower alkenes and cracking of the higher alkenes.[48] A possible advantage of this mechanism for the MTO process is that ethylene and propylene formation are mechanistically separated. This fact could allow to avoid ethylene formation by suppression of the aromatic cycle by choosing an interesting zeolite topology, leading to a possible methanol-to-propylene process.[16,48,66] This possibility is considered in the consideration of H-ZSM-22 as a MTP catalyst. This zeolite also consists of 10-ring channels, but does not have the extra space afforded by intersections due to the 1D topology. Based on experiments at high feeding rate which showed that H-ZSM-22 had a non-observable conversion, it was concluded that in this topology the aromatic-based cycle might be suppressed.[67] Later on, experiments with lower feeding rates showed that higher conversion could be obtained over H-ZSM-22. Furthermore, the aromatics in the channels were found to be almost inactive for methanol conversion in contrast to the effluent alkenes. The product distribution found for the effluent consisted primarily of branched C_{5+} alkenes with negligible aromatics content, which is indicative for the extensive product formation by the alkene cycle. These findings demonstrate the possibility of controlling the product selectivity based on intimate knowledge on the reaction mechanism for the methanol conversion processes.[16,49]

Chapter 3

Industrial MTO catalysts and reaction conditions

Nowadays, two catalysts are already commercially used in MTH processes.[21] Nevertheless, a large variety of materials with different topology, composition an morphology have been screened for methanol conversion both from industrial as from academic point of view.[16] Some of these analyzed catalysts are discussed in Section 3.1. Next to the characteristics of the catalysts also the influence of the process conditions like the presence of water on the conversion of methanol to hydrocarbons will be discussed. Water is a byproduct of methanol synthesis and of the MTH process itself.[19] This influence will be discussed in Section 3.2 and will be the basis for the formulation of the objective of this master dissertation drafted in Section 3.3.

3.1 Catalysts for methanol-to-hydrocarbon processes

In zeolite catalysts, shape selectivity is a key to the success. There are different forms of shape selectivity encountered in the zeolite framework, namely selectivity on the reactant, on the transition state and on the products (Figure 3.1). The selectivity of the catalyst is largely determined by the topology, namely by the dimensions of the pores possibly restricting the access to the internal channel system. The simplest classification of the pores dimensions is based on the number of T atoms forming the windows. Large-, medium- and small-pore topologies are distinguished with 12-, 10- and 8-ring windows, respectively. These ring sizes lead to window openings of approximately 7, 5.5 and 4 Å. For the MTH process it can already be concluded that reactant selectivity will not be crucial, because of the small size of the methanol (free diameter of 2.8 Å) compared to the channel dimensions. On the other hand, the importance of the transition state and product selectivity will depend on the topology and the used process parameters.[16,21,68]

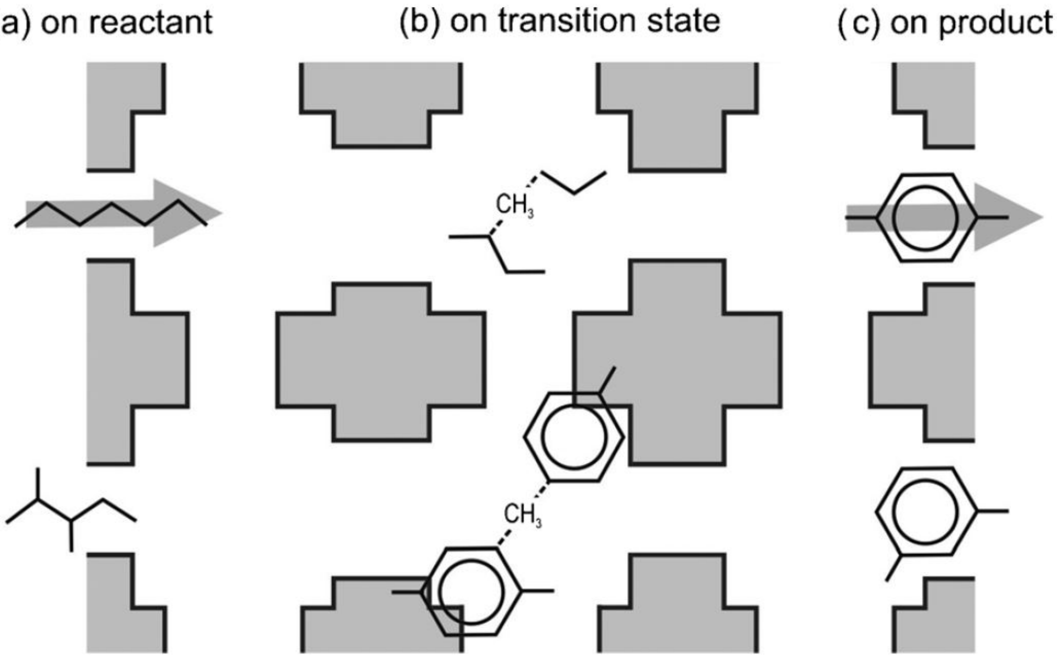

Figure 3.1: Schematic representation of the different possible forms of shape selectivity in a fictitious zeolite framework.[21]

Since H-ZSM-5 and H-SAPO-34 are the commercially used catalysts for MTH processes, these catalysts will first be discussed in detail in the coming paragraphs. Subsequently, a short overview will be given of other topologies that are mentioned in literature as possible MTH catalyst.

3.1.1 H-SAPO-34

The first industrially important MTO catalyst is H-SAPO-34, which has the chabazite topology. This topology consist of large cages (10.0 x 6.7 Å^2) which are connected via small-pore windows (3.8 x 3.8 Å^2).[69] This topology is schematically represented in Figure 3.2.[21] H-SAPO-34 is an silicoaluminophosphate or zeotype material and H-SSZ-13 is the zeolite analogue.[21]

Since water, methanol and polymethylbenzenes are found in the zeolite framework during the process, it is interesting to see how the adsorption of those molecules influences the dimensions of the catalyst unit cell. This study was performed by Wragg et al.[70] and led to the conclusion that water gives a unit cell contraction of 2 % due to the strong

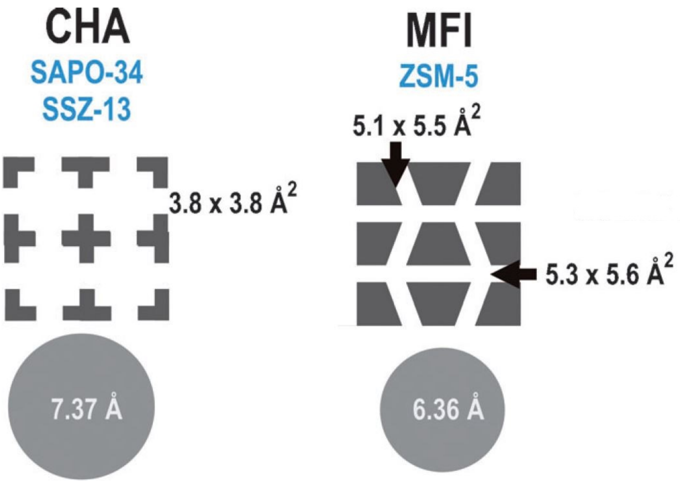

Figure 3.2: Schematic representation of the CHA and MFI topology.[21]

interactions with the framework. On the other hand, methanol adsorption leads to an expansion of 0.5 % and polymethylbenzenes cause a significant expansion. Moreover, the unit cell change was found to be very asymmetric, since the c-axis increases by 3 % while the a-axis increases only 0.1 % during the MTO process. Other experiments by Wragg et al.[71] showed that the expansion of the zeolite framework correlates well with the beginning of the propylene production and declined methanol flowthrough. Furthermore, they proposed 4 steps for the progress of the MTO reaction over H-SAPO-34 based on their observations:

1. Formation of the initial HP at a single point depending on the feed flow and the number of catalytic sites corresponding to a critical concentration of autocatalytic species.
2. Buildup of HP, first against the flow and subsequently with the flow if possible.
3. Formation of coke species from aromatic intermediates.
4. Deactivation of the bed because of heavy coke, yet some parts of the bed remain coke free.

Another study on the unit cell expansion was executed by Zokaie et al.[72] in which the influence of the retained hydrocarbons on the unit cell expansion was analyzed via both experimental and computational studies. Similar experimental results were mentioned, but to get the influence of a single hydrocarbon molecule, theoretical calculations were necessary. These pointed out that small hydrocarbons do not lead to significant cell expansion, while more bulky coke molecules like phenanthrene and pyrene cause cell expansion. Furthermore, the presence of these bulky molecules in one cage causes strain in the neighboring cages. If one bulky molecule is formed per 24 cages, a similar expansion of the crystal is found as if all cages were filled with bulky molecules.

As stated in Section 1.3, a disadvantageous characteristic of this zeotype catalyst is the fast deactivation by coke formation.[73] This deactivation is suggested to occur due to pore blocking of the small windows, which results from the transformation of the intermediates of the reaction cycles presented in Chapter 2 to larger compounds called coke species. To get more insight into the coke formation, it is interesting to identify which aromatic compounds are contained in the catalyst during reaction. This identification was conducted by Hemelsoet et al.[61,74] in a combined theoretical/experimental study. In the UV/Vis microspectroscopy experiments, mainly absorption bands around 400, 450 and 505 nm were found and focused upon. Furthermore, interaction of the used catalyst with ammonia led to the conclusion that the bands are due to carbocations. By time-dependent density functional theory (TDDFT) calculations on molecular dynamics (MD) snapshots, the aromatic carbocations corresponding to the absorption bands could be identified. This leads to the assignment of heavily methylated benzenium ions to the 400 nm band, together with singly methylated bi- and tricyclic species. Naphtalenium ions containing up to four methyl substituents are linked to the absorption band around 450 nm and the more heavily methylated bicyclic species and tricyclic compounds are held responsible for the 505 nm band.[74] It was already explained in Chapter 2 that the methylated benzenium ions are active intermediates in the olefin production cycles. Since naphtalenic species are also found in the catalyst cages during reaction, it is interesting to check if these are also active intermediate or rather coke precursors. Theoretical calculations have shown that although methylation of naphtalenic species has similar reaction barriers as methylation of methylbenzenes[61], the side-chain cycle is not a plausible route for ethylene elimination. This led to the conclusion that naphtalenic compounds should rather be considered as coke precursors than as active hydrocarbon pool species.[75]

It is interesting to analyze the influence of the acid strength on the coke formation. This is done by comparing the MTO process over H-SAPO-34 with that over H-SSZ-13, which also has a CHA topology, but higher acid strength. This comparative study was conducted by Bleken et al.[76] for temperatures from 300 to 425 °C. This paper concluded that both catalysts have similar product spectra and retained hydrocarbons. Nevertheless, H-SSZ-13 had a higher activity and faster deactivation due to the difference in acid strength. Furthermore, a lower optimum reaction temperature was found for H-SSZ-13, which can be explained by the fact that a higher acid strength will lower the reaction barriers and thus increase the rates of reaction. Lastly, both catalysts obtain a higher C_2/C_3 ratio upon increased deactivation, though this is obtained sooner for H-SSZ-13. It is suggested that the reason for this enhanced ethylene selectivity is the increased diffusion limitations due to coke formation.[16] Similar results were obtained based on theoretical calculations leading to methylation reaction rates that were three orders faster in H-SSZ-13 than in H-SAPO-34.[61]

Interesting experimental work on the MTO reaction over H-SAPO-34 is executed by Qian et al.[77–79] using microspectroscopic techniques as in situ UV/Vis, confocal fluorescence and IR. In some of these papers, both MTO and ethanol-to-olefin (ETO) is discussed and compared. One of the conclusions of this comparison is that ETO results in a faster deactivation of the catalyst due to the direct formation of ethylene, which is the main coke precursor. For MTO there is no such competing reaction. Furthermore, the findings lead to the conclusion that completely different pathways exist for the MTO and ETO process. Again the 400 nm absorption band is found and assigned to polymethylated benzenes. This absorption band is monitored in function of temperature and linked to the reaction rate. This way, an activation energy for the intensity can be found and for MTO this is found to be equal to 98 kJ/mol. This value shows a strong connection to the theoretical reaction barrier obtained for the methylation reactions in H-SAPO-34, which again emphasizes the importance of methylations in the MTO process.[77] Another conclusion of these papers is that two reaction stages can be distinguished for the MTO process. In a first stage, which includes the induction and active period, methoxy species, protonated dimethyl ether and polyalkylated benzenes carbocations are formed. It was found that these species do not yet affect the accessibility of the H-SAPO-34 crystal.[78] The role of the methoxy species in the active period was investigated in more detail. The depletion of the methoxy species matches nicely with the formation of alkyl aromatics, suggesting a relationship between them.[79] In the second stage, which is ascribed to the deactivation period, polyaromatic species are formed. These species are bulkier and found to interact with the acid sites leading to alter the accessibility of the H-SAPO-34 crystal. Furthermore, these species are relatively inactive during the MTO process.[78] These polyaromatic species are mainly formed at the border of the catalyst crystals, hindering the diffusion of reactants and products in- and outwards.[77,78]

3.1.2 H-ZSM-5

The second commercially used catalyst for MTH processes is the H-ZSM-5 zeolite, which has the MFI topology, as depicted in Figure 3.2. This framework consists of a 3D network of sinusoidal (5.1 x 5.2 Å^2) and straight (5.3 x 5.6 Å^2) channels defined by 10-rings leading to medium-sized pores.[69]

Since methylations are important reactions in the MTH processes there are some theoretical studies found in literature on the methylation reactions is H-ZSM-5. In a first paper by Van Speybroeck et al.[57] the methylation rates of ethylene, propylene and butene obtained via theoretical calculations are compared to experimental values. In the experiments, it was found that butene is more reactive than propylene, which has a higher methylation rate than ethylene. A good agreement between the theoretical rates and the experimental data was found and near "chemical" (deviations between 0 and 10 kJ/mol for the activation energy) and "kinetic" (deviations of less than a factor 10 for the reaction rate) accuracy was reached. In another paper of Moors et al.[59], the influence of methanol loading on the methylation of benzene was studied. A methylation can occur via two mechanisms, the stepwise and concerted mechanism, as was discussed earlier and depicted in Figure 2.9. In this paper, it was found that both mechanisms might take place. Furthermore, it was found that protonated methanol clusters are formed at high methanol loadings. Methanol clusters consisting of three molecules were found to have the highest formation probability. These cluster have as favorable result that the exact location of the Brønsted acid site (BAS) is not essential for the methylation reaction. A disadvantage of the formation of the methanol clusters is the higher free energy barriers found for the methylation compared to a single methanol. A more recent study analyzed the formation of the framework-bound methoxides, which are intermediates in the stepwise methylation mechanism, in more detail.[80] In this study, the formation of methoxide from methanol and dimethyl ether were found to occur via similar mechanisms. Furthermore, it was found that the effect of the presence of an assisting methanol, which in small cluster calculations was found to lower the enthalpy barrier, is less pronounced in the large cluster calculations. This indicates that the stabilizing effects of the zeolite framework largely outweigh the additional electrostatic stabilization of the assisting methanol. In contrast, molecular dynamics and metadynamics simulations with methanol as reactant and as assistant led to a decrease of the reaction barrier. This is because the reaction proceeds through a broader transition state region, mitigating the entropic penalty of the rigid transition structure obtained in the static calculation. This effect was not found if dimethyl ether is used as a reactant. Lastly, it was found that the methoxide species is as reactive as methanol and dimethyl ether in the methylation of alkenes.

An interesting influence to analyze is that of the topology on the type of deactivation via the comparison of H-SAPO-34 and H-ZSM-5.[21] In contrast to the trapped polyaromatics in the cages of H-SAPO-34, H-ZSM-5 is thought to deactivate by graphitic coke formation at the outer surface of the zeolite crystal. At low temperatures (270-300 °C), ethyl-trimethyl-benzene and isopropyl-dimethyl-benzene are formed by alkylation of benzene rings with ethylene and propylene and block the pore system leading to deactivation. However, at higher temperatures (300-400 °C), the alkylation of benzene rings with olefins is reversible and H-ZSM-5 is reactivated. Therefore, at temperatures of MTH processes, deactivating pore filling does not occur and external coking appears to be the only plausible cause of the loss of activity with time on stream. This coke formation is a rather slow process that is started from an olefin based "coke seed". This can react further with methanol via methylation and dehydrogenation, as depicted in

Figure 3.3. This coke formation is indicated by the methane found among the volatile compounds. The slow external coking process might explain the outstanding catalytic stability of H-ZSM-5.[81,82]

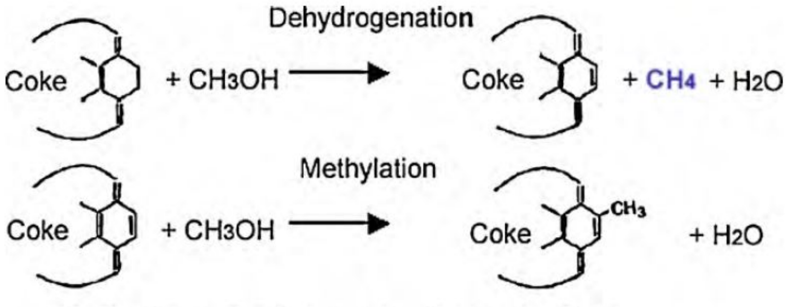

Figure 3.3: Representation of coke growth via methylation and dehydrogenation.[81]

3.1.3 Other catalysts

Other possible zeolite and zeotype catalyst are also considered and discussed in literature due to the ongoing search for the optimal catalyst for the conversion of methanol.[16,21] A short overview of some of the considered catalysts is given in this section.

A first catalyst that has been employed for mechanistic investigations, but not as a commercial catalyst due to rapid coke formation, is H-Beta featuring the BEA topology. This framework consist of a network of intersecting, straight channels, which are slightly larger than those of H-ZSM-5.[69] Due to these more spacious channels, steric hindrance is significantly decreased. This leads to the larger penta- and hexamethylbenzene as the most active aromatic HP species compared to the lower methylated methylbenzenes as intermediates in H-ZSM-5.[83] Since methylation reactions are thought to be very important in the MTH processes, it is instructive to look at a theoretical study by Lesthaeghe et al.[84] that compares the methylation of methylbenzenes for the CHA, BEA and MFI topology. The conclusion of this paper is that the geminal methylation of hexamethylbenzene has the following order of reactivity in function of the topology: $CHA \gg MFI > BEA$. The chabazite cage is found to have the perfect surroundings for a surprisingly stable heptamethylbenzenium cation (heptaMB$^+$), while the large beta cages favor neutral species over cations. The results for the MFI topology are similar to the experimental data mentioned earlier[83] as the lower methylated cations are found as the most likely intermediate.[84]

In literature, several papers compare different zeolite and zeotype topologies as a catalyst for MTH processes. An example is the study of Cui et al.[67] which compares H-ZSM-11 (MEL), H-ZSM-22 (TON), H-SAPO-34 (CHA) and H-SAPO-5 (AFI)[69] as catalysts for methanol conversion. The different topologies and some characteristic lengths are depicted in Figure 3.4. In this paper, methanol conversion over H-ZSM-11, H-SAPO-34 and H-SAPO-5 were found to be 90 %, 80 % and 70%, respectively. On the other hand H-ZSM-22 only showed a very low methanol conversion. Co-feeding experiments with toluene pointed out that this low reactivity is due to the small channels which limit the size of the intermediates and thus the aromatic cycles. Lower feeding rates give higher methanol conversions on H-ZSM-22 as was discussed in Section 2.2.2.

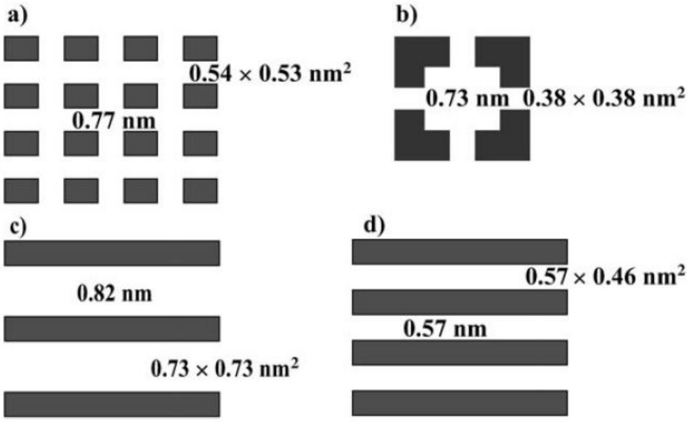

Figure 3.4: Representation of pore structures analyzed by Cui et al.[67]: a) MEL structure of ZSM-11; b) CHA structure of SAPO-34; c) AFI structure of SAPO-5; and d) TON structure of ZSM-22. The values inside the pores indicate the maximum diameter of a sphere that can be included in the framework, and those outside the pores indicate the size of the pore openings.[69]

Another study which compares different zeolite topologies for the MTH reaction was conducted by Teketel et al.[85] in which different one dimensional 10-ring zeolites are compared. The examined catalysts in this study are H-ZSM-22 (TON), H-ZSM-23 (MTT), H-ZSM-48 (*MRE) and H-EU-1 (EUO).[69] Experimental results from this paper show that H-ZSM-22 and H-ZSM-23 show similar product distributions which are characterized by the lack of aromatic species. On the other hand, the product distribution of H-ZSM-48 and H-EU-1 comprises substantial amounts of aromatics. For H-ZSM-48 this observation can be ascribed to the wider channels similar to those of H-ZSM-5. For H-EU-1, this explanation is not valid, since it has narrower channels than H-ZSM-22. Nevertheless, a plausible explanation is proposed by the authors. The H-EU-1 catalyst has 12-ring side pockets on the outer surface of the crystal during MTH reaction, which are sufficiently large to allow diffusion of aromatics out of the crystal without passing through the narrow 10-ring channels.[85]

A similar study which compares the performance of different zeotype catalyst for the

MTO reaction was conducted by Dai et al.[86] comparing H-SAPO-34 (CHA), H-SAPO-11 (AEL), H-SAPO-41 (AFO) and H-SAPO-46 (AFS).[69] Just as H-SAPO-34, H-SAPO-46 possess a structure with cages, while the other two topologies consist of one dimensional 10-ring pore systems. The experimentally obtained product distributions for the different catalysts are depicted in Figure 3.5. A good performance of H-SAPO-34 for the MTO reaction is obtained as expected. Furthermore, H-SAPO-41 is found to have a stable selectivity to C_2-C_4 olefins of about 70 % with as extra advantage that its good performance is preserved for reaction times up to 10 h. On the other hand, selectivity to C_2-C_4 olefins for H-SAPO-11 drops down rather quickly during reaction, while H-SAPO-46 instantaneously has a low selectivity to light olefins and a high selectivity to DME. In both cases, the decreased activity is explained by the lower amount of Brønsted acid sites in these last two topologies compared to the first two.

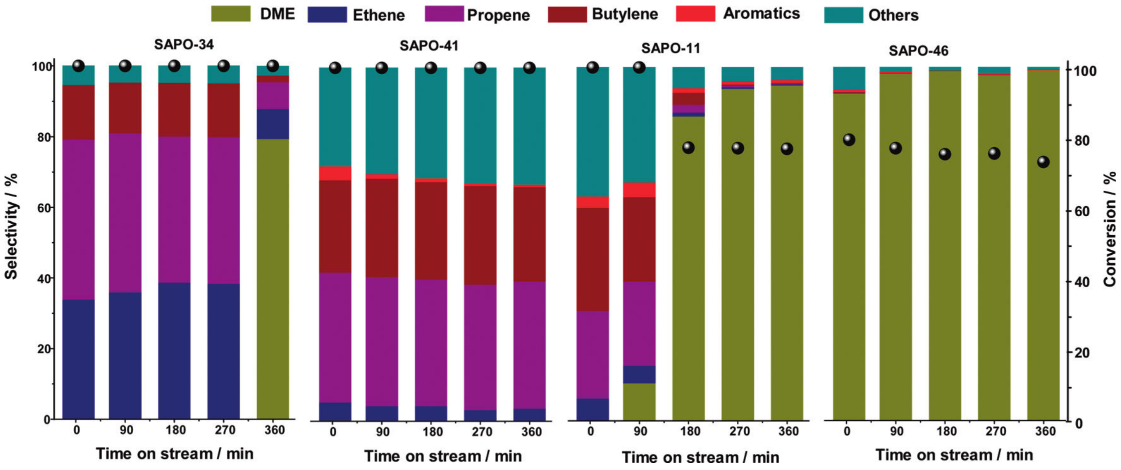

Figure 3.5: Methanol conversion and product distribution during MTO reaction on SAPO materials at 723 K up to a time-on-stream of 6h.[86]

There are still several other zeolite and zeotype catalysts considered for the MTO reaction, like for example H-ZSM-58[87], H-ZSM-34[88,89], etc. but these will not be discussed in detail in this dissertation.

3.2 Influence of water on MTO

Besides the used catalyst, also the operating conditions applied during reaction are important factors in the optimization of the methanol-to-olefin process. The optimal operating conditions for this process were already discussed in Section 1.3.[19] One of these operating conditions will be discussed in more detail in this section, namely the influence of water on the MTO process.

Water is an inherent byproduct of the production of methanol from synthesis gas. Since renewable pathways to chemicals are of great interest, it is interesting to look at the influence of the use of bio-derived syngas on the methanol production. This study was conducted by Yin et al.[90] where it is stated that the main difference between bio-derived syngas and syngas derived from natural gas and coal is that bio-derived syngas contains more CO_2 and less H_2. This thus results in a low H/C ratio and a high CO_2/CO ratio, which is not favorable for methanol synthesis under the conventional method. In the paper a new possible way of methanol synthesis is proposed and analyzed. One of the important results of this paper is that the increased CO_2/CO leads to a higher water content in the produced methanol. Though, the methanol yield can be improved by controlling the temperature, increasing the pressure, etc. Another option is to partially remove CO_2 from the syngas, but this will increase the capital cost of the plant.[90] Nevertheless, water will still be present in the produced methanol, so in case the methanol production unit is to be integrated with the MTO process, the influence of water on the MTO reaction is important. Nowadays, typically the methanol-water mixture is condensed and sent to a distillation column for separation. If a positive influence of the water on MTO process is found, separation can be omitted and this would lead to a remarkable reduction of the fixed and utility cost.[19]

The influence of water on zeolite catalysis has already been extensively investigated. An interesting experimental study on the adsorption of water and methanol in H-SSZ-13 and H-SAPO-34 was executed by Bordiga et al.[91] trying to solve the discussion whether water adsorbs combined with protonation to form hydronium (H_3O^+) ions or merely with the formation of hydrogen bonds with the Brønsted acid sites.[92–94] Their results showed that for H_2O:BAS ratios up to one led to the formation of neutral H-bonded complexes, while an excess of H_2O led to the formation of $H^+(H_2O)_n$ clusters. These clusters were mainly found in H-SSZ-13 and less in H-SAPO-34 due to the lower acidity of the latter.[91] The formation of the protonated water clusters might have a significant influence on the MTO reactions, since the proton might be less available for reaction in the cluster than on the Brønsted acid site.

Solvents might also have an influence on the reactivity in zeolite catalysis, like enhanced acidity and proton transfer.[95] An example is the increased or suppressed alkane C-H bond activation by the addition of water.[96] This study showed that water loading with H_2O:BAS ratios ≤ 1 increased isobutane C-H bond activation, while increased water content (ratios greater than 1-3) reduces the alkane reactivity. At even higher water loading, complete suppression was found. These results indicate that water can be an active participant in reaction involving hydrophobic molecules in solid acid catalysts, as long as the water concentration is essentially stoichiometric.

A first influence of water on the MTO reactions is found in the first stage of the process, namely when the equilibrium between methanol, dimethyl ether, water and framework-bound methoxide species is formed:[20]

$$2\ CH_3OH \rightleftarrows (CH_3)_2O + H_2O \tag{3.1}$$

$$CH_3OH + Z - H \rightleftarrows Z - CH_3 + H_2O \tag{3.2}$$

When water is added to the MTO feed flow the equilibrium of reactions 3.1 and 3.2 will shift to methanol. Since all three species are found to have similar reactivity towards methylation, it is expected that this change in equilibrium will not have a large effect.[56,80]

Some theoretical studies highlight the importance of water acting as a bridge between the HP species and the acid site of the catalyst. This is one of the characteristics of the full catalytic side-chain cycle to ethylene and propylene which has been proven.[63,64]

Several studies have been conducted which analyze the general influence of water on the MTO process. These studies all conclude that the addition of water to the methanol feed results in the reduction of the rate of coke formation and maximizes the selectivity to light olefins, as depicted in Figure 3.6.[19,60,97–99] The delayed coking might be explained by the reduction of olefin conversion to higher molecular weight coke species, because some of the acid sites are occupied by the polar water molecules. This prevents to olefins to undergo oligomerization and coking on the sites.[97,99] A possible explanation for the enhanced selectivity to ethylene can be found in the fact that the H_2O present in the nano cage introduces extra steric constraints. This shifts the selectivity in favor of ethylene, which is produced via the smallest transition state.[60]

A very interesting study concerning the effect of water on MTO reactions is the master dissertation by K. Wondergem.[100] In this work the influence is studied by the use of advanced in situ microspectroscopic techniques. By the use of UV-Vis microspectroscopy it was found that the induction time of the MTO process becomes longer upon increasing the amount of water. Furthermore, confocal fluorescence microscopy led to the conclusion that the distribution of species in the catalyst crystals becomes more even with increasing water content. This observation can be explained by the competitive adsorption between methanol and water. When no water is present in the crystal, methanol can adsorb on any Brønsted acid site to engage in the reaction, so it will not diffuse deep into the crystal. On the other hand, when water is present in the catalyst, it competes for adsorption on the acid sites, thus forcing methanol to diffuse deeper into the crystal to find an available adsorption site. This explanation might also clarify the increased induction period. Another result of the confocal fluorescence microscopy is the increase of the coke crust at the edge of the crystal. This might also be due to the increased methanol diffusion. A last remark about this paper is on the results of the infrared microspectroscopy. The different evolutions in the formation of C-H stretching bands

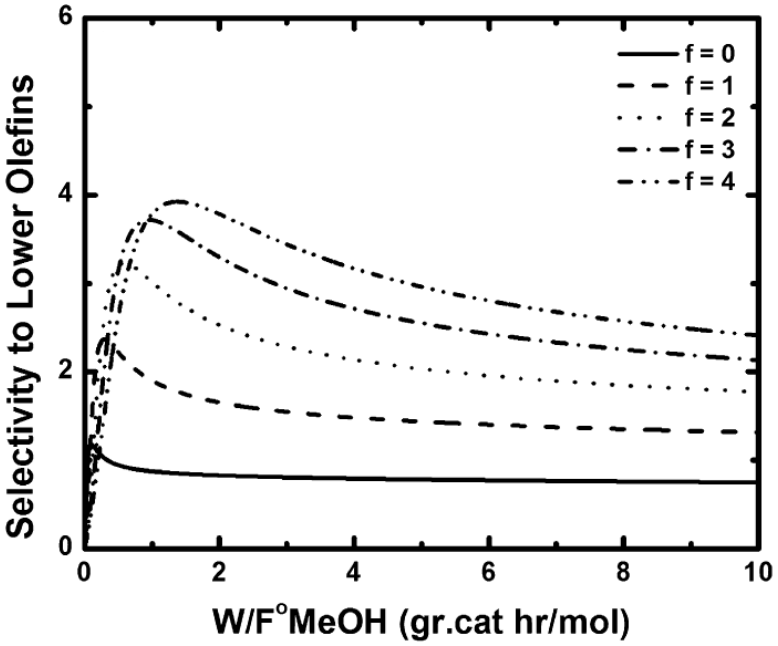

Figure 3.6: Influence of the water:methanol ratio, f, on the selectivity to light olefins.[19]

are found to be an indication that water has an influence on the formation of species in the hydrocarbon pool. This influence can be either by participating in reactions leading to changed ratios between different alkylated aromatics or by making the crystal more accessible resulting in a more homogeneous distribution of species.[100]

3.3 Objective of this master dissertation

Due to the theoretically and experimentally found influences of water on the MTO reactions, as described in Section 3.2, it seems interesting to analyze this effect even further. The basic objective of this master dissertation is to study the influence of water on the methanol conversion in H-SAPO-34, more specifically on the free energy barriers of the side-chain mechanism depicted in Figure 3.7. This influence will be assessed by means of theoretical calculations, namely ab initio molecular dynamics (AIMD) and metadynamics (MTD) simulations. These techniques will be explained in more detail in Chapter 4. These simulations will be executed on four different cases, as depicted in Figure 3.8, in order to unravel the water effect. Besides these four cases, an empty catalyst framework is simulated to have a reference.

In the first part of this thesis, the influence of water on the framework flexibility, movement of the aromatic species and framework deprotonation is analyzed via the results of the AIMD simulations. The influence of different guest molecules on the unit cell

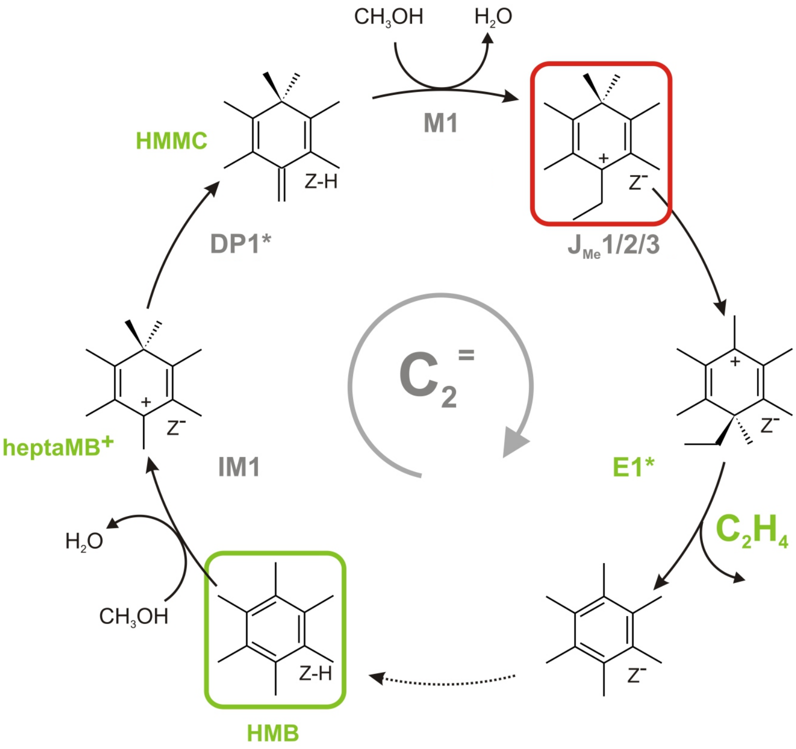

Figure 3.7: The side-chain mechanism for the production of ethylene in the MTO process.[64]

dimensions was already analyzed experimentally by Wragg et al.[70] The results of the ab initio molecular dynamics simulations of hexamethyl benzene in the four cases will show whether these results can be reproduced via theoretical calculations. The comparison of Case 1 with the empty unit cell will show the influence of hexamethylbenzene (HMB) on the unit cell parameters and volume. Furthermore, comparison of Case 1 and 2 will show the influence of methanol on the parameters and volume and comparison of Case 3 and 4 will show the influence of water. Additional examination of these results will show whether these unit cell variations have an influence on the behavior of the aromatic intermediates contained in the framework. Subsequently, the influence of water on the proton mobility in the catalytic framework will be analyzed by comparison of the framework deprotonation probability for the different intermediates of the side-chain cycle, depicted in Figure 3.7, for Case 3 and 4. Lastly, the relative stability of the intermediates will be discussed by looking at the average potential energy of the ab initio molecular dynamics simulations.

In the second part of this master dissertation, the reaction barriers of the different reactions depicted in Figure 3.7 are calculated from the MTD simulations. Since the entire cycle will be simulated for Case 3 and Case 4, the influence of water on these reaction barriers can be analyzed. Furthermore, the obtained reaction barriers can be compared to the literature results of the same cycle obtained with static calculations[64], showing

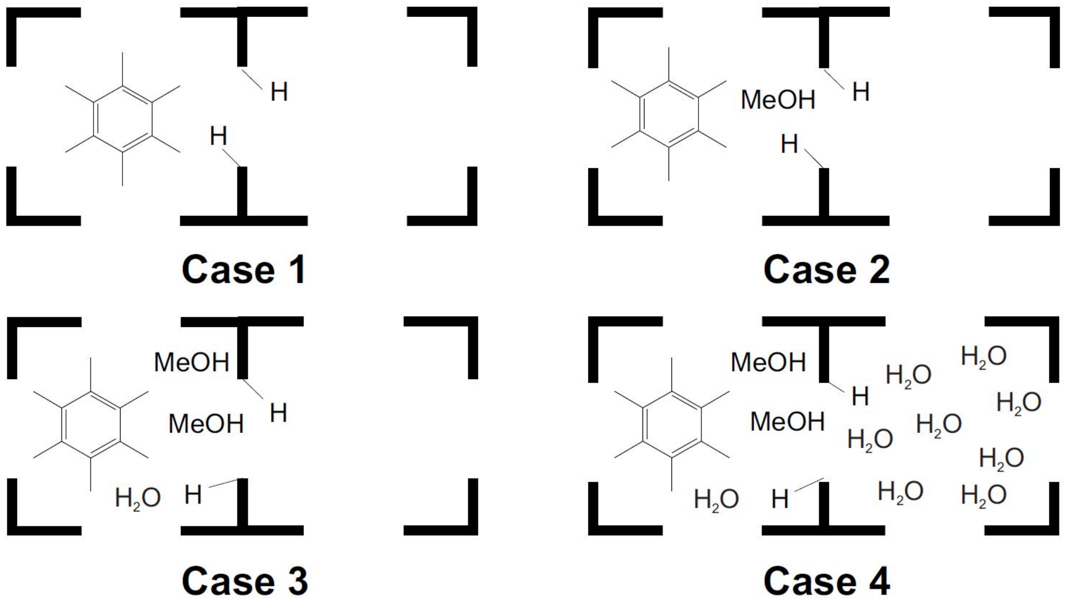

Figure 3.8: The four cases which will be compared via theoretical calculations in order to unravel the influence of water on the MTO process.

the differences between static and dynamic simulations. Additionally, a first insight into the competition between the side-chain and paring mechanism will be obtained, since the first reaction in the paring mechanism (the ring contraction of heptaMB$^+$ as depicted in Figure 2.8) will also be simulated.

Chapter 4

Computational methods

In this master dissertation, the influence of water on the MTO reaction is assessed based on results from ab initio molecular dynamics (AIMD) and metadynamics (MTD) simulations. In this chapter, the use of ab initio simulations in heterogeneous catalysis will be discussed by explaining the basic principles and techniques and by describing how they are used in this master thesis.

4.1 Quantum mechanical methods

When using quantum mechanical methods to describe a system, the Schrödinger equation for the many-body problem is solved. To solve this equation, the Born-Oppenheimer (BO) approximation is assumed in order to separate the effects of the electrons and nuclei.[101] Several methods have been developed to solve the electronic Schrödinger equation within the Born-Oppenheimer approximation. These methods can be divided into three categories: ab initio methods, density functional methods and semi-empirical methods.

4.1.1 Ab initio methods

Ab initio methods try to describe the system based on the first principles of quantum mechanics. When solving the electronic Schrödinger equation, the main problem encountered is the description of the interaction between the multiple electrons. An example of an ab initio method is the Hartree-Fock method where the system is approximated by an independent particle model. Furthermore, the electron-electron interaction is substituted by a mean field wherein the electrons move. The exact N-body wave function is approximated by a single Slater determinant. The Hartree-Fock equation used to solve the system contains a new operator called the Fock operator. This operator consists of two types of contributions. On the one hand, there are contributions that can be described exactly, namely the kinetic energy of the electrons and the attraction energy between electrons and nuclei. On the other hand there is the contribution of the electron-electron repulsion energy that is described by the mean field approximation. In this method, the electron correlation energy is neglected meaning that it will always result in a too high energy due to a loss of a part of the stabilization energy. Due to the fact that the mean field in the Fock operator depends on the one-particle orbitals which are the solutions of the Hartree-Fock equations, this is a numerical, iterative method. The orbitals are recalculated until the field induced by the orbitals and the orbitals induced by the field are consistent. Therefore, this method is also called the self consistent field method.[101]

Nowadays, more advanced methods are available which include parts of the correlation energy to obtain better results. An example of these post-Hartree-Fock methods are the Moller Plesset perturbation methods that use addition terms to the Fock operator like the two body interactions.

4.1.2 Density functional theory

An alternative method for solving the electronic many-body problem is the density functional theory (DFT). This method is based on the fact that there exists a unique relation between the electron density ρ and the wave function in the ground state as stated in the first Hohenberg-Kohn theorem.[101,102] Furthermore, the second Hohenberg-Kohn theorem provides a variational principle to find the ground state electron density. A solution for the ground state electron density is obtained by solving the Kohn-Sham equations which resemble the Hartree-Fock equations, but correlations are incorporated in contrast to the Hartree-Fock mean field. Nevertheless, this correlation energy can be overestimated which might lead to an energy lower that the real energy when using DFT methods, while Hartree-Fock energies are always upper limits. An exact description of the system will be obtained if the exchange-correlation functional is exactly known.[101]

The main challenge of DFT is to find a good approximation for the exchange-correlation energy functional. Several functionals have been proposed based on either parameters fitted to experimental data or without empirical input. Therefore, DFT methods are often referred to as semi-empirical methods[101], but the experimental input is very limited and depends on the choice of the functional.[103] The use of these fitted parameters can possibly lead to errors when the system, on which the experimental data is based, is left. The proposed functionals are often split up in the correlation energy and exchange energy part. When calculating a system, a combination of the proposed correlation functionals and of the proposed exchange functionals can be made. The many functionals can be subdivided according to their computational complexity and accuracy. The more complex the functional, the more accurate the result should be, but also more computational power will be required.[101,103]

The simplest set of functionals use the local density approximation (LDA), which only uses the electron density in a single point. These functionals are computationally interesting, though the results are not very accurate due to an underestimation of the exchange energy.[101]

An improvement of these functionals can be obtained by including the gradient of the density into the functional. This can be interesting since the slope of the density gives information on where you are in the molecular system. A large slope indicates points near the nucleus while small slopes indicate points far from the nucleus. These types of functionals are generally referred to as generalized gradient approximations (GGA). Again several functionals are proposed. On the one hand there are those which are based on fitted parameters like the Becke exchange functional and the LYP correlation functional.[101] On the other hand, there are other functionals like PBE and revPBE that do not try to satisfy as much characteristics of the real functional as possible, like for the PW91 functional developed earlier. Instead, the development of this functional focuses on the fact that all parameters introduced are fundamental constants.[104]

A following step in the advancement of the functionals is the use of hybrid methods that use the fact that Hartree-Fock methods correctly implement the exchange energy without any correlation. An example of this type of functional is the B3 exchange functional which consists of three contributions, namely an LDA contribution, a Hartree-Fock exchange energy and a exchange energy as introduced by Becke. This exchange functional combined with the LYP correlation functional is widely used in theoretical calculations.[101]

The GGA can be further extended to meta-GGA (MGGA) functionals by using the non-interacting kinetic energy density τ as an extra input tot the functional. Even more advancements can be introduced[101], but these will not be discussed in this master thesis.

A major drawback of the DFT methods is that they typically fail to model long-range dispersion interactions. Dispersion interactions depend on electron correlation, but long-range dispersion is typically neglected in DFT since the exchange-correlation term is assumed to be a functional of the local electron density or of the gradient. A consequence of this assumption is that only local contributions to the electron correlation are included. Two solutions are suggested to solve this problem. On the one hand, the functionals can be parametrized to systems which are governed by dispersion interactions, leading to functionals that are capable of modeling dispersion interactions. Examples are the M05 and M06 functionals.[101] On the other hand, it is possible to correct the DFT total energy with an empirical dispersion term. This scheme called DFT-D[105] was introduced by Grimme and included a semi-empirical correction to the energy of the system by the use of a R^{-6} term (in which R is the internuclear interaction). Since the dispersion energy is calculated separately from the DFT energy, this method is computationally inexpensive but leads to good results.

4.1.3 Semi-empirical methods

A third approach to solve the many-body problem is to use empirically parameterized methods that are computationally less demanding than the options discussed before. These semi-empirical methods start out from the ab initio formalism and then neglect many smaller integrals to speed up the calculations. Errors are introduced due to these approximations, which are compensated by inserting empirical parameters into the remaining integrals. These parameters are fitted against empirical or theoretical reference data.[106,107]

Generally, the energies which are obtained via these types of functionals are not very accurate, but they are very adequate to optimize the geometry of the system. Therefore, semi-empirical methods, like PM6[108], are used to obtain a geometry close to the optimum. This geometry is then used as input for a calculation with a more advanced and theoretical method in order to obtain reliable energies. This will lead to a reduced computational cost.[101]

4.2 Basis set

The main objective when solving the Schrödinger equation is to obtain the energy of the ground state of the system. This reduces to an eigenvalues problem where the wave functions of the molecule are the eigenfunctions. Every molecular orbital can be approximated by a linear combination of atomic orbitals (AO) that are centered on each atom present in the molecular system. Subsequently, these AO can be described by a linear combination of Slater type orbitals (STO). These STO are however computationally not the optimal choice. This problem can be circumvented by approximating the STO by functions that are computationally more interesting. Therefore, a basis set of Gaussian type orbitals (GTO) are introduced. These orbitals have as disadvantage that their behavior deviate quite strongly from that of the AO, so linear combinations are needed. When describing the system using GTO a separation is generally made between the core and the valence electrons. Since the most interesting part of the calculations is situated in the valence electrons, these need to be described more accurately. Therefore, the valence electrons are approximated by a linear combination of more GTO than the core electrons.[101]

Another option to represent the basis set makes use of plane waves (PW). The idea behind this basis set is that the interstitial density varies smoothly and is thus easily representable in a plane wave basis, while the rapidly varying density close to the nuclei can be represented by pseudopotentials. These integrate out the core electrons and lead to a smoothly varying density, which can be expressed in a limited number of PW.[109] The resulting, quite efficient algorithm is very interesting when using periodic boundary conditions.[109]

The above two basis sets can also be combined to have the best of both worlds. In this basis set, referred to as Gaussian plane wave (GPW) basis set, the smooth interstitial density is again represented by plane waves, while the rapidly varying density close to the nuclei is represented by localized Gaussian functions in this case.[109] This GPW basis set is implemented in the quickstep algorithm which is part of the freely available program package CP2K, which will be used during this master dissertation. Further information can be found in the paper by Van de Vondele et al.[110]

4.3 Ab initio calculations in heterogeneous catalysis

Obtaining kinetic data experimentally can be challenging when analyzing a heterogeneous catalytic system, since several reactions occur simultaneously. These side reactions need to be suppressed in order to only get information on the reaction under investigation. This can be a tedious job. Here, theoretical simulations offer the advantage that they enable isolating individual elementary steps and separating the influence of different properties such as topology and chemical composition.[21] So to get accurate kinetic data based on theoretical calculations it is important to have a good description of the effects of the zeolite framework on the reaction. In theoretical calculations, the catalyst framework can be taken into account in two manners, namely by a finite cluster of by periodically repeated unit cells.[21]

4.3.1 Finite cluster approach

In the first heterogeneous catalysis simulations, the zeolite framework was limited to a simplified model of the catalyst due to limitations of the computional power. Only the most essential parts of the catalyst were taken into account. These cluster were usually denoted by nT clusters where n is the number of tetrahedral atoms (Si, Al and P in zeolite and zeotype catalysis). In the early calculations, 3- or 5T clusters were used in gas phase computations. In these simulations, the influence of the framework is completely disregarded.[21] Due to the increases in computational power and in efficiency of algorithms, larger clusters can be used in the simulations which makes it possible to account for topology effects. Nowadays, clusters of around 45T atoms are typically used.[61,64,80] In these clusters, the bonds that were cut off by using a finite cluster are saturated by using hydrogen atoms. These hydrogen atoms are fixed in space in order to prevent the framework from collapsing. This leads to a disadvantage of this type of representation of a zeolite framework. By fixating the hydrogen atoms, the flexibility of the framework, which is a known characteristic of zeolites, is hindered.

An advanced method that reduces the computational cost for increasing the size of the used cluster are methods that combine quantum mechanics (QM) with lower level of theory methods as molecular mechanics (MM) or force fields. In the simulations, the most interesting part is the center of the cluster where the reaction occurs. These methods make use of this characteristic by using a high level of theory to describe the reactive center and lower level of theory to describe the surroundings. This technique is known as the QM/MM method.[101]

4.3.2 Periodic approach

An alternative to the finite cluster approach is the use of periodic boundary conditions. This approach is based on the fact that zeolites consist of periodically repeated unit cells. In these types of simulations, a unit cell is used and periodic boundary conditions are implemented to represent an infinitely large crystalline material. One must be careful when using the periodic approach that unphysical interactions between the different periodic images are prevented when using small unit cells.[21]

Although the periodic approach seems like an ideal way to represent the real zeolite framework, it has some shortcomings. Real catalyst materials are known to be heterogeneous[111], for example in the distributions of active sites or defects, which cannot be captured by fully periodic structures.[21] Furthermore, a wider variety of computational methods like the most recent functionals cannot yet be used in periodic calculations, but can be used on finite clusters. Also, the methods to localize the transition states are well established for cluster calculations.[21]

4.4 Ab initio molecular dynamics

4.4.1 The iterative procedure behind AIMD

In the past, ab initio simulations were mostly executed on stationary systems obtained after geometric optimization of the potential energy surface at 0 K. Additional information can be obtained with ab initio molecular dynamics (AIMD) simulations compared to static calculations as these are able to account for dynamical effects as framework flexibility, temperature effect, entropy influence and the influence of surrounding solvent molecules on chemical reactions.[22] A more thorough sampling of the potential energy surface with AIMD methods will lead to insights into the different possible stable structures and the transitions between them, as can be seen on Figure 4.1.

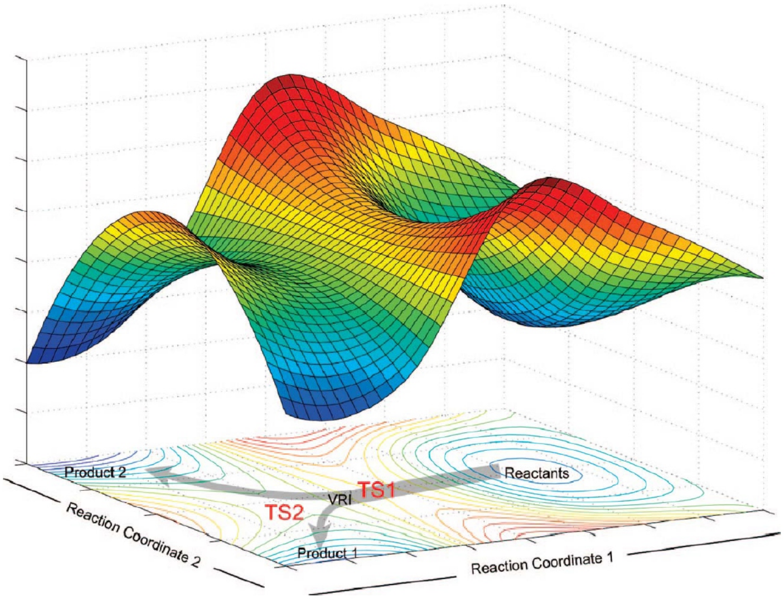

Figure 4.1: Schematic representation of a potential energy surface.[101]

To sample the potential energy surface with AIMD, the simulations start with an initial structure. Based on this initial structure, the electronic structure is calculated via a quantum mechanical method like DFT, leading to a potential V. The movement of the atoms during the next time step is described by Newton's second law as given in Equation 4.1. This movement can be considered classically, since the cores are heavy and the electrons rearrange themselves fast enough to adapt to nuclear motion due to the Born-Oppenheimer approximation.[101]

$$M_I.\overrightarrow{a_I} = \overrightarrow{F_I} = -\overrightarrow{\nabla} V \tag{4.1}$$

Where M_I is the mass of the nuclei, $\overrightarrow{a_I}$ is the acceleration of the atom nuclei and $\overrightarrow{F_I}$ is the force acting on the cores. When the forces acting on the atoms are calculated as the gradient of the potential energy surface, the new conformation for the next time step is obtained after the integration of Newton's law of motion. This step in the simulation immediately emphasizes the importance of the time step. On the one hand, this parameter should be small to describe the quick events that one wants to see, like molecular vibrations. On the other hand, smaller time steps are computationally more expensive and make it unfeasible to simulate for an extended period of time. Based on the new conformation, the electronic structure can be recalculated, leading to a new potential and new forces. This way an iterative procedure is obtained as shown in Figure 4.2.[101]

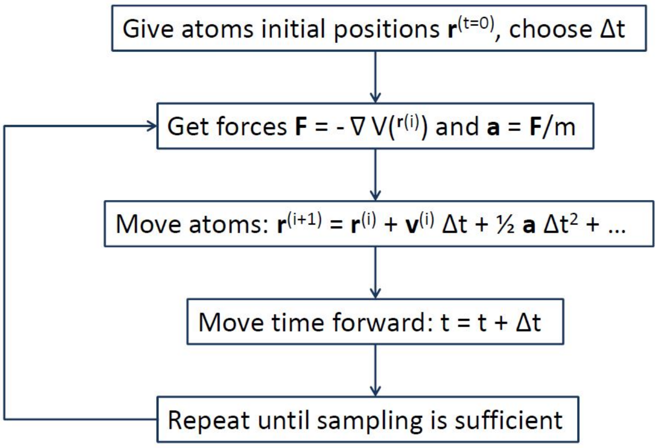

Figure 4.2: Schematic representation of the iterative procedure used in molecular dynamics.[101]

The most correct and straightforward method for molecular dynamics is to solve the electronic many-particles problem after each time step. This leads to a computationally very expensive method, known as Born-Oppenheimer molecular dynamics (MD), where only movement on the Born-Oppenheimer surface are considered. A serious reduction in computational effort can be obtained, while still considering the electronic structure on a quantum mechanical level, using the Car-Parinello approach.[112] In this method the equations of motions are constructed for nuclear and electronic degrees of freedom, leading to a coupling between both. Therefore, a fictitious kinetic energy for the electrons is introduced to be able to minimize the energy functional. This means that deviations from the BO approximation are possible. The solution only has a physical meaning when the fictitious kinetic energy remains small, so close to the BO surface. Furthermore, the Kohn-Sham equations are not calculated from scratch every timestep, but are based on the previous ones.[101,103,113]

4.4.2 Ensembles in MD

A purpose of MD simulations is to get insight in the average behavior of many-body systems. When an average is taken over all possible quantum states of a system, this is called an ensemble average. Nevertheless, in experiment and MD simulations, measurements are taken over time and a time average is obtained. In general, both averages are not equal, though most of the time they are assumed to be equal, which is referred to as the ergodic hypothesis.[114]

MD methods sample the system as a statistical ensemble, which means that every conformation is regarded as a possible state and that the simulation will eventually give the probability distribution for all the states of the system.[103] Molecular dynamics techniques are schemes for the study of the natural time evolution of a classical system of N particles in a volume V. Furthermore, the total energy E is a constant of motion in such simulations. So if the time averages are assumed to be equivalent to ensemble averages, then the obtained averages in MD simulations are equivalent to ensemble averages in the microcanonical (NVE) ensemble. It is however more convenient to perform simulations in other thermodynamic ensembles at constant temperature T in the NVT ensemble or at constant temperature and pressure P, leading to simulations in the NPT ensemble, since these are the process parameters defined in experimental studies.[114] To keep a constant temperature during the simulations, thermostatting methods are applied. Popular methods are rescaling velocities (Canonical sampling through velocity rescaling or CSVR), Nosé -Hoover thermostat, Andersen thermostat and Langevin thermostat.[101,114] In this master dissertation, the first two methods are used. In the CSVR method[115], the velocity is rescaled regularly by multiplication with a properly chosen random factor to match the target temperature. This method is ideal to equilibrate systems before executing the production run.[101] The second method used in this thesis is the Nosé -Hoover thermostat where an additional degree of freedom s is introduced to let the total energy of the physical system fluctuate.[116,117] This new dynamical variable s acts as a heat bath that can exchange energy with the physical system as represented in Figure 4.3.[101] Similarly, a barostat can be applied to control the pressure. In this master dissertation the MTK barostat is used.[118]

The importance of ab initio molecular dynamics simulations in determining the important intermediates and reaction paths is clear from comparative studies on the dehydrogenation and monomolecular cracking of propane by Bucko and Benco et al.[119–121] These studies clearly show the importance of entropic and temperature effects, accounted for in dynamic calculations. Especially the anharmonic interactions, which are intrinsically incorporated in the dynamic simulations, become more important at realistic process conditions. Furthermore, comparison between cluster calculations and large periodic models show the need to account for the flexibility of the catalyst framework.

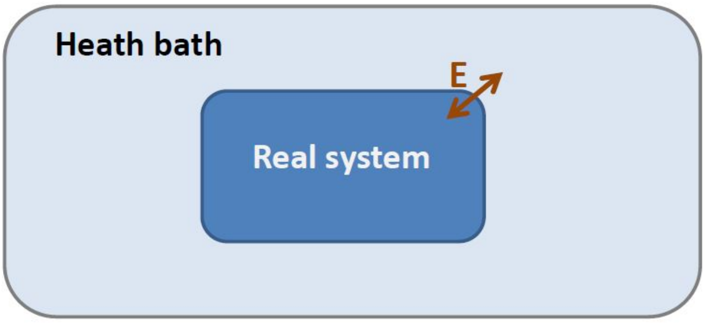

Figure 4.3: Schematic representation of the Nosé -Hoover thermostat.[101]

4.5 Metadynamics

During AIMD simulations, typically barriers of ca. RT (where R is the universal gas constant) can be crossed, leading to a good sampling of lowly activated reactions like proton transfers. As in literature much higher energy barriers are found for the reactions governing the MTO process[64], these are rare events during AIMD simulations due to their low probability. This limitation can be overcome by the use of advanced molecular dynamics techniques that use a kind of steering to force the chemical reaction to cross the barrier.[22] One of these techniques is used in this ab initio study, namely the metadynamics method, developed by Laio and Parrinello.[122,123] This is a very promising method to study zeolite-catalyzed reactions as was demonstrated in several papers discussed earlier.[59,80] In this method, the free energy surface (FES) can be reconstructed as a function of one or more collective variables (CV). These are reaction coordinates, like bond lengths or bond angles, by which the progress of the conversion of reactants into products during the chemical reaction can be represented. For zeolite-catalyzed reactions it is difficult to define the reaction coordinates, since multiple geometric characteristics change simultaneously during the reaction.[22] In this case, collective variables are defined as coordination numbers (CN), which are non-linear functions of characteristic bond distances during the reaction defined as:

$$CN = \sum_{i,j} \frac{1-(\frac{r_{ij}}{r_0})^{nn}}{1-(\frac{r_{ij}}{r_0})^{nd}} \tag{4.2}$$

This sum runs over two sets of atoms i and j with a distance r_{ij} between them. Furthermore, r_0 is a reference distance that depends on the bond type described by the CN. The parameters nn and nd are typically taken to be 6 and 12, respectively, to ensure a value for CN of 0.5 at the reference distance and a fast decay at larger distance. During the MTD simulations, the minima on the FES are filled along the collective variables by introducing Gaussian-shaped hills, as depicted in Figure 4.4a.[22] In this way the sampling of rare events is accelerated. The Gaussian bias potentials at any time t during a MTD simulation is given by: [122,124]

$$V_G(S(x), t) = w \sum_{\substack{t'=\tau_G, 2\tau_G, \ldots \\ t'<t}} \exp(-\frac{(S(x) - s(t'))^2}{2\delta s^2}) \tag{4.3}$$

In this formula, $s(t) = S(x(t))$ is the value taken by the CV at time t. Furthermore, three parameters enter the definition of the V_G:

- w, the height of the spawn Gaussian bias potentials.
- δs, the width of the spawn Gaussian hills.
- τ_G, the time interval between two added Gaussian bias potentials.

The basic assumption of the MTD technique is that the FES can be reconstructed based on the added Gaussian hills as they are assumed to provide an estimate for the underlying FES after a sufficiently long time period, as represented in Equation 4.4 and in Figure 4.4c.

$$\lim_{t \to \infty} V_G(S(x), t) \sim -F(s) \tag{4.4}$$

In case two collective variables are used to describe the reaction, a 2D FES is obtained. Based on these free energy surfaces, free energy barriers ($\Delta G^{\ddagger}$) can be calculated after the projection of this 2D FES onto a 1D surface. This is for example done by taking the difference (CV2-CV1) as reaction coordinate: [22,59]

$$G(CV2 - CV1) = -\frac{1}{\beta} \ln\{\int_{-\infty}^{\infty} d_{CV1} \exp[-\beta G(CV2 - CV1, CV1)]\} \tag{4.5}$$

Subsequently, the $\Delta G^{\ddagger}$ values can be calculated as the difference between the free energy of the transition state ensemble and the free energy of the reactant region on the obtained 1D FES: [22,80]

$$\Delta G^{\ddagger} = -\frac{1}{\beta} \ln \frac{\exp[-\beta G(TS)]}{\int_{-\infty}^{TS} \exp(-\beta G(s)) ds} \tag{4.6}$$

Where $\beta = \frac{1}{k_B T}$ with k_B the Boltzmann constant and TS is the position at the top of the barrier along the reaction coordinate s.

When more than two collective variables are necessary to describe the reaction, a projection onto a 1D free energy profile is not longer possible. To obtain reaction barrier from multi-dimensional free energy surfaces, the lowest free energy path (LFEP) method proposed by Ensing and co-workers will be applied. [125] In this method, a path is constructed that connects two free energy minima along the valley of lowest free energy.

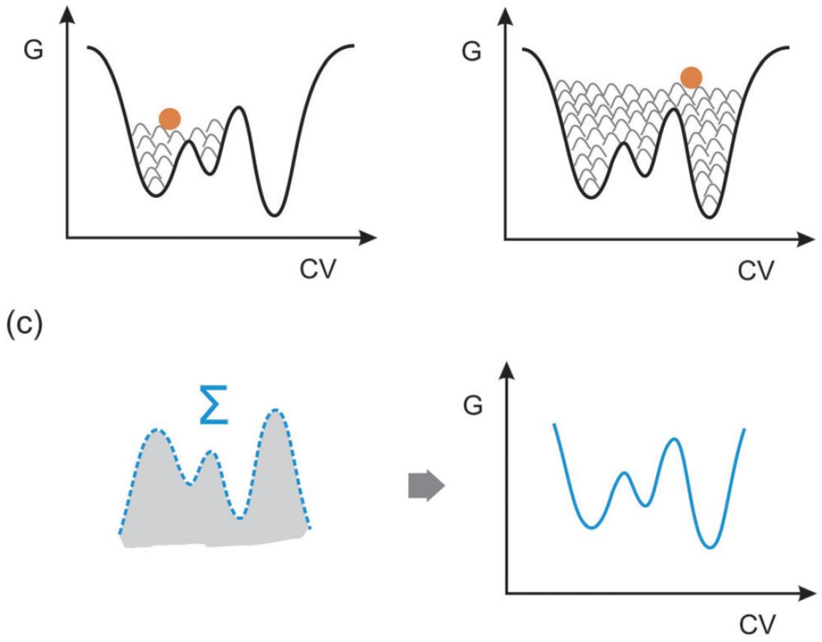

Figure 4.4: Schematic representation of the metadynamics technique. The minima of the free energy surface are filled with Gaussian-shaped hills (a). Once the all minima and all transitions are sampled (b), the free energy landscape can be reconstructed based on the inverse of the sum of the spawned Gaussian hills(c).[22]

4.6 Methodology used in this master thesis

To fully take the topology and the framework flexibility into account, density functional theory calculations were applied to a fully periodic catalyst model. All simulations in this master thesis were performed with the CP2K software package[110] using the combined Gaussian and Plane Wave (GPW) basis sets approach.[109,126] For these simulations, the revPBE functional was chosen because of its improved performance for solid-state calculations compared to the commonly used PBE functional.[127] Furthermore, the DZVP-GTH basis set and pseudopotentials[128] were used and Grimme D3 dispersion corrections[105] were added. For the simulations use was made of an H-SAPO-34 unit cell that contains 110 atoms. The catalyst framework is activated by the introduction of two Si substitutional defects and charge compensating protons, leading to Brønsted acid sites as represented in the unit cell in Figure 4.5.

The theoretical study was started by performing AIMD simulations of the cases represented in Section 3.3 to analyze the absorption of the molecules, the proton mobility, etc. and to have equilibrated starting structures for the subsequent MTD simulations. Therefore, the different intermediates and guest molecules were introduced into the unit cell, leading to starting structures as in Figure 5.2. To account for the framework flexibil-

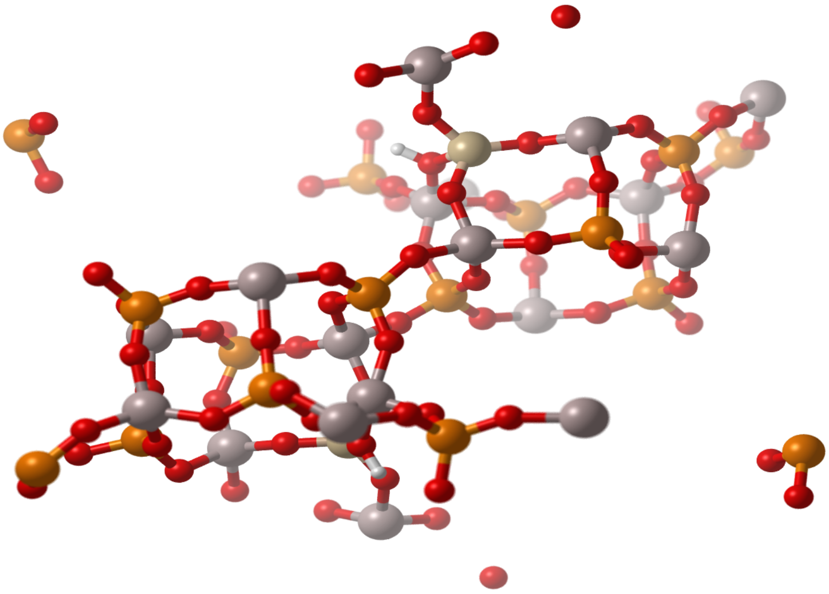

Figure 4.5: The unit cell of the H-SAPO-34 framework used in the simulations.

ity, the simulations were performed in the NPT ensemble at 623 K and 1 atm. The time step for integration of the equations of motion was set to 0.5 fs. The system was equilibrated for 1.25 ps using the CSVR algorithm[115]. These simulations were followed by a production run of 50 ps where the temperature was controlled by a chain of five Nosé -Hoover thermostats[116,117] and the pressure by a MTK barostat.[118] The geometric analysis of the production runs was performed using Visual Molecular Dynamics.[129]

Subsequently, metadynamics simulations are executed starting from the equilibrated structures obtained from the AIMD. These simulations are executed in the NVT ensemble, meaning that the volume and thus the unit cell dimensions should be kept constant. For these constant unit cell parameters, averages of the 50 ps production runs of the AIMD simulations are taken. The obtained average values are discussed for each reaction in Chapter 6. The simulations were also performed at 623 K and the temperature was controlled by a chain of five Nosé -Hoover thermostats.[116,117] The time step for integration of the equations of motion was set to 0.5 fs. The collective variables that were used to describe the different reaction steps are discussed for each reaction separately in Chapter 6. For all reactions the initial height of the Gaussian hills was set to 5.0 kJ/mol, close to the thermal energy RT, the maximum barriers crossed in an AIMD simulation. After each recrossing of the energy barrier, the height of the hills is halved to get a smooth energy surface. An exception on these initial hill heights are the methyl jumps. These were found to occur very fast and therefore the initial hill height was already halved, leading to initial hills of 2.5 kJ/mol. The width of the Gaussian hills was always set to 0.02.

Chapter 5

Influence of water on adsorption behavior

In this master thesis, the MTO reaction cycle in H-SAPO-34 is analyzed via dynamic simulations at realistic reaction conditions, namely 623 K and 1 atm. Nowadays, the hydrocarbon pool mechanism is accepted as the governing reaction mechanism for the MTO process.[36] In this mechanism, a hydrocarbon is trapped within the catalyst framework, acting as a co-catalyst in the MTO reactions. In catalysts exhibiting the chabazite topology, namely H-SAPO-34 and H-SSZ-13[69], the trapped organic molecules consist mainly of methylated aromatics. Based on the aromatic co-catalysts, two reaction cycles were developed, namely the side-chain and the paring mechanism. In the side-chain mechanism, the alkyl groups are formed via methylations of the side-chains, while in the paring mechanism ring contractions and expansions lead to growth of the alkyl groups.[16,21] The focus in this master thesis is on the side-chain mechanism, since a viable catalytic cycle based on HMB was proposed for this mechanism by De Wispelaere et al.[64] via static calculations at 670 K. Furthermore, since water is a byproduct of methanol synthesis and of the MTO process, it will always be present in the reaction environment.[19] Several experimental studies conclude that the addition of water to the methanol feed results in a reduction of the rate of coke formation and maximizes the selectivity to light olefins.[19,60,97–99] To get more insight in the influence of water on the MTO reaction, dynamic simulations with different water loadings are compared. The four considered cases are given in Table 5.1 and depicted in Figure 3.8.

In this chapter, the influence of the guest molecules, water and methanol, on the stability and behavior of the intermediates of the side-chain mechanism, listed in Table 5.2, will be analyzed based on the results of the 50 ps production runs of ab initio molecular

Table 5.1: The four water loadings considered to unravel the influence of water on the MTO reactions.

Name	Initial loading (aromatic species:methanol:water)
Case 1: reference	1:0:0
Case 2: no water content	1:1:0
Case 3: low water content	1:2:1
Case 4: high water content	1:2:9

dynamics (AIMD) calculations at 623 K and 1 atm. Interesting phenomenons that will be addressed are the framework flexibility, the proton mobility and the stability of the intermediates.

5.1 Framework flexibility

An important characteristic of heterogeneous catalysis is the framework flexibility, since it has an influence on possible diffusion limitations as discussed by Zimmerman et al.[130] In this paper, the influence of host-framework flexibility on the diffusion of methane in one dimensional zeolite pores was investigated. By taking framework mobility into account, the diffusion coefficient increased significantly compared to the rigid-lattice simulations.

As mentioned above, the effect of adsorption of methanol and water in H-SAPO-34 on the unit cell volume has been investigated by Wragg et al. via in situ and ex situ X-ray diffraction studies.[70] They concluded that the unit cell expands by 0.5 % when methanol is adsorbed, while the non-polar polymethylbenzene intermediates cause a significant expansion. In contrast, when water is adsorbed onto the framework it was found to contract by 2.0 %. Furthermore, the changes in the unit cell were observed to be very asymmetric, occurring mainly along the c-axis.

To see whether these effects are also found via theoretical calculations, the volume change of the four cases given in Table 5.1 relative to an empty H-SAPO-34 unit cell are compared. Therefore, the unit cell parameters and volume are averaged over the 50 ps production run of HMB in the four cases depicted in Figure 3.8. The results of these measurements are depicted in Figure 5.1.

Figure 5.1 shows that Case 1 leads to a 4 % expansion of the unit cell volume compared to the empty unit cell. The only difference between the two simulations is the introduction of HMB in the environment. Subsequently, the only difference between Case 1 and Case

Table 5.2: Abbreviations used for the intermediates of the side-chain mechanism depicted in Figure 3.7.

Abbreviation	**Description**	**Structure**
HMB	hexamethylbenzene	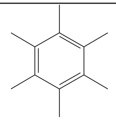
heptaMB$^+$	heptamethylbenzenium cation	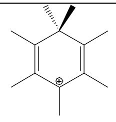
HMMC	1,2,3,3,4,5-hexamethyl-6-methylene-1,4-cyclohexadiene	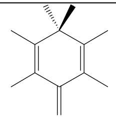
R$_{JMe1}$	Reactant of the first methyl jump	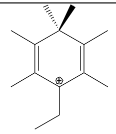
R$_{JMe2}$	Reactant of the second methyl jump	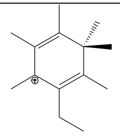
R$_{JMe3}$	Reactant of the third methyl jump	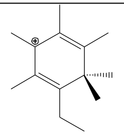
R$_{EthEli}$	Reactant of the ethylene elimination	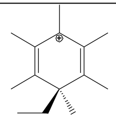

2 is the introduction of methanol in the unit cell, which leads to an additional 0.2 % increase in the unit cell volume. Lastly, the influence of the introduction of water in the catalyst environment can be analyzed by the comparison of Case 3 and Case 4, since the difference between these two simulations is eight water molecules. From this comparison it can be concluded that the adsorption of water on the framework leads to an 1.2 % contraction of the unit cell. The observed expansions and contractions are in line with the experimental results of Wragg et al.[70]

Analyzing the variations in the unit cell dimensions, which are also included in Figure 5.1, shows that these changes are anisotropic. For all cases, the main variation is along the c-axis, which corresponds well with experimental data from literature.[70,72] This anisotropic variation might be because the 8-ring windows, which are quite flexible, are parallel to the c-axis, while the more rigid 6-ring windows are perpendicular on this

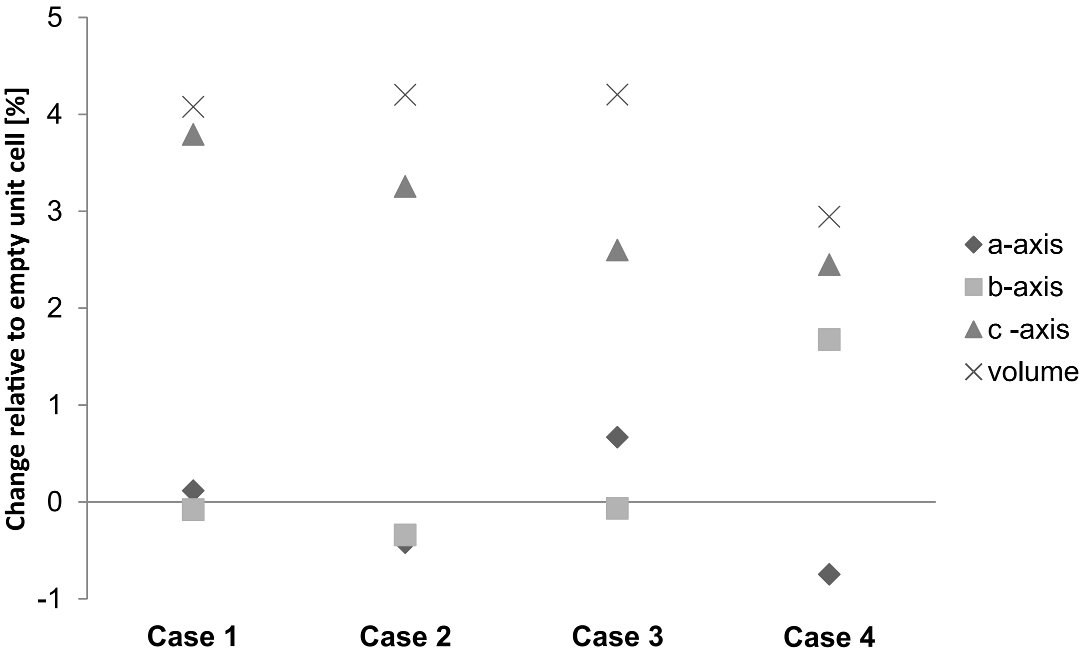

Figure 5.1: Average variation of the unit cell parameters and volume, relative to an empty H-SAPO-34 unit cell, over the 50 ps production run, at 623 K and 1 atm, of HMB.

axis. Lastly, the unit cell angles are not significantly altered by the introduction of guest molecules in the catalyst pores and remain close to 90 °, 90 ° and 120 ° for α, β and γ, respectively.

5.2 Mobility of the aromatic species

In the previous section, the introduction of water in the catalyst framework was found to lead to a contraction of the unit cell. It is now interesting to see whether this contraction leads to additional limitations on the mobility of the aromatic species. To analyze this, the ab initio molecular dynamics simulations of Case 3 (with a low water content) and Case 4 (with a high water content) for the different MTO intermediates (Table 5.2) are used. The simulations are started from initial structures as depicted in Figure 5.2a, c and e for HMB and heptaMB^{+}. Similar initial structures are used for the other intermediates listed in Table 5.2.

As can be seen by comparing Figure 5.2a and c, the cage containing the aromatic species always starts with three guest molecules, while the second cage is empty in Case 3 and contains 8 extra water molecules in Case 4. For all simulations, the three guest molecules in the cage with the aromatic species diffuse out of this cage and the aromatic species rotates to use the entire height of the cage, leading to structures as in Figure 5.2b, d

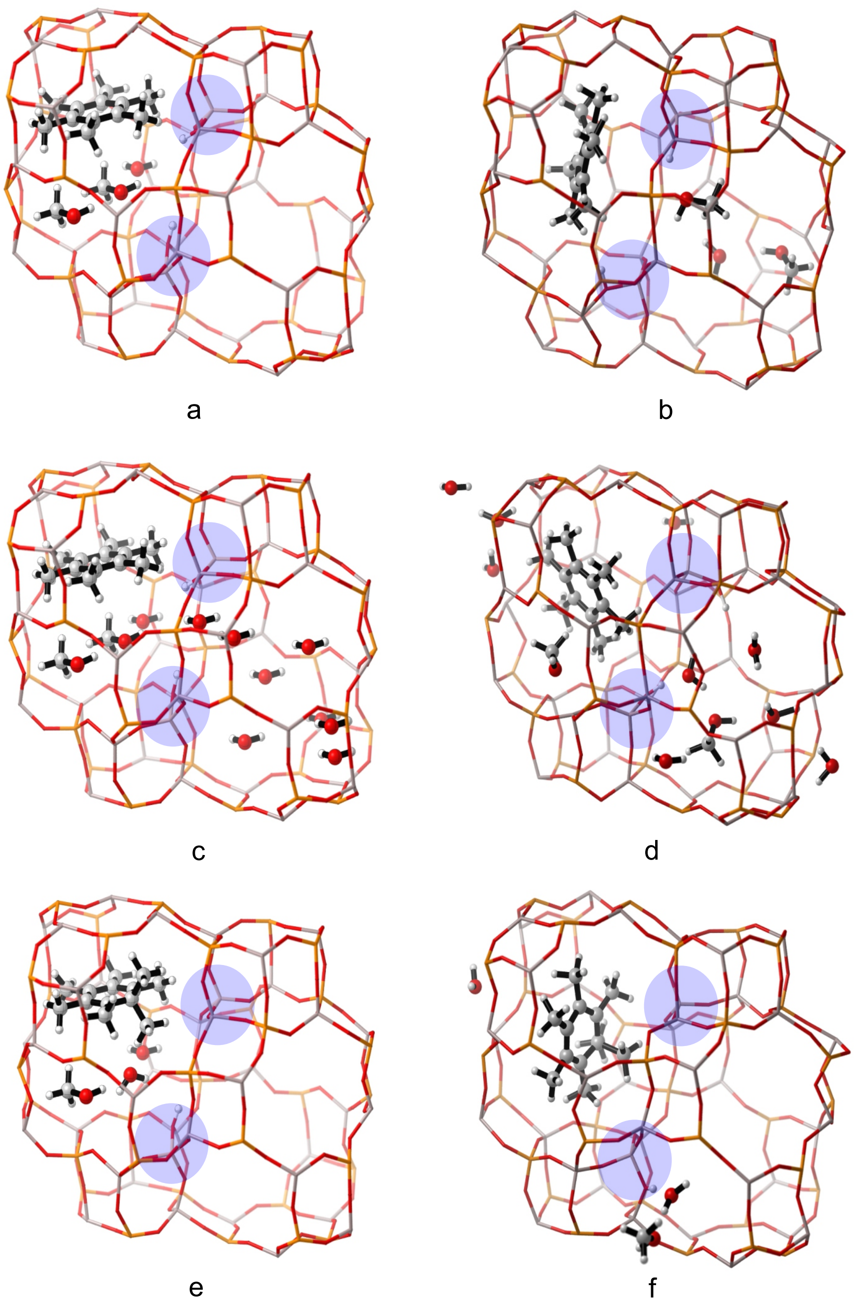

Figure 5.2: The initial structures used for the AIMD simulations of HMB at low (a) and high (c) water content and heptaMB$^+$ (e) at low water content. In (b), (d) and (f), the corresponding structures after 50 ps AIMD production runs at 623 K and 1 atm are shown. The Brønsted acid sites are highlighted in blue.

and f for HMB at low and high water content and heptaMB$^+$ at low water content. The reorientation of the aromatic ring can be analyzed by following the angle between the normals to the plane of the aromatic ring and the plane of the framework illustrated in

Figure 5.3.

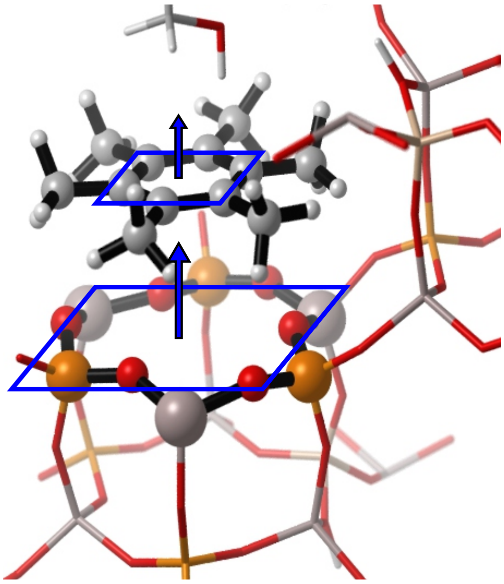

Figure 5.3: Representation of both normal vectors used in the analysis of the rotation of the aromatic species.

This angle is then plotted as function of the simulation time as represented in Figure 5.4 for HMB. Similar graphs for the other intermediates can be found in Appendix A. The angle between the two normal vectors always starts at a low angle, corresponding to the orientation in the starting structures, and converges to a value around 90 °, corresponding to the rotated structures. In some cases, the initial angle is already slightly higher (close to 40 °), because the rotation has already started during the equilibration time with the CSVR thermostat, as explained in Section 4.6.

Analysis of the time needed for this rotation to occur for the different intermediates leads to the following conclusions. First, a difference was found between HMB and the cationic intermediates (heptaMB$^+$, R$_{JMe1}$, R$_{JMe2}$, R$_{JMe3}$ and R$_{EthEli}$) at low water content. The reorganization takes more than 25 ps for HMB, while it only takes 5-10 ps in case of an ionic intermediate. This might be because HMB is smaller than all other intermediates, which would mean that the main driving force for the diffusion is that the aromatic species needs an entire cage for itself. Nevertheless, these observations are not confirmed by the simulations at high water content, since the rotation of HMB is very quick in that case. When comparing the high and low water content case for the cationic intermediates, no significant influence is found of the contraction of the unit cell due to the extra water present.

Because the interaction of the aromatic intermediate with the framework could depend on the composition of the catalyst, it might be interesting to examine whether the same

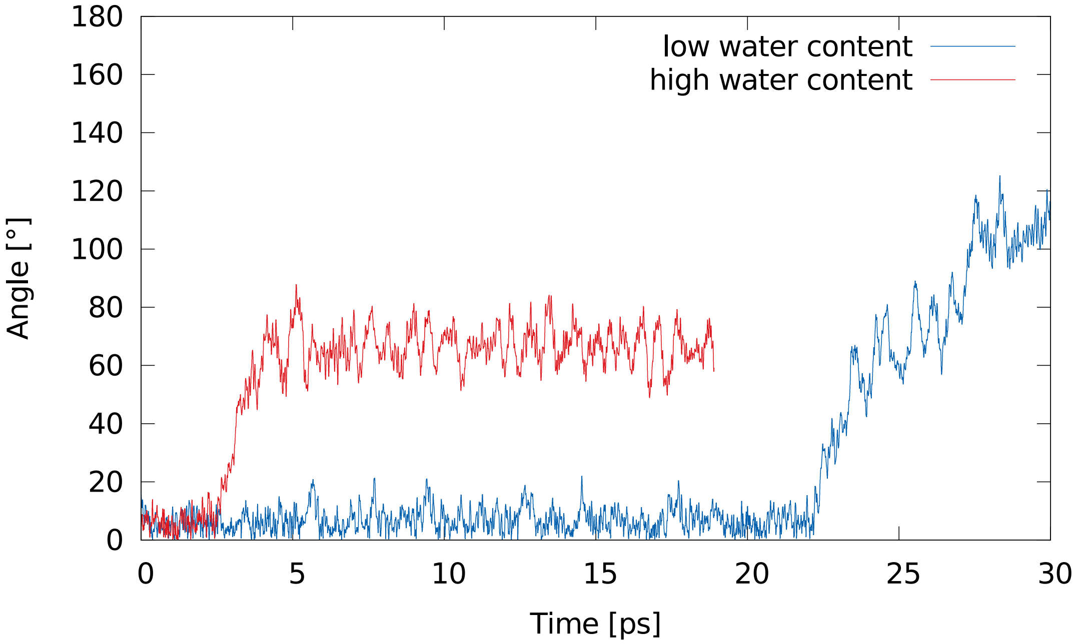

Figure 5.4: Angle between the normal of the plane of the aromatic ring and the normal of the plane of the catalyst framework indicated in Figure 5.3, as function of time for the AIMD simulation of HMB at 623 K and 1 atm.

rotation is found in H-SSZ-13. Therefore, an extra AIMD simulation was started in which the H-SAPO-34 environment was converted to an H-SSZ-13 environment. Due to time limitations, only the simulation for heptaMB$^+$ at high and low water content was executed and only a 25 ps production run was obtained. The simulations were started from similar starting structures, thus the same angle as for H-SAPO-34 can be followed to see whether the rotation occurs. This resulted in Figure 5.5, which clearly shows that this rotation also occurs in the H-SSZ-13 framework. When these results are compared to those of heptaMB$^+$ in the H-SAPO-34 framework depicted in Figure A.1, the results are quite similar. In both cases, the rotation is slightly faster in the low water content case and occurs in a comparable time interval, suggesting that the hydrophobicity or acidity of the framework does not play a major role in the rotation of the aromatic intermediate.

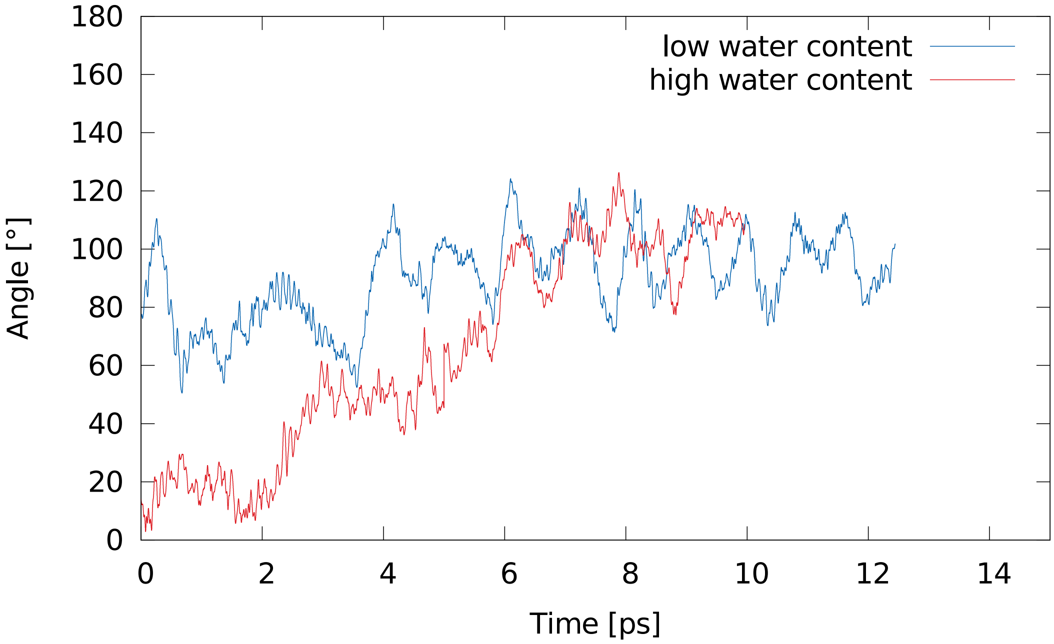

Figure 5.5: Angle between the normal of the plane of the aromatic ring and the normal of the plane of the catalyst framework indicated in Figure 5.3, as function of time for the AIMD simulation of heptaMB$^+$ at 623 K and 1 atm in the H-SSZ-13 framework.

5.3 Framework deprotonation

The Brønsted acid sites are an important characteristic of the MTO catalyst.[21] Furthermore, guest molecules might influence the behavior of this BAS due to competitive adsorption between methanol and water[80] or due to the formation of protonated clusters.[59,91] Therefore, the effect of water in the H-SAPO-34 environment on the deprotonation of the zeotype framework is investigated. For this analysis, the distance from the eight oxygens which are next to one of the two Si substitutional defects in the unit cell to all hydrogens that were originally bonded to an oxygen are followed during the 50 ps production run of all intermediates in both low and high water content cases. Examples of the bond distances that are taken into account are schematically represented by the dotted lines in Figure 5.6. From the analysis of the transition state for the deprotonation of the catalyst framework, a cutoff distance for the O-H bond length 1.3 Å is taken. A longer distance is considered as a deprotonation. Hence, the fraction of the simulation time in which the framework is deprotonated can be determined, resulting in Figure 5.7. The convergence of this data can be seen in the graphs given in Appendix B where the fractions are given after 30, 35, 40 and 45 ps of the simulation. These figures show that some fractions still change slightly, though the conclusions stay the same.

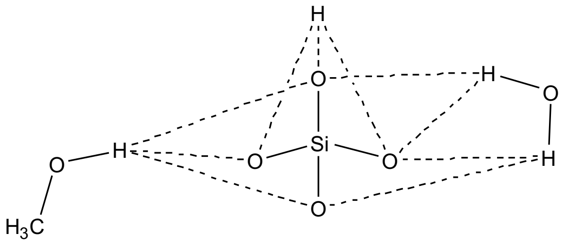

Figure 5.6: Schematic representation of the O-H bonds taken into account in the calculation of the deprotonation fraction of the catalyst framework.

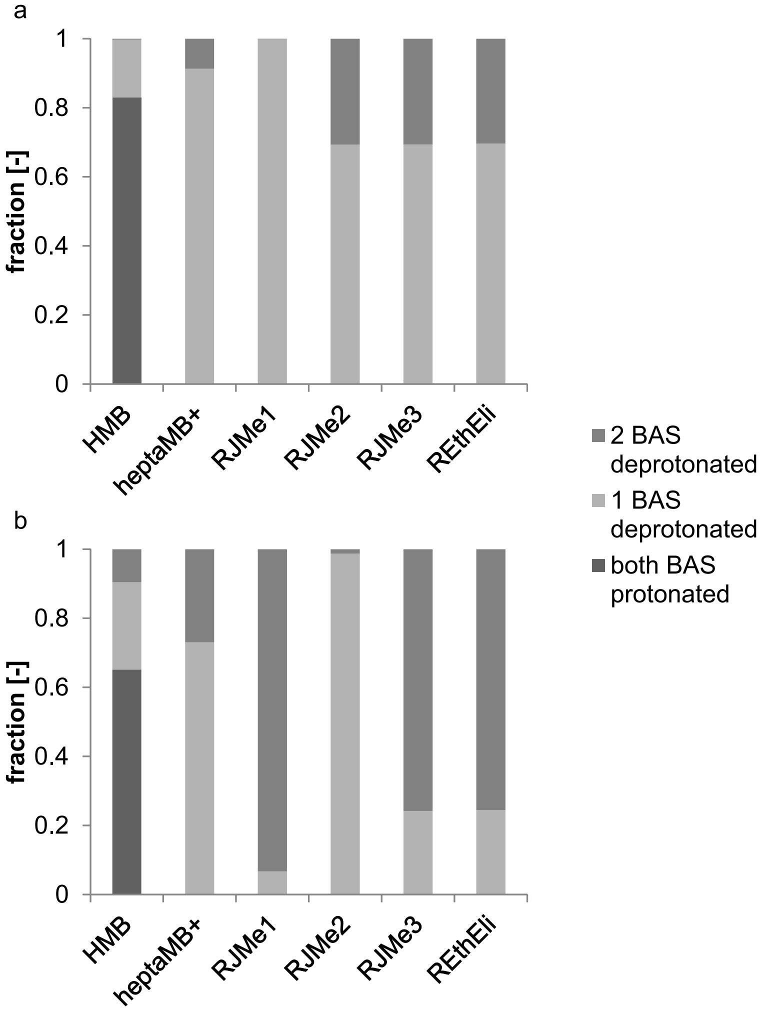

Figure 5.7: Fraction of the 50 ps AIMD simulation at 623 K and 1 atm in which the Brønsted acid sites of the H-SAPO-34 framework are (de)protonated for low water content (a) and high water content (b).

Notably, Figure 5.7, does not contain results for HMMC, because no full production run of 50 ps could be obtained. In a first attempt, the CH_2-group was found to interact with a random aluminum of the zeotype framework in the low water content case, as depicted in Figure 5.8a. In the case with high water content, HMMC was protonated to form heptaMB$^+$, but the formed OH$^-$-group survived in an acid environment (Figure 5.8b), which is not realistic. Therefore, new simulations were started in which the double bond was already close to the acid sites. In both the cases with low and high water content, the protonation of HMMC was found to be very rapid. Suggesting that this intermediate is not stable in the H-SAPO-34 environment. More insight into this instability will be provided when discussing the metadynamics simulations in Chapter 6.

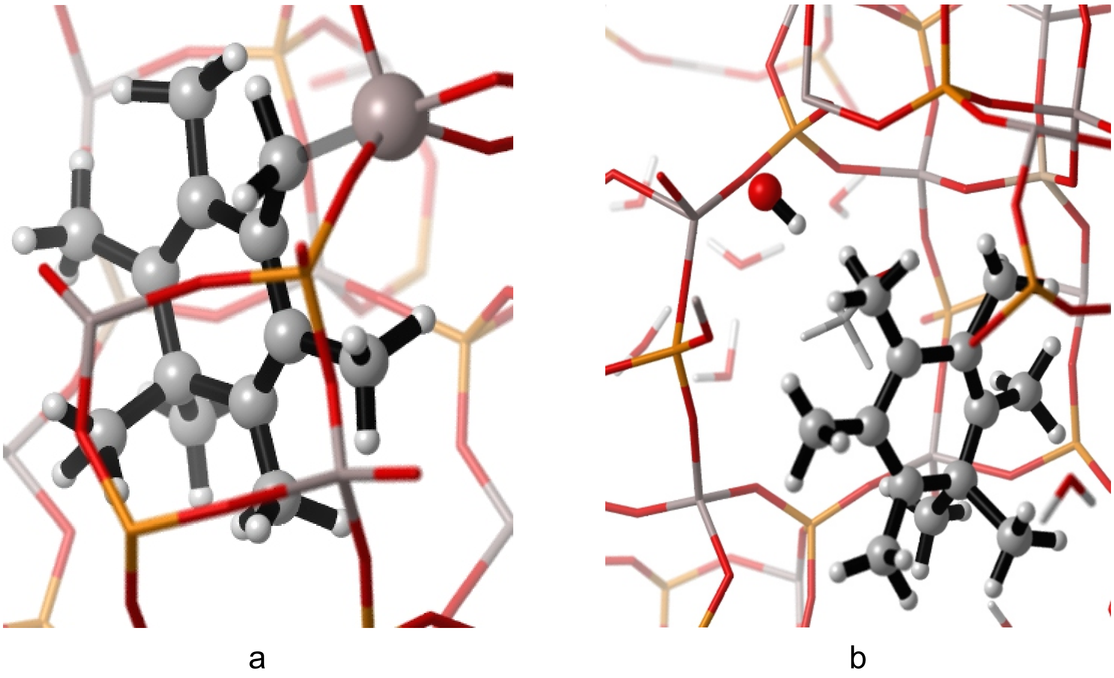

Figure 5.8: Snapshot of the abnormalities occurring during the AIMD simulations of HMMC at 623 K and 1 atm for the low (a) and high (b) water content case.

The comparison of Figure 5.7a and b leads to several conclusions. First of all, a difference can be observed between HMB and the cationic intermediates. For the cationic intermediates, maximum one BAS is present, because the formation of a cationic species consumes one acid site, which can be seen by the comparison of the initial structure in Figure 5.2a and 5.2e. Therefore, two BAS are only found in the simulation of HMB. Furthermore, a difference can be observed in the results for heptaMB$^+$ and the other cationic intermediates. The framework is less probable to deprotonate when heptaMB$^+$ as aromatic species, though no clear reason was found for this difference.

Subsequently, the simulations at low water content are compared to those at high water content. In most cases, the introduction of extra water in the catalytic environment leads to an increased probability to deprotonate the framework. At low water content, water is adsorbed on the BAS rather than protonated. A protonated cluster can be formed, but exists only for a short period of time, while at high water content, deprotonation of the framework leading to the formation of protonated water clusters is found more often and for a longer period. An example of both cases can be seen in Figure 5.9. The fact that more deprotonation occurs at higher water content shows that more than three water molecules are needed to form a stable protonated water cluster.

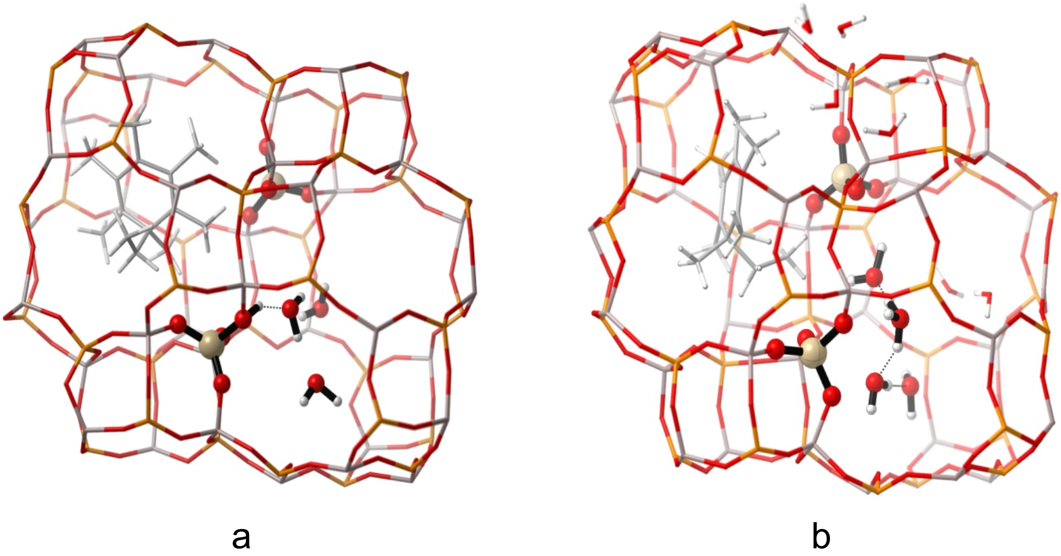

Figure 5.9: A snapshot of the AIMD production run at 623 K and 1 atm of EthEli at low (a) and high (b) water content. Snapshot (a) shows the water adsorption at low water content, while snapshot (b) shows the deprotonation of the framework and formation of a protonated water cluster.

There are two special cases, namely the simulation of R$_{JMe1}$ at low water content and of R$_{JMe2}$ at high water content. In these cases the deprotonation of the remaining BAS is very rare. This can be understood when looking at Figure 5.10, which shows a snapshot of R$_{JMe1}$ at low water content. At the start of the simulation, when guest molecules are still present in the cage with the aromatic species, the proton of the remaining Brønsted acid sites has been moved to another oxygen neighboring the Si substitutional defect. Afterwards, the guest molecules diffuse out of the cage and the cage is blocked due to the rotation of the aromatic species. Hence, the remaining proton becomes unavailable because the guest molecules never diffuse back to this cage after the rotation of the aromatic species. Therefore, deprotonation only occurs during the first part of these simulations and is thus rare. This event may not have a physical reason, but could depend on the initial structure or chance.

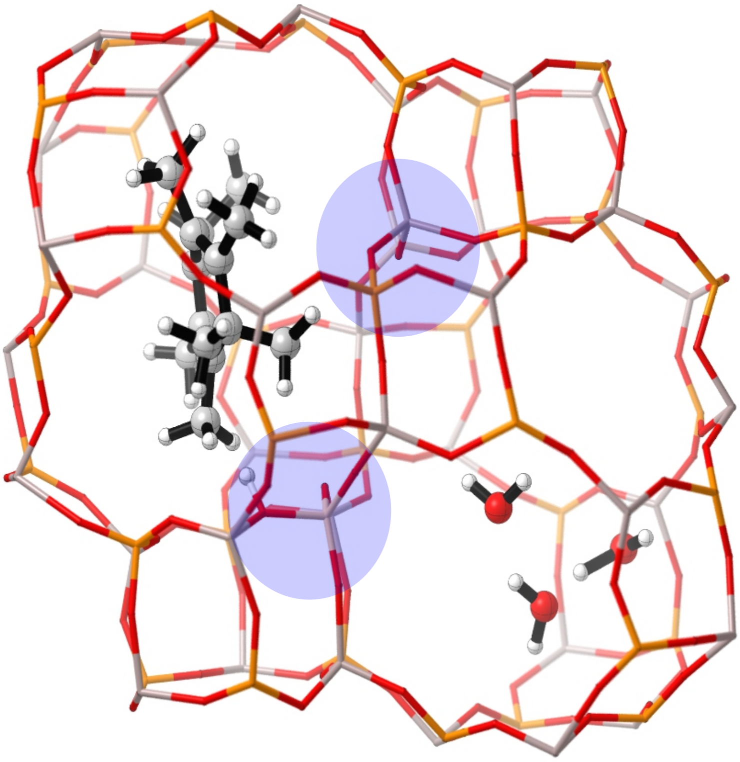

Figure 5.10: A snapshot of the production run of R_{JMe1} at 623 K and 1 atm with low water content showing the blocking of the Brønsted acid site, highlighted in blue, by the aromatic species.

Similarly as for the rotation of the aromatic species, it is interesting to see the influence of the composition and thus the acidity of the catalyst on the framework deprotonation. This can again be done by comparison of the result for heptaMB$^+$ in H-SAPO-34 with the simulation of heptaMB$^+$ in H-SSZ-13. When the same procedure as for H-SAPO-34 is followed, Figure 5.11 is obtained for the framework deprotonation fraction. Comparison of the results for H-SSZ-13 with the corresponding results for H-SAPO-34, depicted in Figure 5.7, immediately shows the effect of the higher acid strength of H-SSZ-13[76], since the framework has a significantly higher probability to deprotonate in both the low and high water content cases.

The BAS are especially important in the methylation reactions, since methanol needs to be protonated during this reaction.[59] Therefore, it is interesting to look in more detail to the simulations of HMB and see if the addition of water limits the protonation of methanol significantly. To this end, the distance from the oxygens of the methanols to all hydrogens originally bonded to an oxygen, as represented in Figure 5.12a, is followed during the production run. Similarly, the distance from the oxygens of the

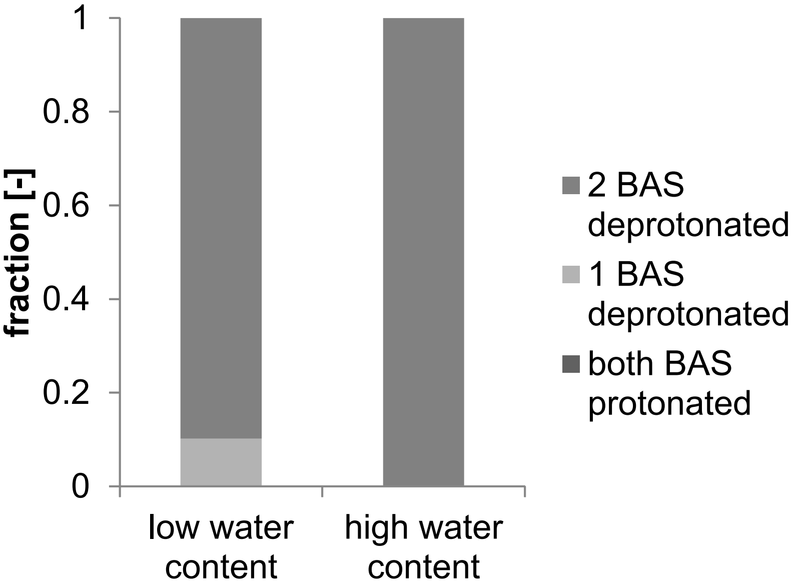

Figure 5.11: Fraction of the 25 ps AIMD simulation of heptaMB$^+$ at 623 K and 1 atm in which the Brønsted acid sites of the H-SSZ-13 framework are (de)protonated for low water content and high water content.

water molecules to all these hydrogens (Figure 5.12b) is followed. By again applying a cutoff of 1.3 Å for the O-H bond length, the fraction of the simulation time that methanol or water is protonated can be obtained, which is depicted in Figure 5.13.

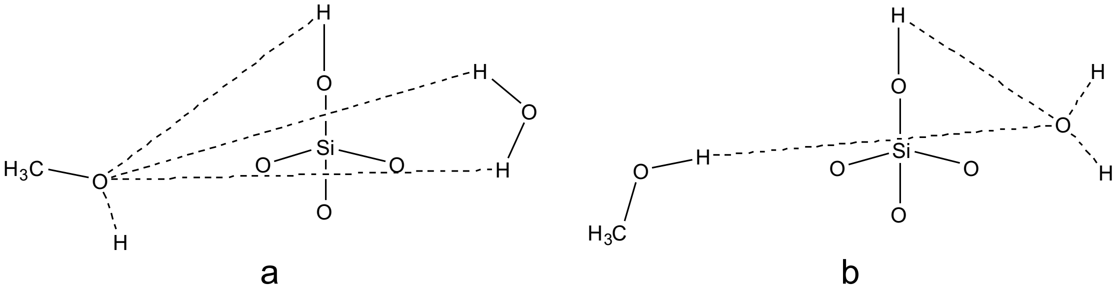

Figure 5.12: Schematic representation of the O-H bonds taken into account in the calculation of the protonation fraction of methanol (a) and water (b).

From Figure 5.13 it is immediately clear that the introduction of extra water in the catalyst environment has a significant influence on the protonation of methanol. At low water content, methanol is protonated for almost one third of the production run, far more than water. In contrast, the high water content case shows that water has now a higher probability to be protonated. This indicates that water and methanol adsorb competitively. Furthermore, water limits the activation of methanol in the catalyst

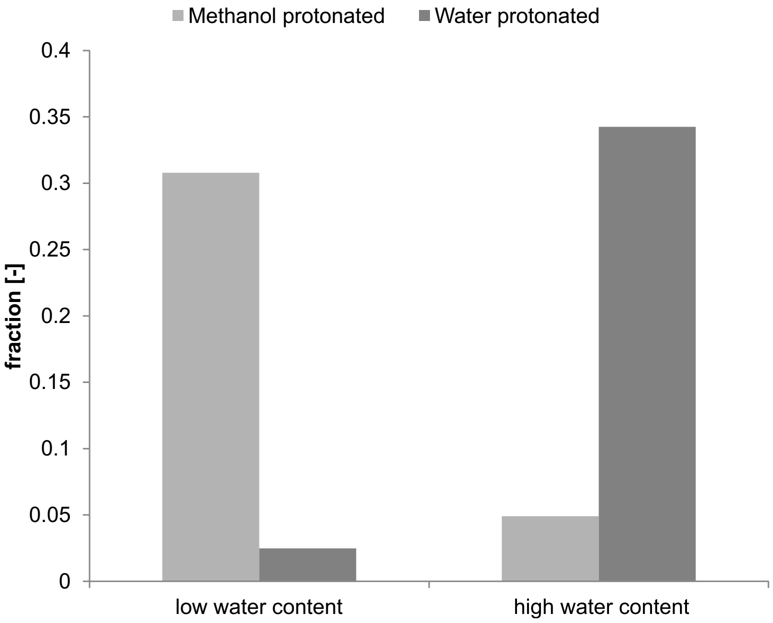

Figure 5.13: Fraction of time in the AIMD simulation of HMB at 623 K and 1 atm for which methanol and water are protonated at low and high water content.

environment, which is in line with the experimental results of the master dissertation by K. Wondergem[100] and the corresponding theoretical results of De Wispelaere et al.[131] These results showed that when water is present in the catalyst, it competes for adsorption on the acid sites, thus forcing methanol to diffuse deeper into the crystal to find an available adsorption site. Whether or not this competitive adsorption has an influence on the reaction barrier for the methylation of HMB will be discussed in Section 6.1.

5.4 Relative stability of the MTO intermediates in the side-chain mechanism

Before examining the reaction barriers it is instructive to inspect the relative stability of the intermediates. This is done by calculating the average potential energy over the production runs of the different intermediates for both the low and high water content case. For both cases, the average potential energy of each intermediate is taken relative to the average potential energy of the corresponding simulation of HMB, resulting in Figure 5.14. In this graph, also the relative enthalpies found by the static calculations of De Wispelaere et al.[64] are depicted.

Analyzing the results on the graph, clearly shows that there is some uncertainty on energy

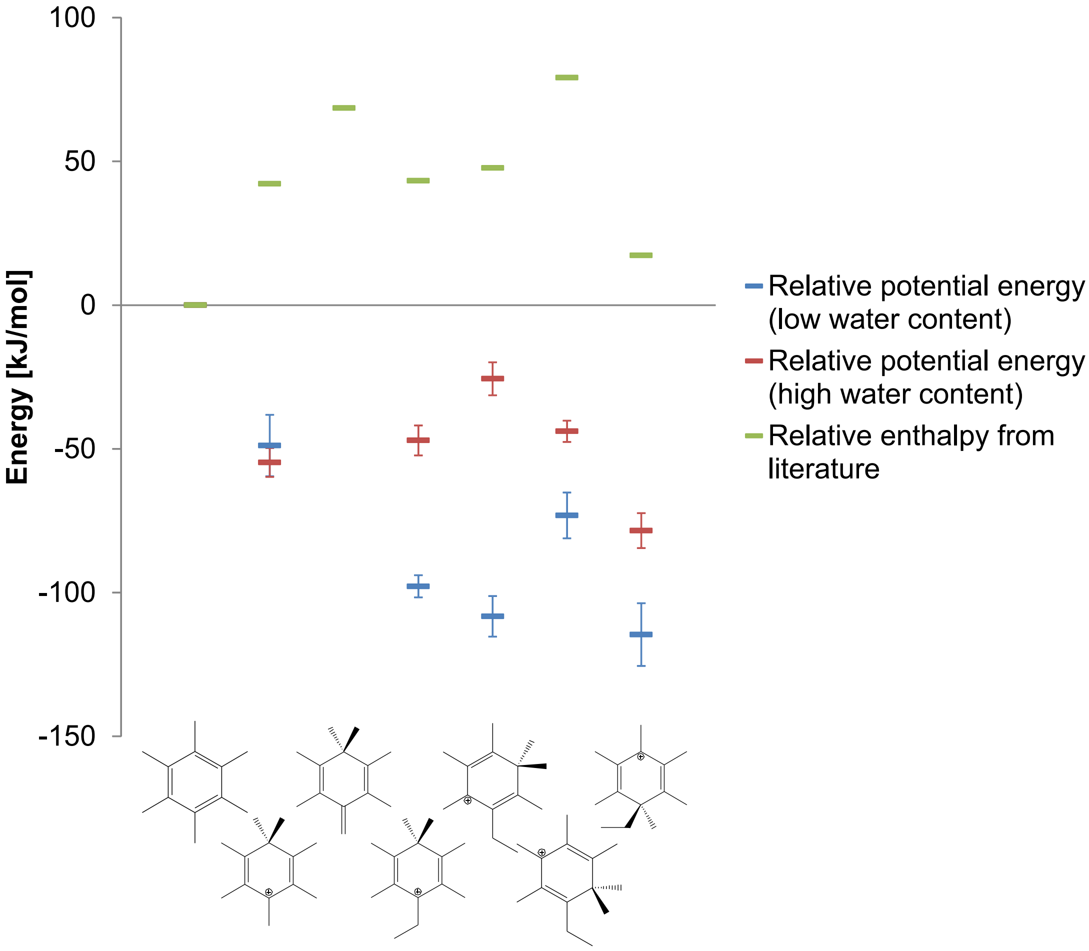

Figure 5.14: Average potential energy of the different intermediates relative to HMB for the low and high water content case combined with the enthalpy from literature.[64] The average potential energies are taken over the 50 ps AIMD simulations at 623 K and 1 atm. The error bars are calculated as explained in Appendix C. The static calculations from literature were executed with the B3LYP functional in an extended cluster with one BAS.[64]

calculations based on ab initio molecular dynamics simulations. The calculation of the error bars is explained in Appendix C. This uncertainty is due to the trade-off between the accuracy of the results and the time needed for the calculations. For the AIMD simulations the threshold error for the self consistent field (SCF) is taken to be 10^{-5} a.u. A lower value would lead to more accurate results, but this would make the required computer time too long. Therefore, the data in Figure 5.14 merely provide a qualitative view on the stability trends. More accurate results of the relative energy will be obtained by the metadynamics simulations in Chapter 6. When comparing the static and dynamic results, three conclusions can be drawn. Firstly, the literature values show that HMMC is indeed unstable and accordingly, no stable AIMD simulation was obtained for this intermediate. Secondly, a difference is found between the stability of neutral an ionic intermediates for the static and dynamic calculations. In the static calculations, the ionic intermediates are found to be less stable than HMB, while the dynamic calculations show the opposite result. Finally, the results for low and high water content can be compared. This shows that addition of water destabilizes the ionic intermediates significantly, except for heptaMB$^+$. Thus, as for the framework deprotonation, a difference is found between heptaMB$^+$ and the other cationic intermediates.

5.5 Conclusion

In this chapter, the influence of water on the stability and mobility of the aromatic intermediates occurring during the MTO process has been evaluated. This was done by considering the influence on the framework flexibility of H-SAPO-34, the behavior of the aromatic intermediates of the side-chain cycle in the catalyst pores, the deprotonation of the framework and the relative stability of the intermediates.

The framework flexibility of H-SAPO-34 was analyzed by looking at the unit cell parameters and volume variations when additional molecules are loaded in the unit cell. The addition of the aromatic intermediate, HMB, to the catalyst environment introduced a volume expansion of 4 % compared to an empty unit cell. A subsequent addition of methanol to the H-SAPO-34 unit cell leads to an extra expansion of 0.2 %. In contrast, the addition of water to the catalyst pores leads to a volume contraction of around 1.2 %. When corresponding changes in the unit cell parameters are considered, the volume variations are found to be anisotropic, since the main variations occur along the c-axis. These asymmetric unit cell changes might be because the more flexible 8-ring windows are directed parallel to the c-axis, while the more rigid 6-ring window are perpendicular on this axis. These conclusions are in line with experimental results.[70]

Subsequently, it was examined whether the contraction due to the extra loading of water influences the behavior of the aromatic intermediates in the H-SAPO-34 environment. All intermediates of the side-chain mechanism were found to rotate during the AIMD simulation to take advantage of the entire length of the zeotype cage. No clear dependence of the tendency for rotation and the behavior of the additional guest molecules on the water loading was found. Additionally, the influence of the acidity and hydrophobicity of the framework on the rotation was considered by repeating the simulations of heptaMB$^+$ in an H-SSZ-13 environment. This analysis led to the conclusion that this rotation seems to be independent of the chemical composition of the catalyst framework.

Since acidity is known to be an important feature of the MTO catalyst[21], the dependence of the deprotonation probability of the H-SAPO-34 framework on the loading of water was analyzed. This study showed that increased water content leads to an increased probability for the framework to deprotonate. Furthermore, the influence of the acidity of the catalyst on the deprotonation was investigated by comparing the results for H-SAPO-34 with those of heptaMB$^+$ in the H-SSZ-13 environment. The outcome of this comparison shows that the increased acidity induces an increase in the framework deprotonation probability. Additionally, the influence of the water loading on the probability to protonate methanol are considered for the simulation of HMB, since methanol needs to be protonated for the methylation reaction.[59] The addition of water to the catalyst pores was found to lead to a decrease of the probability to find protonated methanol.

Lastly, the dependence of the relative stability of the aromatic intermediates on the water content was examined. This analysis showed that the addition of water destabilizes the cationic intermediates, except for heptaMB$^+$. Furthermore, a clear difference was found with the results of the static calculations reported by De Wispelaere et al.[64] In the static calculations the cationic intermediates were found to be unstable compared to HMB, while the dynamic simulations show a stabilization of the ionic intermediates compared to HMB.

Chapter 6

Influence of water on the MTO reaction mechanism

Nowadays, the HP mechanism has been accepted as governing the MTO process. In the reaction cycles proposed for H-SAPO-34, aromatic intermediates, especially polymethylbenzenes, play an important role as HP species, as proven both experimentally and theoretically.[34,35,61] Two types of reaction cycles are distinguished, namely the side-chain mechanism and the paring mechanism, which were discussed in Section 2.2.1.[16,21,36] For the side-chain mechanism, a complete cycle for $C_2^=$, $C_3^=$ and $C_4^=$ formation with low barriers was already found using static calculations.[64] In this chapter, the reaction barriers for this reaction cycle will be recalculated using dynamic simulations at 623 K. The cycle is started from HMB, since it is identified as a crucial HP species[21,68] and it was used as the starting point for the static calculations.[64] Dynamic simulations have the advantage that temperature, entropy and guest molecule effects can be taken into account.[22] Furthermore, the reaction barrier of the first reaction in the paring mechanism will be calculated to have a first idea of the competition between the side-chain and paring mechanism in H-SAPO-34. All simulated reactions are depicted in Figure 6.1.

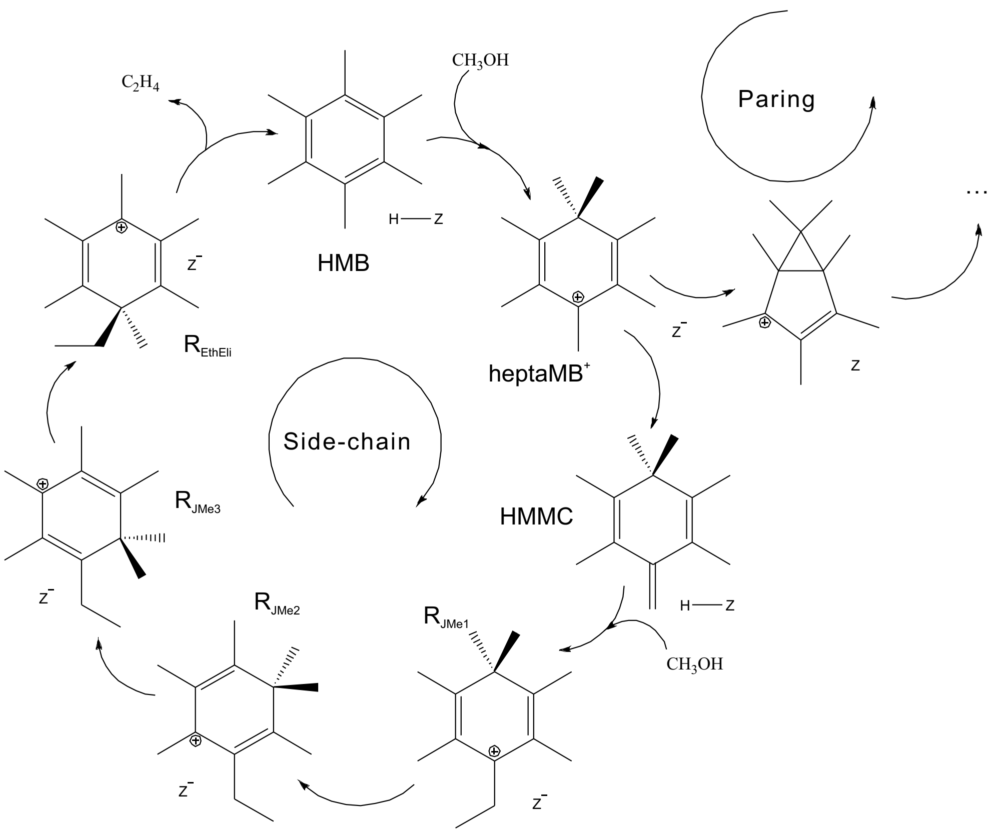

Figure 6.1: Representation of the simulated reactions in the side-chain mechanism and the onset of the paring mechanism.

6.1 Methylation of hexamethylbenzene

The methylation reaction of HMB with methanol forming heptaMB$^+$ is the first step in both the side-chain and paring mechanism as can be seen in Figure 6.1. As explained in Section 2.2.1, methylation reactions are accepted to play an important role in all proposed mechanisms for the MTO process.[21] Good agreement between theoretical and experimental data is already obtained for the methylation of alkenes in H-ZSM-5.[57,58]

This first step is similar to the methylation of benzene as described by Moors et al.[59] Therefore, similar collective variables can be used to simulate the methylation of HMB. The collective variables are represented in Figure 6.2. The first collective variable, CV1, is a coordination number between the carbon and oxygen of the reacting methanol. The breaking of this C-O bond leads to the formation of water that can diffuse away from the methyl group. This diffusion is limited by the introduction of a wall on the CV, which enhances the probability of a transition state recrossing. The second collective variable describes the formation of the bond between the methyl group and the aromatic ring. Therefore, CV2 is described by a CN between the carbon of the methyl group and the six carbon atoms in the aromatic ring of HMB. Similar to CV1 a wall is introduced to keep the distance between the methyl carbon and the benzene molecule under control. To ensure that the reacting methanol is protonated during the entire reaction, as was suggested in literature[59], two extra walls were introduced on coordination numbers between the oxygen of methanol and the hydrogens to keep the methanol protonated. More detailed information on the collective variables and the walls can be found in Appendix D.

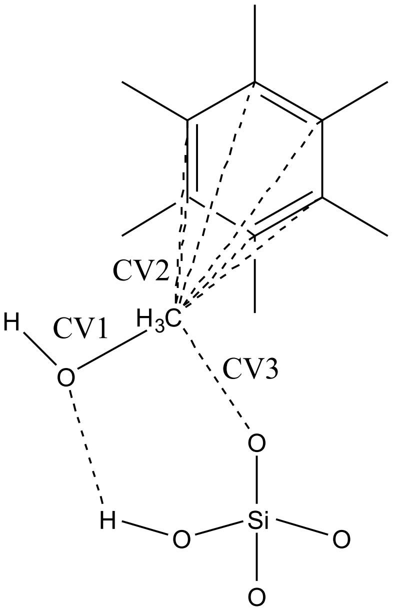

Figure 6.2: Representation of the collective variables used to simulate the methylation of HMB. The acid site is simplified to the Si atom and the four surrounding oxygens.

Since metadynamics simulations are executed in the NVT ensemble, the volume and thus the unit cell dimensions are kept constant. For these constant values, averages are taken from the 50 ps production runs of the AIMD simulations at 623 K and 1 atm. The values used in the methylation of HMB are represented in Table D.2.

During the first attempt to simulate the methylation of HMB with the two collective variables described above, the formation of a methoxide species occurred in the simulation at low water content. This reaction leads to a third stable state in the 2D FES obtained from the MTD simulation, as can be seen around the origin in Figure 6.3. When the 2D surface is projected onto a 1D surface to obtain the 1D free energy profile from which a barrier can be calculated as described in Section 4.5, this third stable state will overlap with the transition state between the other two stable states. Furthermore, since the C-O bond of the methoxide is not described by the used collective variables, there is no driving force for the system to leave this minimum. This means that the simulations stay in this state and thus had to be restarted with an extra CV to be able to take the methoxide species into account. Therefore, CV3 was added which is a CN between the carbon of the methyl group and the Si neighboring oxygens as represented in Figure 6.2.

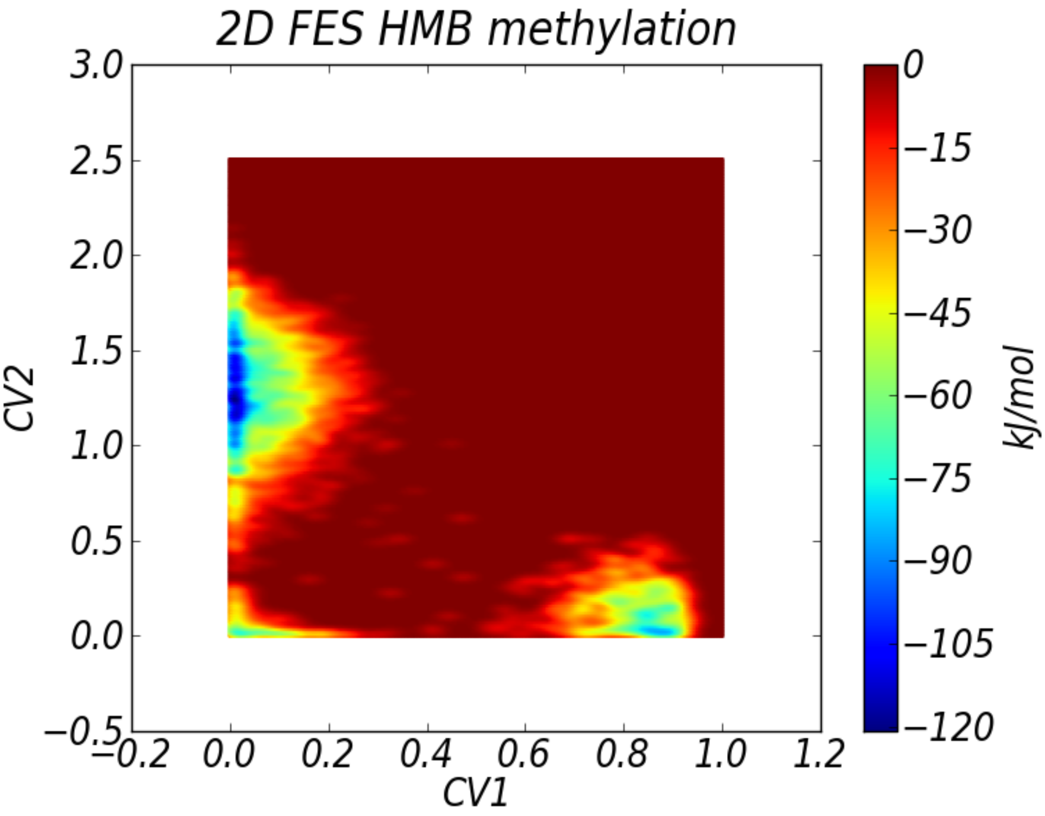

Figure 6.3: The 2D FES obtained from the metadynamics simulation of the methylation of HMB at 623 K in the low water content case using two collective variables, showing the third stable state obtained around CV1 = CV2 = 0.

Although the simulations with two collective variables at low water content eventually led to the formation of methoxide species and thus had to be stopped, the reaction barrier for the methylation of HMB with methanol was first recrossed at least once, as can be seen in Appendix E. Therefore, a first estimate of the reaction barrier can be obtained from the MTD simulation results up to the formation of methoxide and compared with the results of the simulations with other water content and the results of the simulations with three collective variables. The MTD simulation with no and high water content results in a 2D FES as plotted in Figure 6.4.

At first sight, both 2D free energy surfaces look similar, with two minima representing the reactant and product state. Although, when analyzing the transitions between these two minima, a difference can be observed. On the one hand, the simulations with no water loading only show one type of transition path, which goes straight from

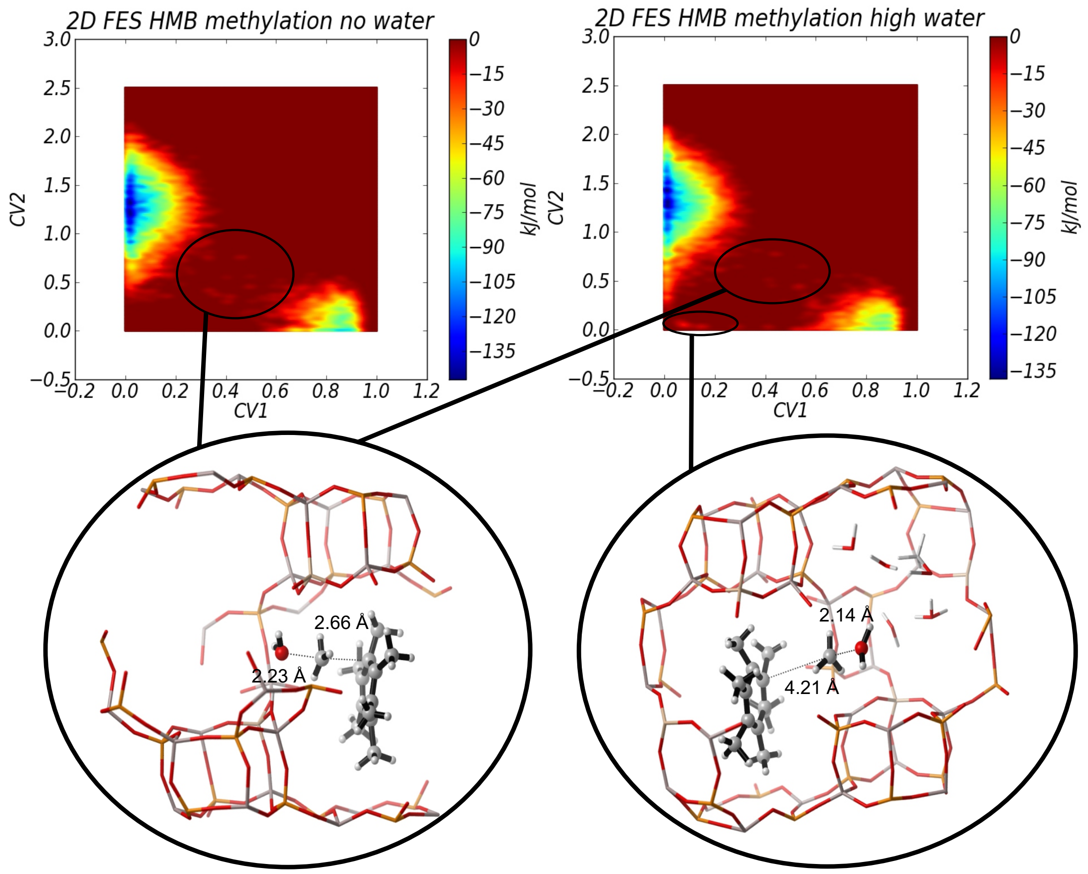

Figure 6.4: The 2D FES obtained from the metadynamics simulation of the methylation of HMB at 623 K with no (left) and high (right) water content case using two collective variables. At high water content two transition states are found, while the simulations with no water loading shows only one type of transition state.

one minimum to the other and is represented in the left snapshot of Figure 6.4. On the other hand, a second type of transition state is found in the simulation at high water content. This second configuration for the transition state, depicted in the right snapshot in Figure 6.4, is only encountered once. It was found when the water molecule formed from methanol diffused away from the aromatic. Subsequently, a methyl group was formed, which first diffused to the water molecule and then formed methanol. All other transitions occurred via the left transition state. From these observations, the advantage of dynamic simulations compared to static calculations becomes clear. In dynamic simulations, not one single reactant and product state is taken into account, but the entire reactant and product valleys are sampled. Furthermore, not one single transition state is considered, but different reaction paths are sampled. As explained in Section 4.5, the 2D free energy surface can be projected onto a 1D surface, leading to the 1D free energy profiles depicted in Figure 6.5. The reaction coordinate resulting from the procedure described in Section 4.5 is equal to CV2-CV1, which means that the reactants are on the left hand side of the free energy profile and the products are on the right hand side.

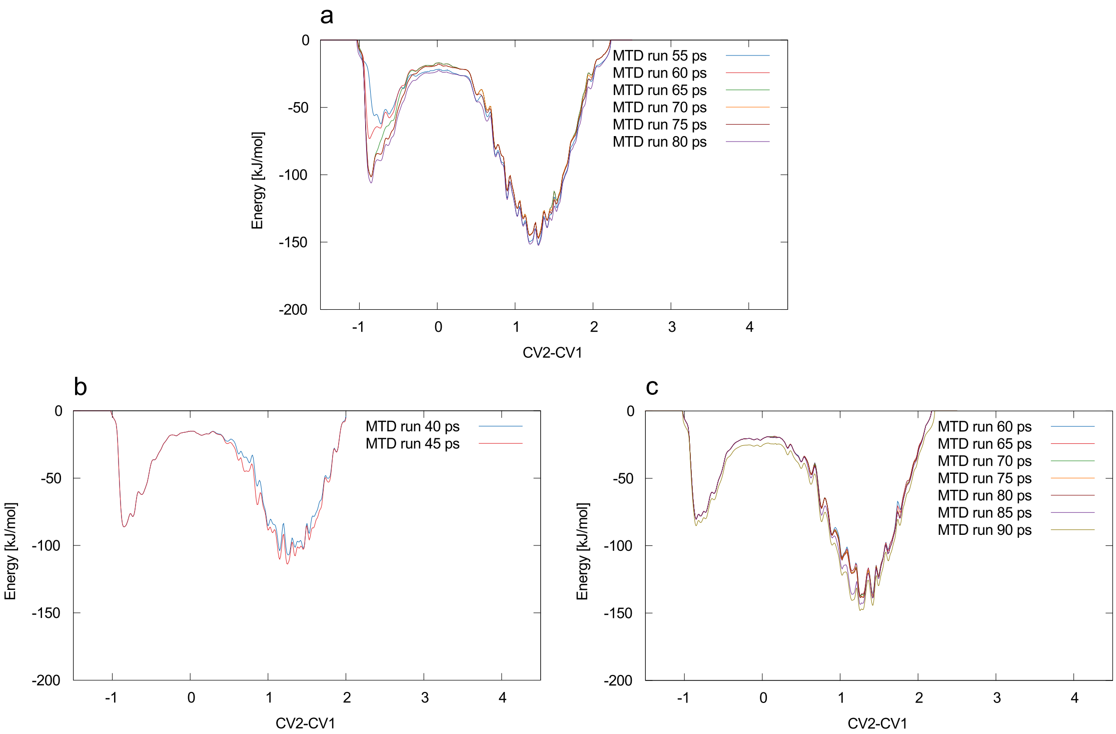

Figure 6.5: The 1D free energy profiles obtained from the projection of the 2D free energy surfaces resulting from metadynamics simulation of the methylation of HMB at 623 K in the no (a), low (b) and high (c) water content case.

When looking at the resulting free energy profiles, it becomes clear that the simulations have not yet completely converged. Nevertheless, the results give a first idea of the reaction barriers. Furthermore, the relative stability of HMB and heptaMB$^+$ can be compared based on these results. In all cases, the heptaMB$^+$ is more stable than HMB, which corresponds well with the results from the average potential energy calculations described in Section 5.4. Based on these free energy profiles, the reaction barrier for the methylation of HMB can be calculated. The resulting forward ($\Delta\overrightarrow{G}^{\ddagger}$) and backward ($\Delta\overleftarrow{G}^{\ddagger}$) barriers are given in Table 6.1.

These results show that an increase in the amount of water present in the catalyst environment leads to a decrease of the barrier for the forward methylation reaction. Furthermore, when comparing these results with the free energy barrier from the static calculations in literature[64], where a barrier of 57.2 kJ/mol was found, the barriers obtained via the dynamic calculations are significantly higher. This again demonstrates that dynamic and static calculations might lead to different conclusions on governing

Table 6.1: Reaction barriers for the methylation of HMB.

	$\Delta \overrightarrow{G}^\ddagger$ [kJ/mol]	$\Delta \overleftarrow{G}^\ddagger$ [kJ/mol]
no water content	91	158
low water content	82	109
high water content	72	135

reaction mechanisms and intermediates. When looking at the backward barrier, the results are less logical, which might be because the low water content case has not been sampled sufficiently. There is no clear trend in these results, which show that no water stabilizes heptaMB$^+$ best, while a low water content leads to the worst stabilization.

A possible explanation for the decreasing forward barrier with increased water loading might be a decreased stability of the reacting methanol, which was kept protonated by the introduction of a wall. This protonated methanol can be seen as a pre-reactive complex, as represented in Figure 6.6, which has a free energy which is ΔG_{pre} higher than the stable reactant state. From the analysis of the framework deprotonation, discussed in Section 5.3, it was concluded that increased water content leads to a decrease of the probability to protonate methanol. The protonated methanol thus becomes a less stable complex at higher water loadings, which then leads to an increase of ΔG_{pre}, which in turn might lead to an decrease of ΔG_{rea}, the forward free energy barrier calculated from the MTD simulations. The calculated forward free energy barrier is thus a lower limit for the actual barrier and might be influenced by the barrier for the formation of the protonated methanol.

The destabilization of protonated methanol with increasing water loading is confirmed by the snapshots of the MTD simulations at 623 K shown in Figure 6.7. In these snapshots the protonated methanol is shown for no (a), low (b) and high (c) water content. At no and low water content, the protonated methanol can be adsorbed at the BAS, which stabilize the complex. In contrast, at high water content the BAS is not available due to the competitive adsorption of water, which is shown in the background of snapshot c, leading to a rather unstable protonated methanol. The instability of the protonated methanol is shown through the interaction of the protons with the framework and the aromatic ring.

To get insight in the importance of the methoxide species in the methylation reaction, the results of the simulations with three collective variables are analyzed. These simulations lead to an energy surface in three dimensions, which cannot be easily represented and is more difficult to interpret. In this case, the extra dimension cannot be eliminated via a projection on a 1D surface as before, since the third stable state will overlap

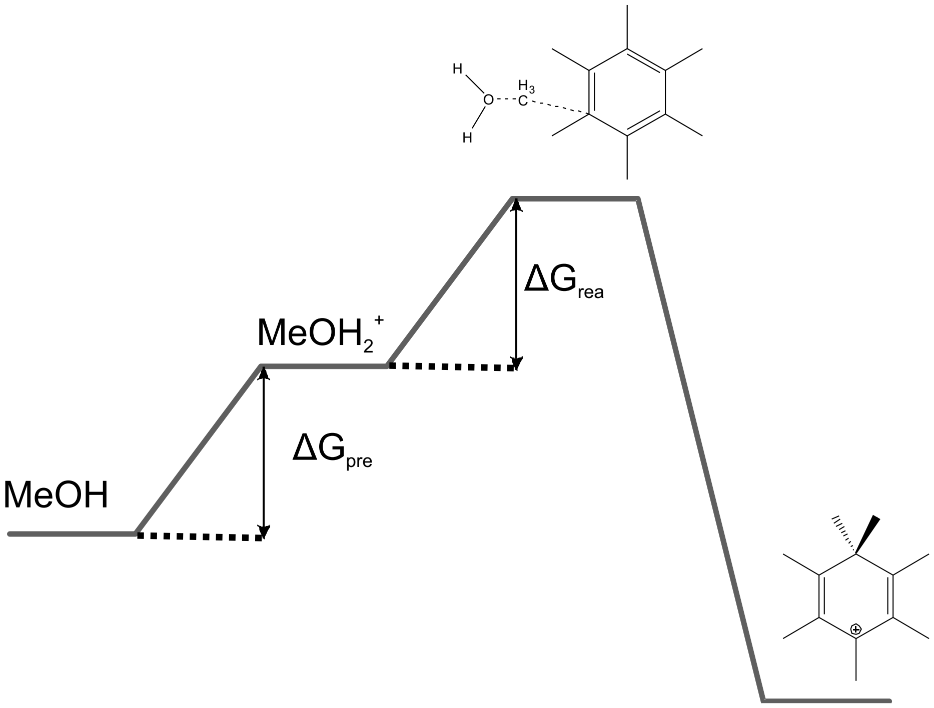

Figure 6.6: Representation of the barrier for the formation of the protonated methanol as pre-reactive complex.

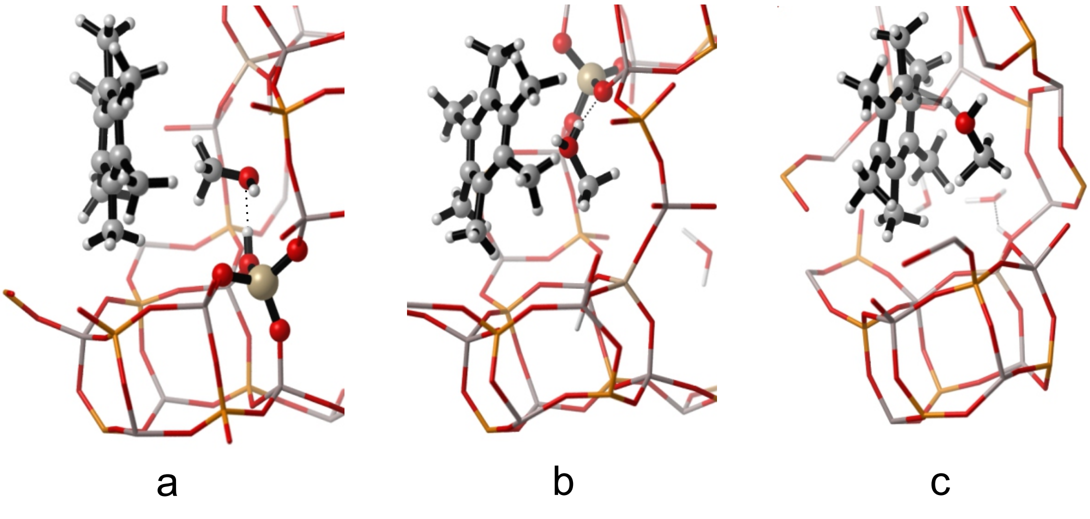

Figure 6.7: Snapshots of the MTD simulations at 623 K of the protonated methanol as pre-reactive complex in no (a), low (b) and high (c) water content case.

with the transition state between the other two states. Therefore, an different method is used which localizes the lowest free energy path that connects the stable reactant and product state, called the LFEP method proposed by Ensing and co-workers[125] explained in Section 4.5.

Due to the third collective variable, the metadynamics simulations go slower than the two dimensional calculations, since the efficiency of the MTD method scales exponentially with the number of collective variables.[132] Therefore, the three stable states, namely A, B and C as illustrated in Figure 6.8, were only sampled in the case no water was added to the zeotype environment. In the low and high water cases, methoxide formation is not yet encountered and a longer simulation time is needed.

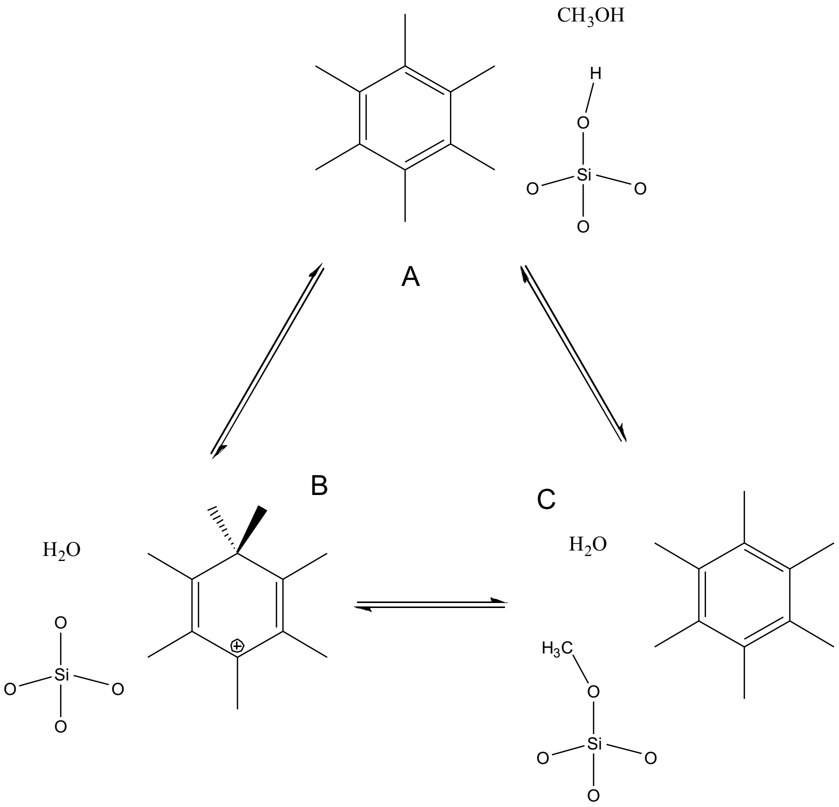

Figure 6.8: Representation of the three stable states encountered in the three dimensional metadynamics simulation of the methylation of HMB at 623 K.

Via the LFEP method, a 1D free energy profile of the three reactions in Figure 6.8 can be obtained. These are depicted in Figure 6.9 for the case with no water.

The first energy profile (a) represents the concerted methylation of HMB with a methanol molecule, which was also sampled by the simulation using two collective variables. The forward free energy barrier (from A to B), which is found to be 14 kJ/mol, is clearly smaller than the value given in Table 6.1 that was computed from the 2D simulation results. This might be because state A has only been encountered once during the simulation, since recrossing to methanol was not sampled yet. This is similar to the two dimensional case as can be seen in Figure 6.5a in which the forward barrier also increases after the first recrossing. Longer simulations might thus give better correspondence with the earlier results. Just as for the simulations using two collective variables, the backward

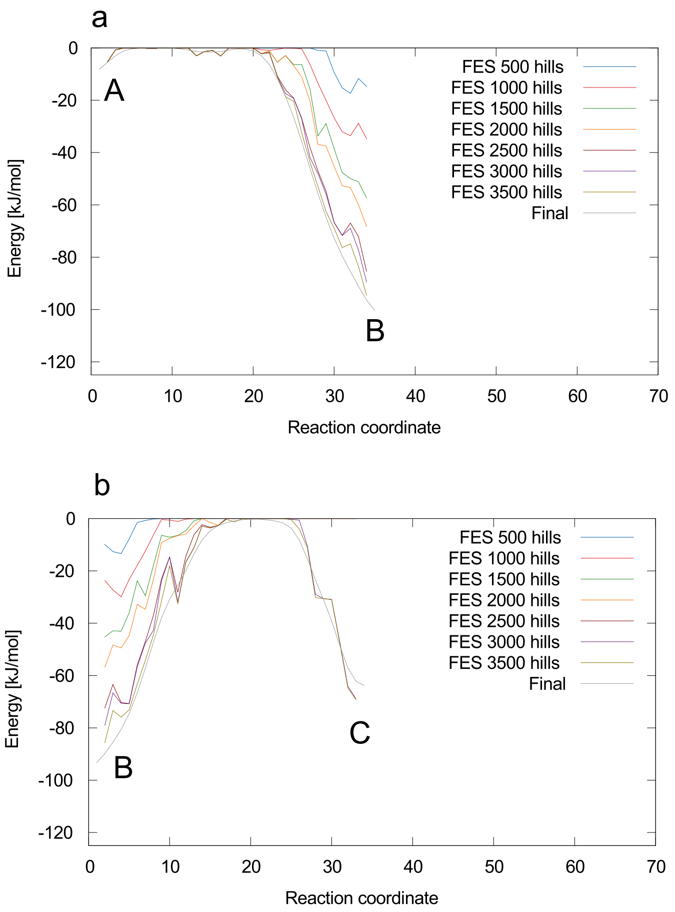

Figure 6.9: The 1D free energy profiles obtained via the LFEP method of the 3D free energy surfaces resulting from metadynamics simulation of the methylation of HMB at 623 K in case no water is originally present in the catalyst environment. The three different graphs (a) and (b) depict the free energy profile between state A and B and B and C, respectively. The three states were defined in Figure 6.8. The different line colors represent the convergence of the energy profile in function of the simulation time, since one hill is added every 25 fs.

reaction barrier, equal to 103 kJ/mol, is significantly higher than the forward free energy barrier, again showing that heptaMB$^+$ is the more stable state. Nevertheless, the free energy barrier is still a lot lower than the 2D simulation result given in Table 6.1.

The subsequent reaction profile (b) shows the demethylation of heptaMB$^+$ with the formation of a methoxide species, which corresponds to the reverse of the second step in the stepwise methylation mechanism as was explained in Section 2.2.1. This reaction has been sampled more than the first one. The height of the methylation barrier (C to B), which is found to be 67 kJ/mol, is similar although slightly lower than the results in Table 6.1, suggesting that methylation via a methoxide species is similar to methylation with methanol as was also suggested by Van der Mynsbrugge et al.[80]

A crossing of the third barrier (A to C) was not yet encountered, so no free energy barrier for this reaction is available yet. Longer simulations might give more insight in the formation of methoxide species and the other two reactions.

Since the formation of a methoxide species is not yet encountered in the 3D simulation of the low and high water case, it is only interesting to look at the barrier of the reaction of A to B in these cases. These represent the methylation of HMB with methanol as in the 2D case. The resulting free energy profiles are depicted in Figure 6.10. In the low water content case (a), the barrier has been recrossed once, which results in a good sampling of state A and thus a good estimate for the forward barrier, which equals 88 kJ/mol, compared to the 2D simulations results given in Table 6.1. Nevertheless, the backward barrier, which is found to be 70 kJ/mol, is rather small compared to the barrier in Table 6.1. Furthermore, the relative stability of both states is altered, since state A would be the most stable state according to the 3D simulations. In contrast, in the high water content case (b), the barrier has only been crossed in the forward direction and remained in state B for the remainder of the simulation so far. This results in an underestimation of the forward barrier, which is found to be 32 kJ/mol, compared to the 2D results, while the backward barrier of 144 kJ/mol is in correspondence with the earlier results. Once again, longer simulation times might lead to better convergence of the results and to information on the role of methoxide species in the methylation reaction.

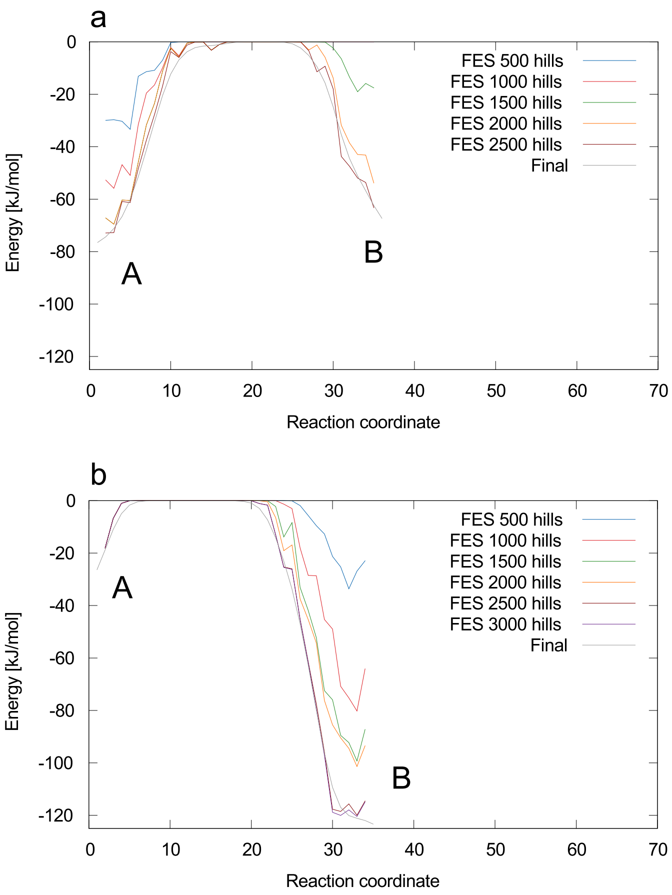

Figure 6.10: The 1D free energy profiles obtained via the LFEP method of the 3D free energy surfaces resulting from metadynamics simulation of the methylation of HMB with methanol (reaction A to B in Figure 6.8) at 623 K in the low (a) and high (b) water content case. The different line colors represent the convergence of the energy profile in function of the simulation time, since one hill is added every 25 fs.

6.2 Deprotonation versus ring contraction of heptaMB$^+$

In the second step of the HP mechanisms, the side-chain and paring mechanism split up as can be seen in Figure 6.1. While heptaMB$^+$ deprotonates to HMMC in the side-chain mechanism, a ring contraction of heptaMB$^+$ occurs in the onset of the paring mechanism. In this section, both reactions are discussed to get insight in the competition between both mechanisms and to see whether water has an influence on this competition.

6.2.1 Simulation of the deprotonation of heptaMB$^+$

The second step of the side-chain mechanism is the deprotonation of heptaMB$^+$, leading to the formation of HMMC. Since HMMC is found to be an unstable intermediate in the AIMD simulations at 623 K and 1 atm, this reaction is expected to be difficult to simulate, with possibly a high reaction barrier. The two collective variables that were used to describe this reaction are depicted in Figure 6.11. The first collective variable is a coordination number between the carbon of the deprotonating methyl group and the three hydrogens which can be transfered. The second collective variable is a CN between the three transferring hydrogens and the closest oxygens which can receive a proton (in both low and high water case, this was found to be the oxygen of a water molecule). On CV2 a wall was set to keep the oxygen in the neighborhood of the deprotonating methyl group, to avoid a proton jump to other oxygens, not taken into account by the collective variable. In the first attempts of the simulation of this reaction, it was indeed seen that HMMC is an unstable intermediate and the backward reaction occurred very quickly. Because the backward reaction occurred with one of the hydrogen atoms of the water molecule, which is not described by the original collective variables, the simulations were restarted and two walls were added to avoid breaking of the O-H bond. The computational details are again given in Appendix D.

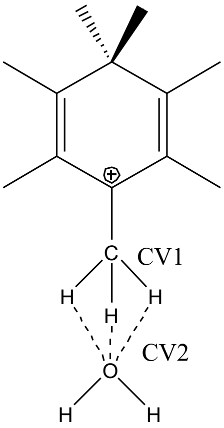

Figure 6.11: Representation of the collective variables used to simulate the deprotonation of heptaMB$^+$.

As explained in Section 4.5, Gaussian hills are added during the metadynamics simulations which disturbs the local equilibrium. In the deprotonation of heptaMB$^+$, a proton is transfered. Since a proton has a low mass and thus inertia, it is very sensitive to the changes on the free energy surface due to the Gaussian hills. This might lead to high accelerations of the proton and thus breaking of the system. Because the goal of the simulations is to find equilibrium thermodynamic properties of the reaction, the atomic masses become irrelevant in the Hamiltonian. Changes in the masses will only have an influence on the dynamic behavior of the simulation, but not on the thermodynamic properties.[103,133] Therefore, the high accelerations are avoided by artificially increasing the mass of hydrogen to 3.0 a.u., which corresponds to the tritium isotope.

Because the metadynamics simulations are again executed in the NVT ensemble, the volume and thus the unit cell dimensions are kept constant. The values used in the MTD simulation of the deprotonation of heptaMB$^+$ are represented in Table D.4.

Because of the instability of the HMMC intermediate, it is expected that recrossing of the barrier will occur quickly after the forward crossing of the barrier. This is indeed seen in the graphs plotting the used collective variables as a function of time depicted in Figure 6.12. The quick crossing and recrossings can be seen at the points where CV1 decreases while CV2 increases. Examples can be seen around 5 and 8 ps for the low water content case (Figure 6.12a) and around 6 and 9.5 ps for the high water content case (Figure 6.12b). For both simulations it can be seen that the collective variables remain in the product state after 10 ps simulation time. The reason for this event is for both cases different. In the low water content case, the collective variables stay in the reactant state, while the backward reaction takes places with one of the two other hydrogens of the formed H_3O^+. This means that the two extra walls, which were introduced to avoid this, were not defined strict enough. In the high water case on the other hand, this reaction does not occur. Instead, the formed H_3O^+ is found to diffuse away from the formed HMMC, which remains stable. This difference might be because of the instability of H_3O^+ only stabilized by a methanol molecule in the low water content case compared to the formation of a cluster in the high water content case, which can be seen in Figure 6.13. Nevertheless, both events result in the fact that only the simulation results up to 10 ps are useful to get an idea of the reaction barrier in both cases.

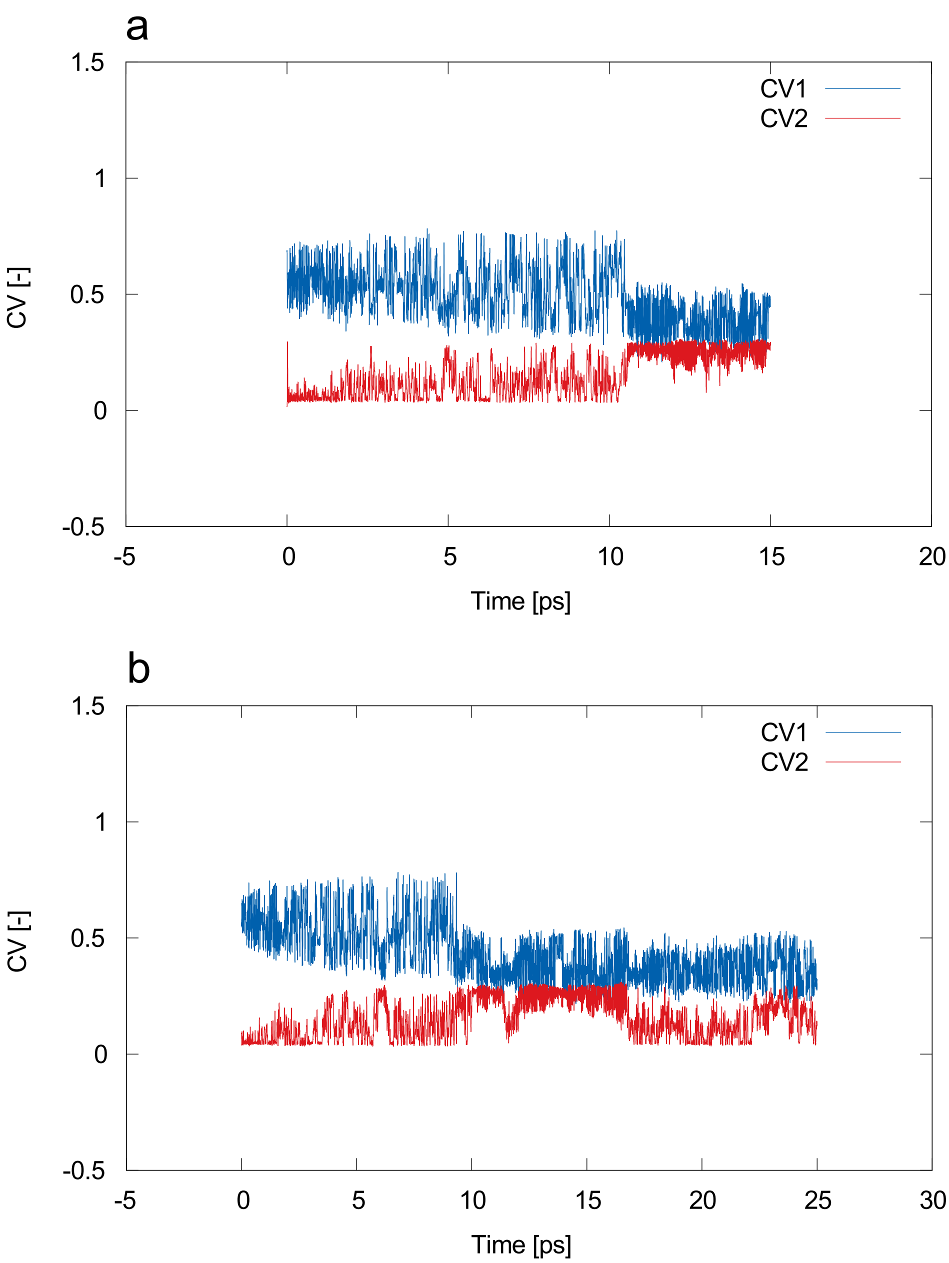

Figure 6.12: The collective variables used for the MTD simulation at 623 K of the deprotonation of heptaMB$^+$, which were defined in Figure 6.11, with low (a) and high (b) water content, in function of simulation time.

Due to the use of two collective variables, a two dimensional FES is obtained similar to that of the methylation of HMB depicted in Figure 6.4. Therefore, the 1D free energy profile can again be obtained via projection as explained in Section 4.5, leading to the profiles depicted in Figure 6.14. When looking at these free energy profiles at 10 ps, the forward barrier is similar to the barriers encountered previously, while the backward

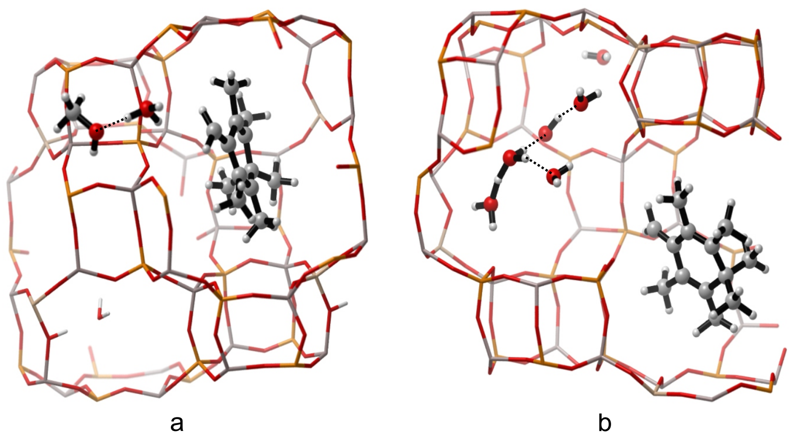

Figure 6.13: Snapshot of the MTD simulation of the deprotonation of heptaMB$^+$ at 623 at low (a) and high (b) water content, showing the behavior of the formed H_3O^+.

barrier is very low to non-existing. Therefore, only the forward barriers are calculated with a transition state taken around CV2-CV1 = 0.27, resulting in Table 6.2. These barriers are slightly higher than the barrier found by the static calculation, which was 70.9 kJ/mol. Furthermore, when analyzing the influence of the amount of water present on the reaction barrier, a decrease of the deprotonation barrier is found, which might be due to the stabilization of H_3O^+ by the additional water present.

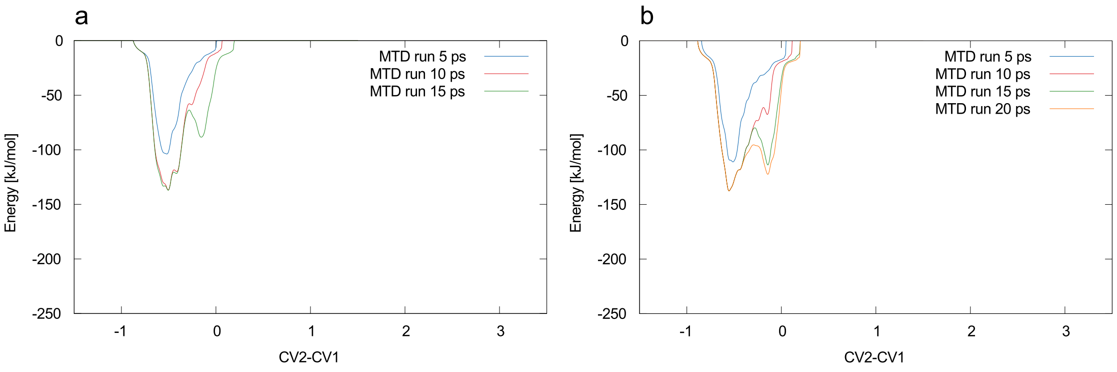

Figure 6.14: The 1D free energy profile of the deprotonation of heptaMB$^+$ in low (a) and high (b) water content case at 623 K.

Table 6.2: Reaction barriers for the deprotonation of heptaMB$^+$.

	$\Delta \overrightarrow{G}^{\ddagger}$ [kJ/mol]
low water content	91
high water content	77

6.2.2 Simulation of the ring contraction of heptaMB$^+$

As mentioned above, the first step of the paring mechanism is a ring contraction. Earlier work suggested that this is a two-step reaction with an intermediate product as depicted in Figure 6.15.[103] Therefore, two parallel simulations were executed. On the one hand, a two dimensional simulation is executed to check whether the reaction is really a two-step reaction. This 2D simulation is necessary to be able to distinguish between the two product states. On the other hand, a second simulation with only one collective variable was executed, which simulates the transition from the reactant to the intermediate product to be able to determine the reaction barrier. Only one CV is used in this second simulation, since the efficiency of the MTD method scales exponentially with the number of collective variables.[132] Thus faster crossing and recrossing is expected in the 1D simulation, leading to more detailed information on the free energy barrier.

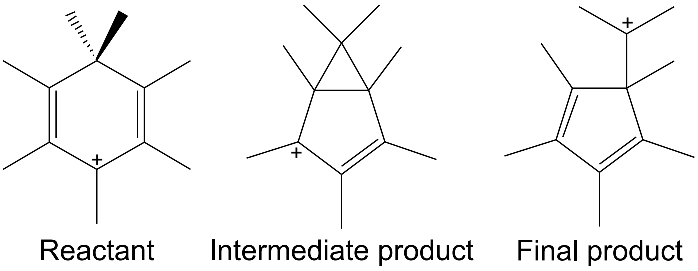

Figure 6.15: Representation of the reactant and product states in the ring contraction reaction of heptaMB$^+$.

For the first simulation the two collective variables depicted in Figure 6.16 are used. CV1 is a coordination number between C6 and C2 in order to introduce the formation of a bond between these two atoms. The second collective variable is a CN between C1 on the one hand and C2 and C6 on the other hand. This CV should break the C1-C2 or C1-C6 bond to initiate the transition from the intermediate product to the final product.

For the second simulation only one collective variable is used, namely CV1 from Figure 6.16. Furthermore, a wall is added to the second collective variable, in order to avoid the C1-C2 and C1-C6 bond from breaking, such that only the intermediate product is sampled.

Earlier simulations showed that the formed 3-ring or iso-propyl group is very mobile and can perform a 'ring walk' on the five ring.[103,134] This 'ring walk' is prevented by hindering the formation of a bond between C1 and C3, C4 or C5 by using a wall for both the 1D and 2D simulation. More computational details can be found in Appendix D. The constant unit cell parameters are the same as for the deprotonation of heptaMB$^+$ given in Table D.4, since the reactant state is the same for both simulations.

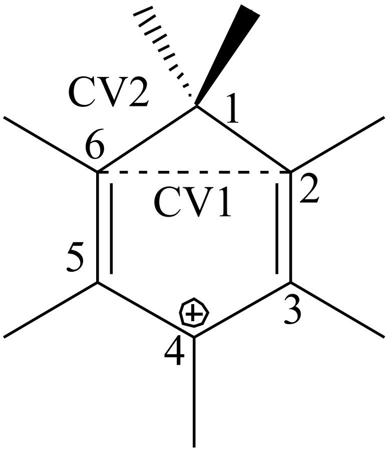

Figure 6.16: Representation of the collective variables used to simulate the ring contraction of heptaMB$^+$.

The two dimensional FES obtained from the MTD simulation with two collective variables at high water content is depicted in Figure 6.17. When analyzing these results, it should be taken into account that the reaction barrier between the reactants and (intermediate) product has only been crossed once as can be seen from the collective variables in function of time in Figure 6.18. Nevertheless, the transition between the intermediate product (CV1 $\approx$ 1.0 and CV2 $\approx$ 1.5) and the final product (CV1 $\approx$ 1.0 and CV2 $\approx$ 1.0) has occurred frequently. From the 2D surface obtained so far, it seems that the barrier between the intermediate product and final product is very low or even non existing compared to the barrier of the first step, which is in accordance with the occurrence of the spontaneous 'ring walk' as described earlier.[134] To assess whether the reaction always occurs via the intermediate product, longer metadynamics simulations are necessary, but so far it can be concluded that the first step of the reaction will be rate determining.

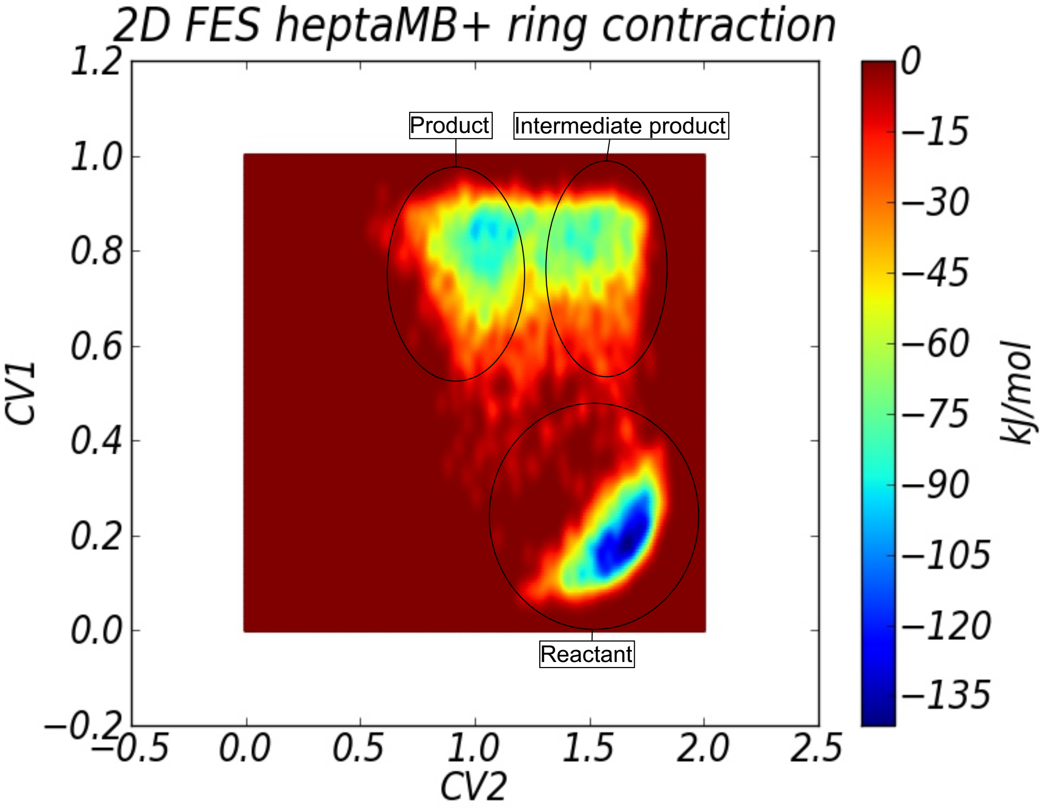

Figure 6.17: The 2D FES obtained from the metadynamics simulation of the ring contraction of heptaMB$^+$ in the high water content case at 623 K.

To estimate the reaction barrier of the first step, the results of the simulations with only one CV can be used. The resulting free energy profiles are depicted in Figure 6.19. These graphs show that the free energy profile has not completely converged yet, since the profile still changes a lot after the recrossing around 25 ps, leading to a significant decrease in the reaction barrier. Furthermore, the stability of the product states relative to the reactant state improves and the relative stability even shifts. This might be because after the second crossing of the free energy barrier, the onset of the second reaction (breaking of the C1-C2 or C1-C6 bond) in the proposed two-step mechanism was sampled more. This means that the extra stabilization might be due to an overlap with the final product. Furthermore, Figure 6.17 shows that the final product is broader in the CV1 direction, which might lead to an overlap with the transition state of the first reaction step, thus lowering this barrier. Therefore, it might be interesting to repeat the simulations with a more stringent wall on the second collective variable, to see whether this explanation clarifies the results at longer simulation times.

Because there is some doubt upon the correctness of the results, the free energy barriers based on the one dimensional simulations are not discussed in more detail. However,

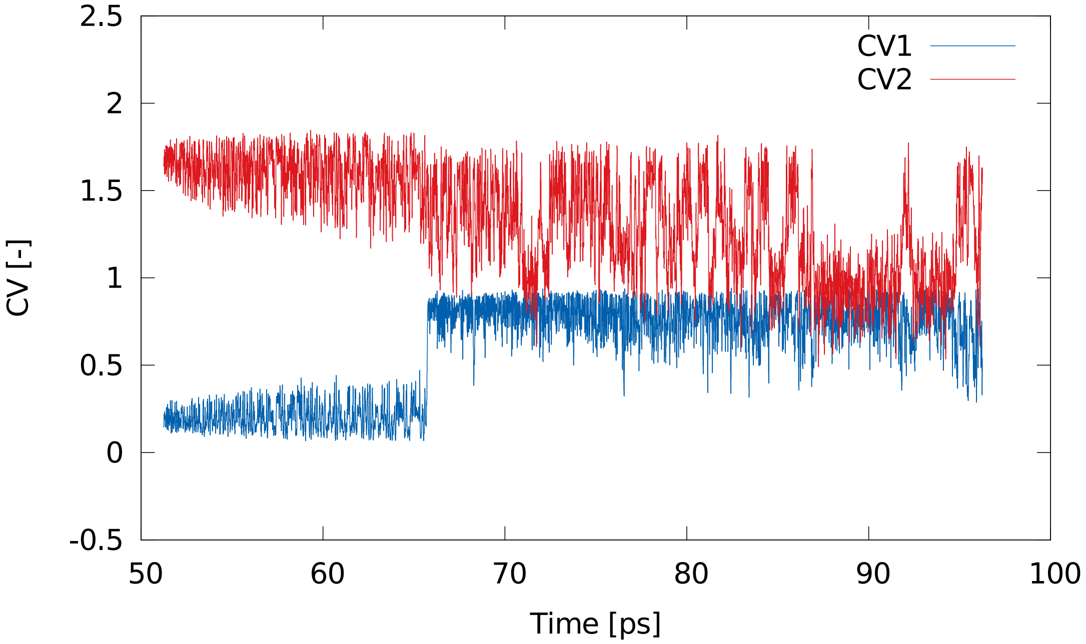

Figure 6.18: The collective variables used for the ring contraction of heptaMB$^+$, which were defined in Figure 6.16, with high water content in function of the metadynamics simulation time.

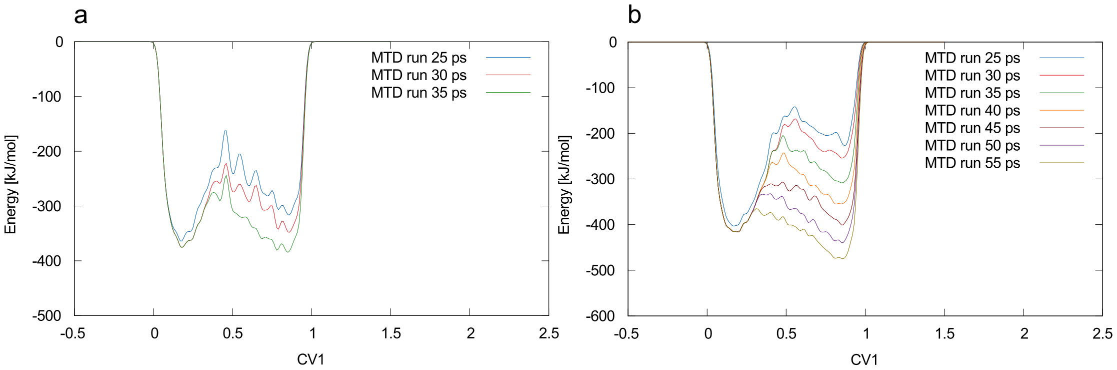

Figure 6.19: The 1D free energy profile of the ring contraction of heptaMB$^+$ in low (a) and high (b) water content case.

an estimate of the forward free energy barrier can be obtained for the 2D simulations using the LFEP method proposed by Ensing and co-workers[125] discussed in Section 4.5. Only the high water content simulation is considered, since the low water content 2D simulation had failed. The resulting lowest free energy path and free energy profile are depicted in Figure 6.20.

The resulting forward reaction barrier is equal to 124 kJ/mol, which is similar to the barrier of 139 kJ/mol obtained by Arstad et al.[134] in H-Beta. This barrier can be com-

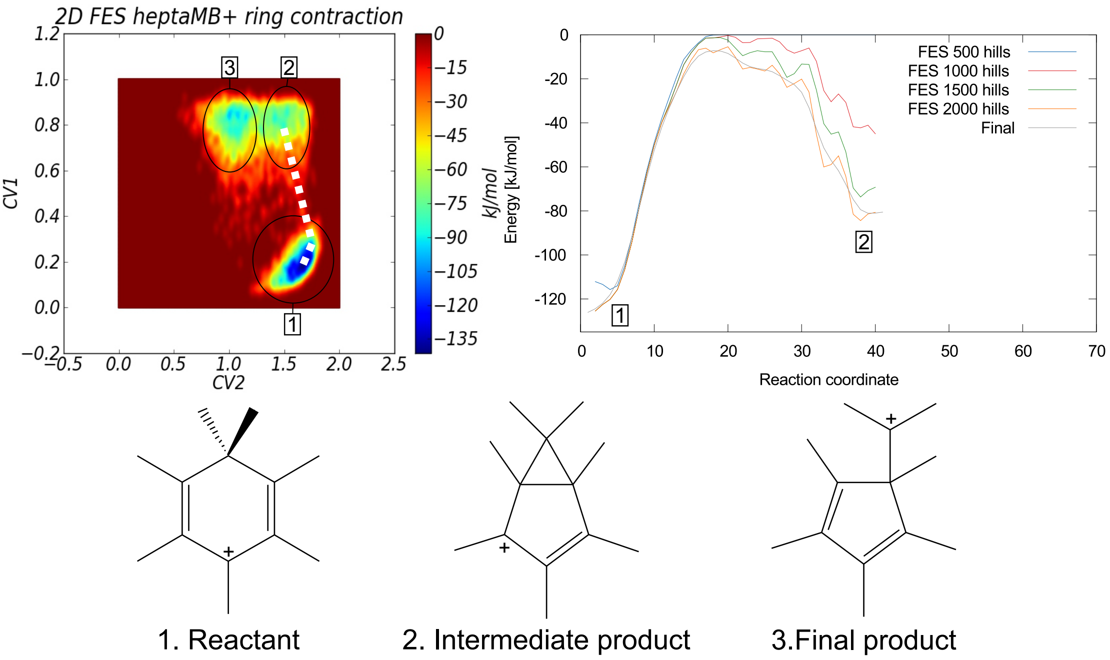

Figure 6.20: The 2D free energy surface (left) from the MTD simulations of the ring contraction of heptaMB$^+$ at 623 K and 1 atm in high water content case, showing the transition path found via the LFEP method[125] resulting in the 1D free energy surface (right). In the lower part, the three intermediates encounter during the ring contraction are depicted.

pared to the barrier for heptaMB$^+$ deprotonation at high water content, which showed a barrier of 77 kJ/mol. This suggests that in H-SAPO-34 the side-chain mechanism prevails, though a simulation of the complete paring mechanism would provide more certainty on this competition.

6.3 Methylation of HMMC

After analyzing the influence of water on the competition between the side-chain mechanism and the paring mechanism, the remainder of this chapter focuses on the subsequent reactions of the side-chain mechanism. The next step, the methylation of HMMC is similar to the methylation of HMB, hence similar collective variables are used. The problem with this simulation is that no AIMD production run of HMMC could be obtained as discussed in Section 5.3. Therefore, the metadynamics simulation was started from the product state, the R_{JMe1} intermediate. This intermediate with the used collective variables is shown in Figure 6.21. The formation of methoxides is again taken into account as for the methylation of HMB in Section 6.1. This time the use of three collective variables was avoided by executing two parallel simulations, one sampling the formation of methanol and one the formation of methoxide, corresponding with the inverse reaction of the concerted methylation and the inverse second step of the stepwise methylation, respectively. The formation of methoxide from methanol, which is the first step of the stepwise mechanism, was thus in this case not simulated, since this barrier is expected to be similar to the one that would be obtained in the 3D simulation of the methylation of HMB, discussed in Section 6.1.

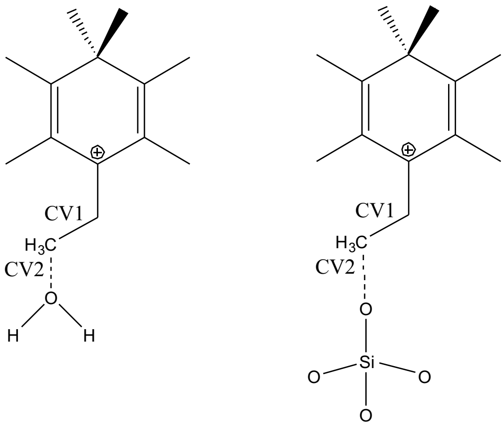

Figure 6.21: Representation of the collective variables used to simulate the methylation of HMMC.

The first collective variable when the formation of methanol is considered is a coordination number between the two carbon atoms of the breaking bond. CV2 is a CN between the carbon of the jumping methyl group and the oxygens of all water molecules. Water is kept close to the jumping methyl group by the application of a wall on the second collective variable.

When the formation of methoxide is simulated, the first collective variable is the same as for methanol formation. The second collective variable is also similar, but the oxygens of water were replaced by the oxygens surrounding the Si defect. Since the simulations were started from the R_{JMe1} intermediate, the same unit cell dimensions as for the first methyl jump are used in the metadynamics simulations, which are represented in Table 6.24. A summary of the computational details used in the simulations of these reactions can be found in Appendix D.

Because the initial attempts to simulate these reactions with starting structures equilibrated by the AIMD simulations failed in some cases, small changes were applied to the initial structures. To observe the methanol formation in the low water content case, a water molecule was placed near the jumping methyl group, while in case of the methoxide formation at high water content, the aromatic species was rotated to point the ethyl group in the direction of the Brønsted acid sites. In the other two simulations, the initial structures were not adapted. This manual formation of the pre-reactive complex might cause the observed reaction barrier to be lower limits for the actual barriers, since the formation of pre-reactive complexes costs energy, which is not taken into account.

The metadynamics simulations result in 2D free energy surfaces, similar to those obtained for the methylation of HMB. Therefore, this 2D surface can be projected onto a 1D surface as explained in Section 4.5. The resulting free energy profiles are depicted in Figure 6.22 for the low water content cases. Due to the order in which the collective variables were defined, HMMC is the right hand side state while the R_{JMe1} intermediate is found on the left hand side of the reaction profile. Clearly some rough bumps remain in the profile after one recrossing, which indicates that further simulation of the system is necessary. The results are however useful to get an idea of the probability for this reaction to occur.

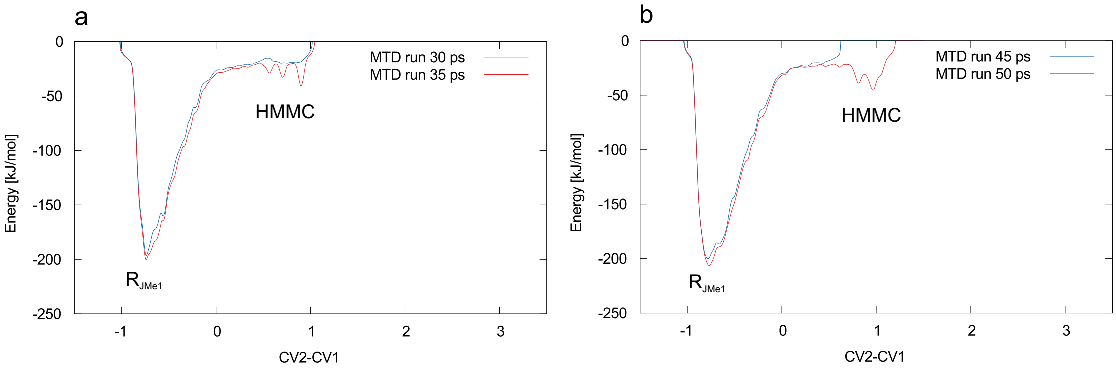

Figure 6.22: The 1D free energy profile obtained from the projection of the 2D free energy surfaces resulting from metadynamics simulation at 623 K of the methylation of HMMC in the low content case for methylation by methanol (a) and methoxide (b).

When looking at the profiles, HMMC is indeed found as an unstable intermediate relative to the R_{JMe1} intermediate in correspondence with the results of the AIMD simulations discussed in Chapter 5. This becomes even more clear when looking at the obtained reaction barriers summarized in Table 6.3. The forward barrier is taken from HMMC to R_{JMe1} with a transition state around 0.5.

The obtained reaction barrier for the methylation of HMMC (34 kJ/mol) is very low, approximately half of the barrier obtained for the same reaction with HMB (82 kJ/mol) as given in Table 6.1. When comparing the obtained barriers with the static result from literature[64], the difference is immense, since a barrier of 98.1 kJ/mol was found. This again demonstrates the importance of temperature and entropy effects on the stable intermediates in reaction cycles. Subsequently, the difference between a methylation

Table 6.3: Reaction barriers for the methylation of HMMC.

	$\Delta\overrightarrow{G}^{\ddagger}$ [kJ/mol]	$\Delta\overleftarrow{G}^{\ddagger}$ [kJ/mol]
low water content		
methanol	34	192
methoxide	38	198

using methanol or methoxide can be analyzed by comparing the barriers for methylation with both in the low water content case. As can be seen from Table 6.3, both forward and backward barriers are quite similar for both cases. Both barriers are slightly higher for the methylation with a methoxide species, though the difference is similar to the height of the added Gaussian hills and further sampling with lower hills might decrease this difference. Besides similar reaction barriers, similar transition states are found as depicted in Figure 6.23. When methanol is formed, the protonated methanol is found to adsorb at the BAS, which is suggested to be a more stable configuration as discussed in Section 6.1. Due to the similar barrier and transition state, methoxide species are suggested to be viable intermediates in the methylation reactions and that competition between the concerted and stepwise mechanism may rather be determined by which reactants are close to one another.

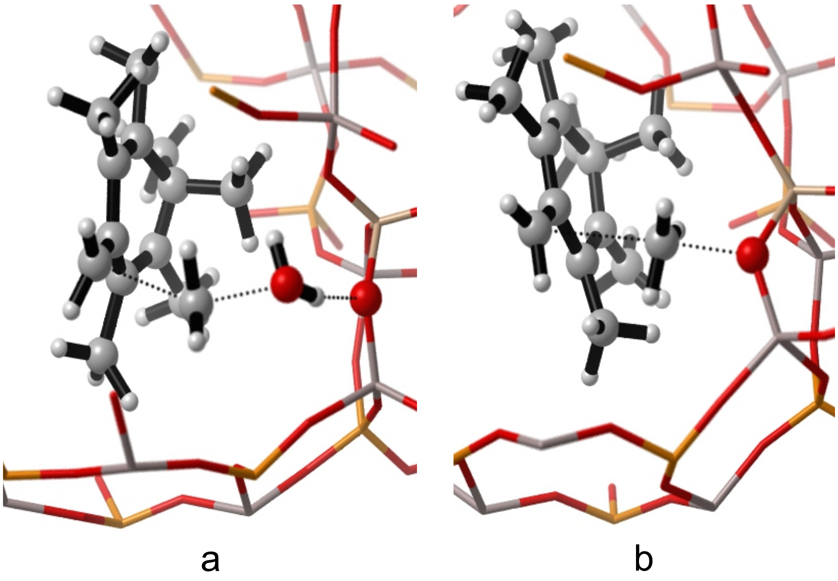

Figure 6.23: Snapshot of the metadynamics simulation at 623 K showing the transition state of the methylation of HMMC in the low content case for methylation by methanol (a) and methoxide (b).

Furthermore, the influence of water on the methylation mechanism could not be analyzed because no crossing of the barrier was found yet for the high water content simulations.

6.4 Methyl jumps

In the next step of the side-chain mechanism, the gem-methyl group (in para position with respect to the ethyl group) migrates to the ethyl group via three methyl jumps. This leads to sp^3 hybridization at the ethyl group, leading to a weakened C-C bond, which is found to be one of the conditions for a low barrier for olefin elimination by De Wispelaere et al.[64]

All methyl jumps occur similarly and therefore the collective variables used will be discussed for only one of the reactions. The example is represented in Figure 6.24 and represents the second methyl jump. These methyl jumps are described by a linear combination of two collective variables. The first part of the linear combination, CV1a, is a coordination number between the carbon of the aromatic ring that originally had two methyl groups and the carbon from the two methyl groups that could jump. The second part, CV1b, is a CN between the destination carbon of the aromatic ring and the two methyl carbons. By implementing a linear combination of collective variables, CV1a-CV1b, the simulations should go faster, since the efficiency of the MTD method scales exponentially with the number of dimensions.[132] Furthermore, a wall was introduced to prevent the jumping methyl groups from walking around the aromatic ring, similar to the 'ring walk' discussed in Section 6.2.2. A summary of the computational details can be found in Appendix D.

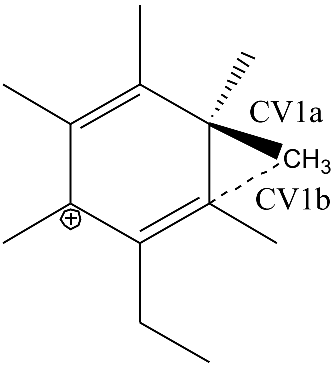

Figure 6.24: Representation of the collective variables used to simulate the second methyl jump.

Due to the use of the NVT ensemble in the metadynamics simulations, the unit cell parameters are kept constant. Again, averages are taken from the 50 ps production runs of the AIMD simulations. The values used in the simulations of the different methyl jumps are represented in Table D.10.

Since a linear combination of the collective variables is used as reaction coordinate, the resulting free energy surface is immediately one dimensional. An example is shown in Figure 6.25 for the first methyl jump at low water content. Similar results for the other methyl jumps are represented in Appendix F. When looking at these graphs, it should be mentioned that due to the way the linear combination is defined (CV1a-CV1b), the reactant state is found on the right hand side and the product state is found on the left hand side as indicated on Figure 6.25.

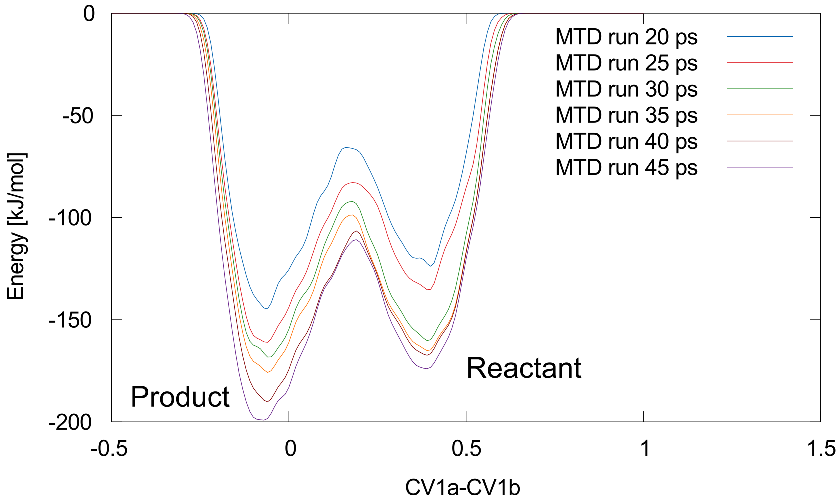

Figure 6.25: 1D free energy profile of the first methyl jump in the low water content case.

The graphs in Figure 6.25 and Appendix F demonstrate that quite smooth free energy profiles are already obtained in short simulation times, due to the use of only one simulation variable. Based on the obtained free energy profiles, forward and backward reaction barriers can again be calculated, resulting in Table 6.4.

Analysis of these results leads to several conclusions. First of all, the relative stability of the different intermediates is significantly influenced by the addition of water. At low water content, intermediate R_{JMe1} is less stable than R_{JMe2}. Furthermore, R_{JMe2} is more stable than R_{JMe3}, which is less stable than R_{EthEli}. In contrast, at high water content R_{JMe1} is more stable than R_{JMe2}, which is less stable than R_{JMe3}, which is turn is less stable than R_{EthEli}. These variations are in very good agreement with the average potential energy calculations depicted in Figure 5.14. In both cases, R_{EthEli} is found to be a relative stable intermediate. Subsequently, the reaction barrier can be analyzed. All obtained forward barriers are low enough for a viable catalytic cycle. These forward barriers can be compared with the static results.[64] The variation of the forward barrier for the different intermediates at low water content is similar to the static results, while a different variation is found for the barriers in case of a high water content. This again indicates the influence of water on the encountered intermediates, reaction mechanism and reaction rates, although a direct (de)stabilization of the transition state is not found,

Table 6.4: Free energy barrier and reaction free energy for the methyl jumps.

	$\Delta\overrightarrow{G}^{\ddagger}$ [kJ/mol]	$\Delta\overleftarrow{G}^{\ddagger}$ [kJ/mol]	ΔG_r [kJ/mol]
First methyl jump			
low water content	73	98	-25
high water content	99	88	11
static calculation[64]	88	90	-2
Second methyl jump			
low water content	94	83	11
high water content	76	98	-22
static calculation[64]	95	56	39
Third methyl jump			
low water content	58	95	-37
high water content	65	123	-58
static calculation[64]	65	145	-80

since no guest molecules diffuse to the cage with the aromatic intermediate.

6.5 Ethylene elimination

In the side-chain mechanism, the olefin elimination steps were the main bottleneck in earlier simulation attempts, since barriers around 200 kJ/mol were obtained.[55,63] More recently, low free energy barriers for the elimination of olefins were found by De Wispelaere et al.[64] due to three characteristics, depicted in Figure 6.26:

- The breaking C-C bond is already weakened due to sp^3 hybridization.
- An alkylbenzene-like complex is formed, which is stabilized by non-covalent interactions.
- Assisting water molecules ease the deprotonation of the ethyl group by facilitating the access to the active site.

It is now interesting to look whether these characteristics are also found in the ab initio molecular dynamics simulations of the R$_{EthEli}$ intermediate or if the formation of this pre-reactive complex leads to an increase of the reaction barrier. For the analysis of the first two characteristics, a comparison is made between the AIMD simulations of R$_{JMe1}$

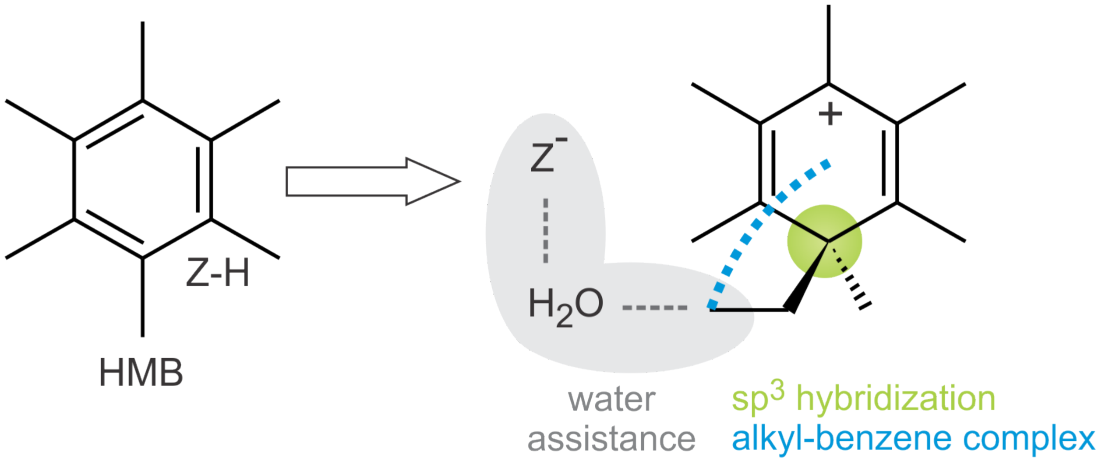

Figure 6.26: Representation of the conditions for a low barrier for olefin elimination found by De Wispelaere et al.[64]

and R_{EthEli}, as will be discussed in Section 6.5.1, while the third characteristic will be analyzed based on the metadynamics simulations discussed in Section 6.5.2.

6.5.1 Analysis of the pre-reactive complex

The first characteristic, the weakening of the breaking C-C bond, is analyzed by comparing the average length of the bonds in R_{JMe1} and R_{EthEli} indicated in Figure 6.27.

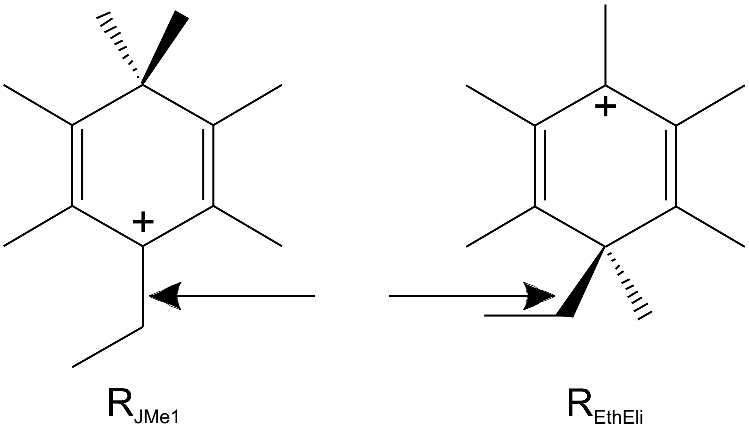

Figure 6.27: Representation of the bond lengths which are analyzed to see the weakening of the C-C bond due to sp^3 hybridization.

The length of these bonds as a function of simulation time are shown in Figure 6.28 for the high water content case. Similar results were obtained for the low water content case.

From the graphs, the C-C bond is clearly lengthened due to the sp^3 hybridization. This finding is confirmed by the calculation of the average bond length during the production run. For R_{JMe1} the average bond length was found to be 1.51 ± 0.05 Å for both low and high water content. Similarly, the average bond lengths for R_{EthEli} were found to be equal to 1.62 ± 0.08 Å and 1.62 ± 0.07 Å for low and high water content, respectively. These results show that the bond length clearly increases due to sp^3 hybridization, which means that the bond is weakened. Furthermore, it can be seen that the bond length is not influenced by the extra water in the catalyst environment.

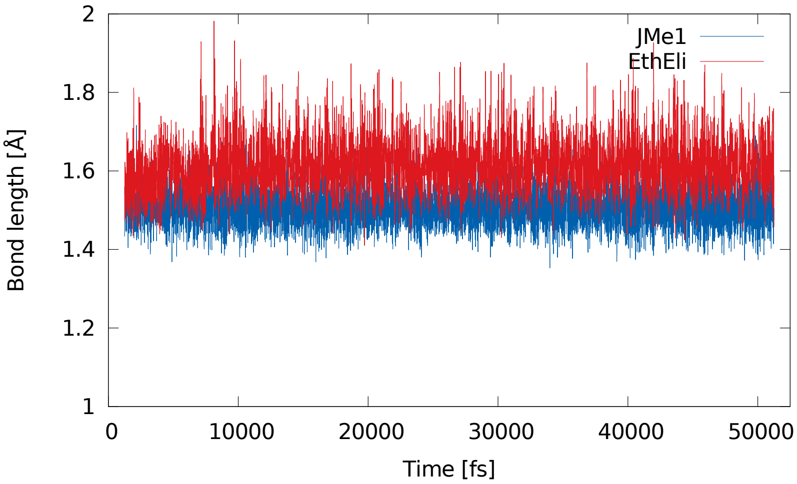

Figure 6.28: Graph showing the bond lengths represented in Figure 6.27 in function of time of the AIMD simulation at 623 K and 1 atm, both for the high water content case.

The formation of an alkylbenzene-like complex is analyzed by comparing the dihedral angle defined by the carbon atoms 1-4 indicated in Figure 6.29, again for R_{JMe1} and R_{EthEli}.

The graphs of these dihedral angles in function of simulation time are shown in Figure 6.30 for the high water content case, which are similar to the results obtained for the low water content case. By analyzing these results, it can be concluded that for R_{EthEli}, the ethyl group stays oriented to the aromatic ring, because the dihedral angle stays between -50° and 50°. This becomes even clearer when looking at Figure 6.31, where the rotation of this dihedral angle between -50° and 50°is represented. For R_{JMe1} on the other hand, there is no clear orientation, since the dihedral can vary from -180° to 180°, which means that the ethyl group can make an entire rotation. The results do show that there are two configurations at 0° and 180° which are more stable than the others, while R_{EthEli} stays in one oriented configuration during the entire simulation.

On Figure 6.30, it can also be seen that in the simulation for R_{EthEli} the ethyl group is oriented towards the aromatic ring at the start of the simulation. This means that

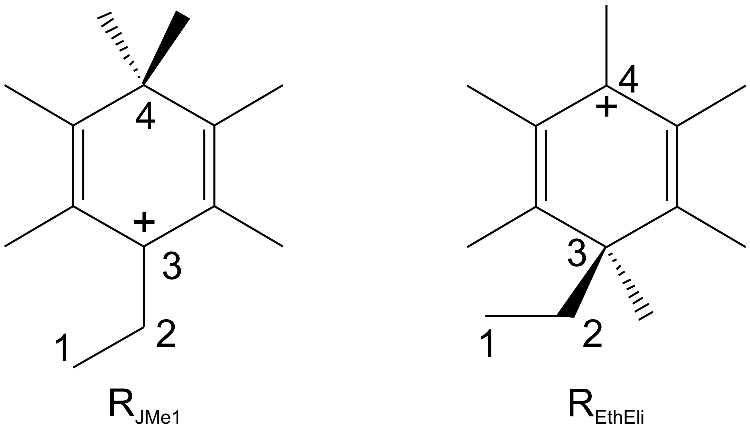

Figure 6.29: Representation of the dihedral angles which are analyzed to see the formation of the alkylbenzene-like complex.

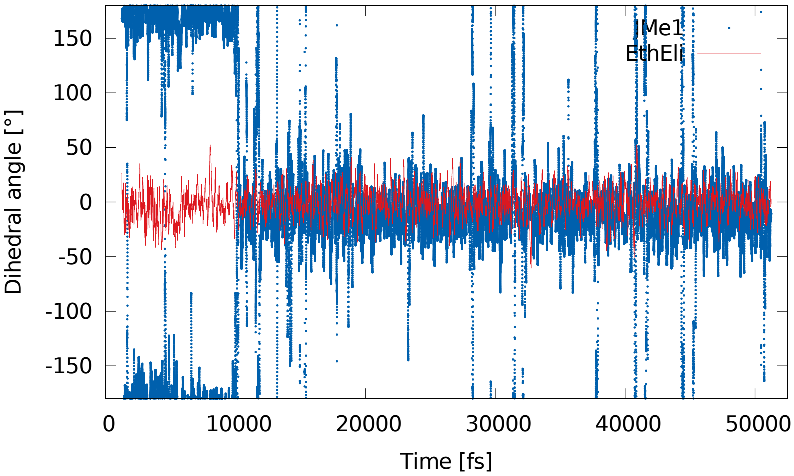

Figure 6.30: Graph showing the dihedral angles represented in Figure 6.29 in function of time of the AIMD simulation at 623 K and 1 atm, both for the high water content case.

once the ethyl group is oriented to the aromatic ring, it maintains this orientation, but it can not be concluded yet that this orientation occurs naturally. Therefore, an extra simulation is needed in which the ethyl group has been rotated in order to break the orientation. The resulting graph of the dihedral angle as a function of simulation time is shown in Figure 6.32 for both the low and high water content case. After some time, the dihedral angle comes in the -50° to 50° range, meaning that it orients itself toward the aromatic ring. The results again show that once favorable orientation occurs, it remains in the alkylbenzene-like complex. Furthermore, the results show that the orientation occurs faster in the high water content case.

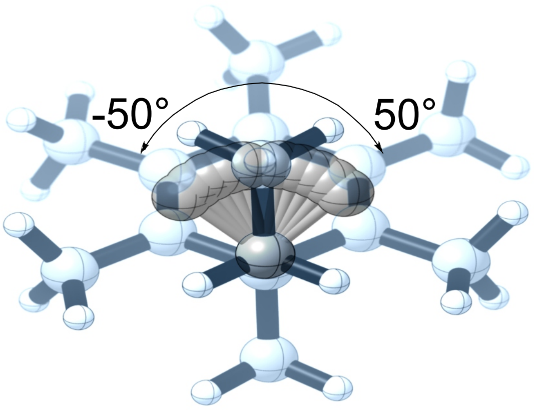

Figure 6.31: Representation of the dihedral angle rotation between -50° and 50° for R_{EthEli}.

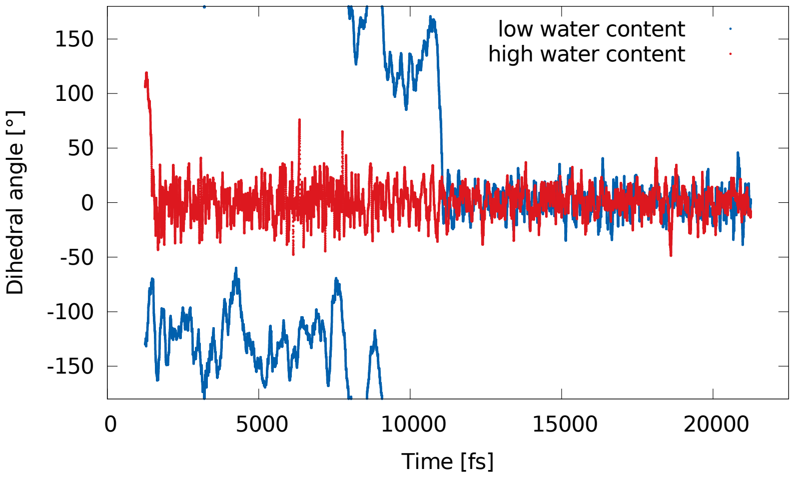

Figure 6.32: Graph showing the dihedral angles of R_{EthEli} represented in Figure 6.29 in function of simulation time, both for the low and high water content case when the initial structure is not oriented to the aromatic ring.

As stated earlier, the third characteristic will be determined by comparison of the metadynamics simulations for the low and high water content. This will be discussed in the subsequent section.

6.5.2 Simulation of the ethylene elimination

The last step of the side-chain mechanism, the ethylene elimination, was simulated using a linear combination of two collective variables, which are depicted in Figure 6.33. The first part of the linear combination, CV1a, is a coordination number between the carbon and the three hydrogens of the CH_3 tail of the ethylene group. The second part, CV1b, is a CN between those three hydrogens and all oxygens to which they can be transferred (oxygens of water and BAS). On the second part of the linear combination, a wall was placed to keep an oxygen in the neighborhood of the jumping hydrogens. This linear combination thus induces a proton transfer between the ethyl group and an oxygen of water or BAS. Similarly as for the deprotonation of heptaMB$^+$, a proton is transfered in this reaction, which has a low mass and inertia which make it susceptible to the addition of Gaussian hills to the free energy surface, leading to high accelerations. This was again avoided by artificially increasing the mass of all hydrogen atoms to 3.0 a.u. during the metadynamics simulations.[103,133]

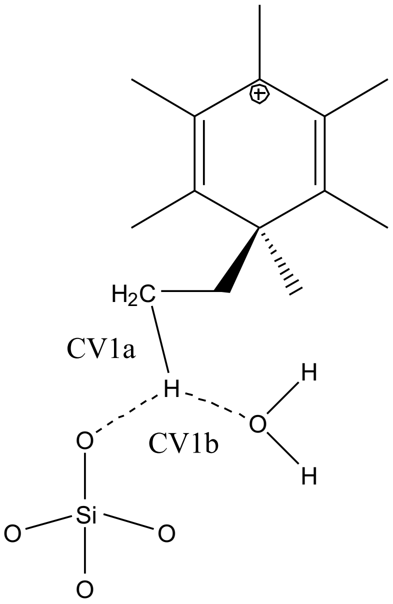

Figure 6.33: Representation of the collective variables used to simulate the ethylene elimination.

In the first attempts to simulate this reaction, another collective variable was introduced, namely a CN between the two carbon atoms of the breaking bond. In these simulations the C-C bond breaking is easier than breaking the C-H bond, which means that deprotonation is the rate limiting step. This led to the formation of ethoxide species instead of the formation of ethylene, which might mean that at realistic reaction conditions, the ethylene elimination does not only go via a concerted mechanism, as found by the static calculations[64], but also via a stepwise mechanism with ethoxide species as intermediates. Therefore, it might be interesting to start a simulation with three collective variables, also accounting for ethoxide species. Due to time limitation, these simulations were not yet executed. Instead, this second collective variable was removed, because breaking of the C-H was anticipated to also break the C-C bond, which turned out to be true.

Another wall was added, but only for the low water content case. In this case, the formed ethylene was found to diffuse away from HMB, thus lowering the probability of a recrossing. Since the focus of these simulations is on the reaction barrier and not on the diffusion limitations, this diffusion is inhibited by a wall on the length of the breaking C-C bond. This wall was not added in the high water content case, since the additional water was expected to limit the diffusion of the formed ethylene.

During the metadynamics simulations in the NVT ensemble, the unit cell parameters given in Table D.12 were used.

Since a collective variable is introduced on the breaking C-C bond to limit the length of this bond in the low water content case, this collective variable can be followed in function of time during the simulation. It is interesting to plot this collective variable together with CV1, which introduced the elimination reaction, to see if the breaking of the C-H bond actually leads to elimination of the ethylene. These two collective variables are depicted in Figure 6.34. As can be seen on this graph, a stepwise mechanism is also suggested by these results, since the reforming of the C-H bond occurs around 72 ps and the formation of C-C bond only occurs at 75 ps. Furthermore, two aberrations are observed. Firstly, around 66 ps, CV1 decreases, meaning that the C-H bond is formed, while the C-C bond is not formed. This is also depicted in the snapshot of Event 1, which shows that an ethyl group is formed that is adsorbed on an acid site. This is a similar configuration as found between 72 and 75 ps, meaning that this might be an intermediate step in the ethylene elimination.

A second unexpected configuration is found around 71 ps. Here, one of the hydrogens of ethylene is shared with water, as can be seen in the snapshot of Event 2. It is possible that this structure is formed due to the definition of CV1. Since all three hydrogens are taken into account, energy is also added to the other two C-H bonds, which might lead to configurations as in Event 2. Both events are not found during the high water content case. Though another problem occurs in this simulation, namely the diffusion of the formed ethylene to neighboring cage, as depicted in Figure 6.35, which was expected to be limited by the water present. Furthermore, the formed ethylene does not diffuse back to the cage with the aromatic intermediate, so a second recrossing is not observed. This leads to an increase in the backward barrier, which is actually a diffusion barrier, therefore making this backward barrier meaningless.

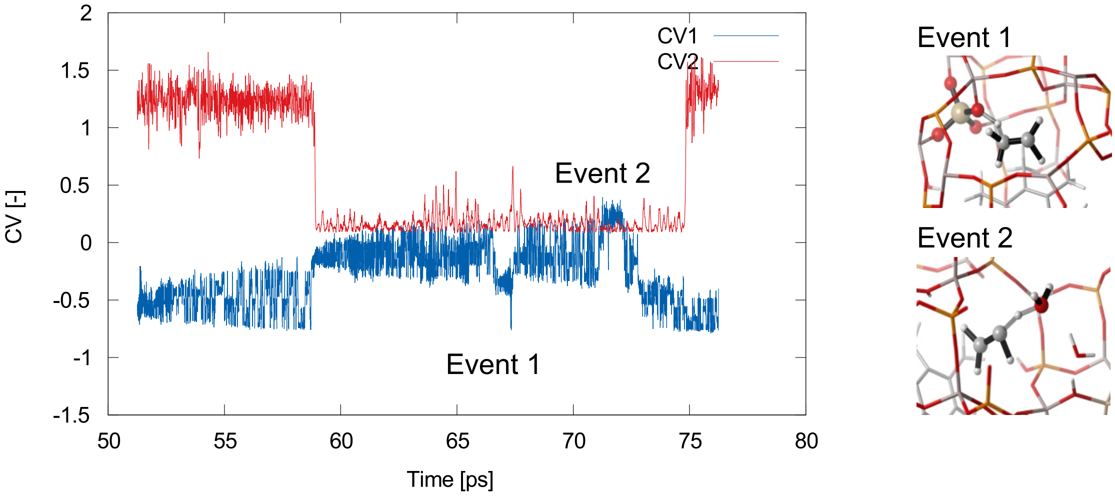

Figure 6.34: The collective variables used for the MTD simulation at 623 K of the ethylene elimination with low water content in function of simulation time. CV1 is a linear combination of the collective variable CV1a and CV1b defined in Figure 6.33 and CV2 is the collective variable introduced to place a wall on the breaking C-C bond.

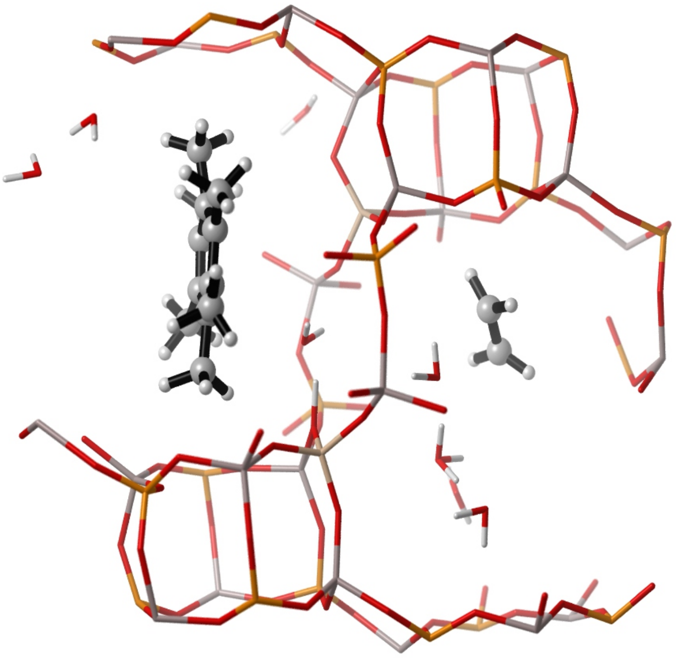

Figure 6.35: Snapshot of the MTD simulation at 623 K of the ethylene elimination at high water content, showing the diffusion of ethylene to a neighboring cage.

Alhough some unwanted events occur during the MTD simulation of the ethylene elimination and the breaking of the C-C and C-H do not necessarily occur simultaneously, an estimate of the ethylene elimination reaction barrier can be obtained by analyzing the barrier for the C-H bond breaking. The free energy profiles are depicted in Figure 6.36. In the low water content case, in which the deviating events occur, the reaction profile is significantly influenced by Event 1 (formation of an adsorbed ethyl group). Since the collective variables describing this configuration overlap with the transition state, the barrier incorrectly decreases and becomes meaningless. Nevertheless, an estimate of the barrier can be obtained from the free energy profile after the first forward barrier crossing after 10 ps MTD simulation. Here, a barrier of 141 kJ/mol is found. Moreover, the aberrant events do not occur in the high water content case, so the forward barrier can be calculated from the free energy profile obtained after 40 ps. This barrier is found to be equal to 116 kJ/mol, which is significantly lower than at low water content. When looking at the transition states of the ethylene elimination depicted in Figure 6.37, the decrease of the barrier is not attributed to the assistance of water, but occurs because the orientation between the ethyl chain and the aromatic ring is lost at low water content. Therefore, the influence of water on this reaction could not be determined. To verify this effect on the ethylene elimination, simulations are suggested where the alkylbenzene-like complex and the water assistance is imposed. Both free energy barriers are higher than the static barrier of 99.3 kJ/mol.[64]

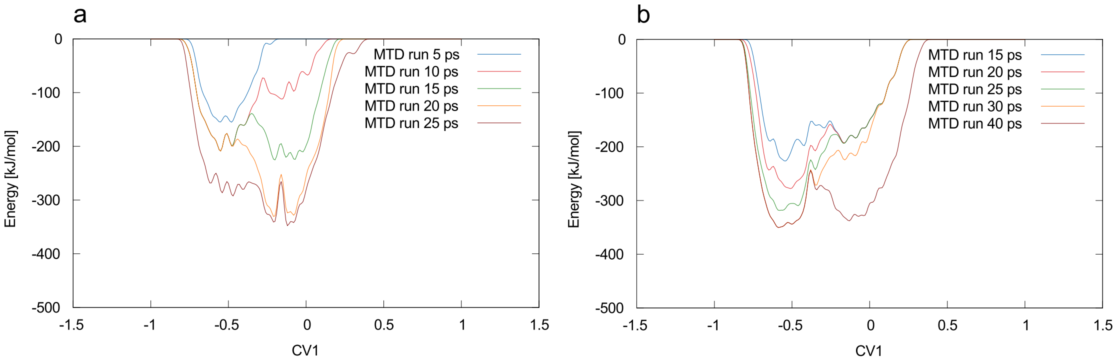

Figure 6.36: The 1D free energy profiles of the ethylene elimination in low (a) and high (b) water content case.

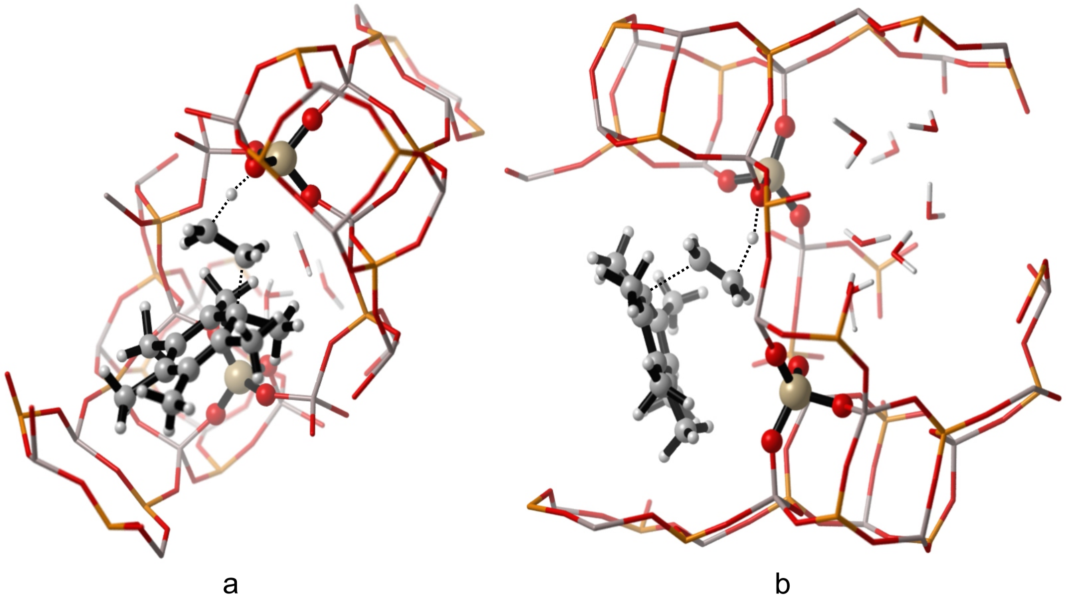

Figure 6.37: Snapshot of the transition state of the ethylene elimination in low (a) and high (b) water content case, showing that the alkyl-benzene orientation is lost at low water content.

Based on the results of the MTD simulations of the ethylene simulation it is suggested to execute simulations with three collective variables. One collective variable describing the breaking of the C-C bond, a second describing the breaking of the C-H bond and formation of the H-O bond (as used in this thesis) and a third describing the formation of the C-O of an ethoxide species. These simulations might unravel the role of the absorbed ethyl group and ethoxide in the ethylene elimination reaction.

6.6 Conclusion

In this chapter, the influence of water on the free energy barriers for the reactions in the side-chain cycle was investigated using metadynamics simulations at 623 K. Furthermore, the effect on the competition between the side-chain mechanism and the paring mechanism was analyzed by additionally considering the free energy barrier of the onset reaction of the paring mechanism.

The first considered reaction is the methylation of HMB, which is the first step in both the side-chain and paring mechanism. The resulting free energy barriers show a decrease with increasing water content from 91 kJ/mol with no water content to 72 kJ/mol at high water content. This decrease in the reaction barrier is thought to be due to a destabilization of the protonated methanol with increasing water loading, which is in agreement with the results of Chapter 5. Furthermore, the role of a methoxide in the methylation reaction has been analyzed. Although the simulations have not completely converged yet, the available results suggest that the methoxide species is a plausible intermediate in the MTO process.

In the subsequent reaction step, both mechanism differ and thus the competition between both can be examined. From the reaction occurring in the side-chain cycle, the deprotonation of heptaMB$^+$, it was confirmed that HMMC is an unstable intermediate at the used conditions. For this reaction, a decrease in the free energy barrier was found with in increased water loading from 91 kJ/mol at low water content to 77 kJ/mol at high water content. This might be due to the stabilization of H_3O^+ by the formation of a cluster with the additional water. The competing reaction of the paring mechanism is the ring contraction of heptaMB$^+$, which is suggested to be a two step reaction. Only the first step is considered in the calculation of the free energy barrier, though some interference of the second reaction step was found which possibly led to an underestimation of the reaction barrier obtained from the 1D simulations. Nevertheless, an estimate of the forward free energy barrier could be obtained from the 2D simulation at high water content. This barrier was found to be 124 kJ/mol, which is higher than the 77 kJ/mol barrier for the deprotonation of heptaMB$^+$ at high water content, suggesting the side-chain mechanism as prevailing cycle in H-SAPO-34

Next, the dependence of the free energy barriers of the subsequent reactions in the side-chain mechanism on the water loading was studied. The following reaction that occurs is the methylation of HMMC. Here, the influence of water could not be determined, since no results were available at high water content. Nevertheless, the competition between methylation with methanol and methoxide could be analyzed. Both reactions exhibit similar free energy barriers, 34 kJ/mol for methanol and 38 kJ/mol for methoxide, which again suggests that methoxides might occur as intermediates.

Subsequently, three methyl jumps take care of the migration of the gem-methyl group to the ethyl group, which weakens the C-C bond that breaks in the subsequent ethylene elimination. The free energy barrier of the reactions and the stability of the intermediates are found to be altered due to the loading of additional water, though a direct (de)stabilization is not found, since the guest molecules do not diffuse to the cage in which the reaction takes place.

Lastly, the ethylene elimination was considered. First of all, the characteristics for a low barrier suggested by De Wispelaere et al.[64] were analyzed via the results of the AIMD simulations. This examination showed that the two of the conditions were fulfilled and the third, the assistance of water, could be studied via the results of the metadynamics simulations. At low water content, an ethyl adsorbed at the BAS was found as a stable intermediate, which led to a spurious decrease of the free energy barrier. Nevertheless, an estimate of the free energy barrier could be obtained using the free energy profile after the first crossing of the barrier. A barrier of 140 kJ/mol was found. For the high water content simulation, a barrier of 116 kJ/mol was found. This decrease of the free energy barrier could not be attributed to an assistance of water during the reaction. Loss of the orientation of the ethyl chain to the aromatic ring at low water content was found to increase the barrier.

Chapter 7

Conclusion and outlook

Due to the growing importance of renewable resources, interest in the MTO process has grown since it is one of the most prominent technologies to bypass crude oil in the production of light olefins. Research on the reaction mechanism governing this MTO process has been ongoing for years. Various experimental techniques have been used to unravel the mechanism, but because of the large number of reactions that take place simultaneously, it is difficult to get information on the individual reaction steps. Here, theoretical simulations can offer additional understanding, since these are capable of analyzing individual reactions and intermediates. Combined efforts of experimental and theoretical research resulted in the general acceptance of the hydrocarbon pool mechanism governing the MTO process. In this mechanism, a hydrocarbon is trapped in the catalyst framework and acts as a co-catalyst. In H-SAPO-34, which is of particular industrial interest due to its high selectivity to light olefins, polymethylbenzenes are identified as HP species. Based on these aromatic intermediates two reaction cycles have been proposed, the side-chain and paring mechanism.

Several reaction conditions, such as temperature, pressure and methanol space time, influence the yield and selectivity of the MTO process over an H-SAPO-34 catalyst. Another interesting influence to analyze is that of water, since it is both a byproduct of the methanol synthesis and the MTO process itself. Experimental research has shown that at high water loadings, competitive adsorption of water and methanol forces the methanol to diffuse deeper in the catalyst to find an available adsorption site. To get a more detailed understanding of the importance of these events, the dependence of the governing reaction mechanism and stability of the intermediates of the MTO process on the water loading was investigated on a molecular level.

To get insight on a molecular level, theoretical simulations were executed, since they offer the advantage of isolating individual elementary steps. In the past, these ab initio simulations were executed on stationary systems at 0 K, but in this dissertation dynamic simulations were used. These dynamic simulations have the advantage that they account for temperature effects, entropic effects and the influence of surrounding solvent molecules. Since the aim is to investigate the influence of water at MTO reaction conditions, i.e., 623 K and 1 atm, dynamic simulations are essential.

In the first part of this thesis, the influence of water on the stability and mobility of the aromatic intermediates was evaluated. Therefore, several characteristics were considered based on ab initio molecular dynamics simulations at 623 K and 1 atm. First, it was observed that water influences the time-averaged unit cell volume. To get more detailed information, the unit cell parameters and volume of the simulations of HMB were compared at different loadings. The introduction of the aromatic intermediate led to a 4 % volume expansion of the framework compared to the empty unit cell. Inclusion of a methanol led to an extra expansion of 0.2 %. In contrast, the introduction of eight water molecules to the unit cell led to a volume contraction of 1.2 %. Furthermore, the analysis of the unit cell parameters showed the anisotropy of this expansion, since the main variation was found along the c-axis. This is because the flexible 8-ring windows are directed parallel to this axis, while the more rigid 6-ring windows are perpendicular to this axis. These results are in good correspondence with the reported experimental XRD results of Wragg et al.[70]

Subsequently, it was investigated whether the contraction of the framework due to the higher water loading decreases the mobility of the aromatic intermediate trapped in the catalyst framework. When analyzing the orientation of the aromatic species in the H-SAPO-34 cages, a clear trend is found for the most stable configuration. A rotation occurs compared to the initial structure to take advantage of the full length of the cage. To see the influence of water on the mobility of the aromatic intermediate, the time this rotation takes was compared for different water loadings. No clear relation between the tendency towards rotation and the water loading was found. Additionally, the influence of the composition of the catalyst framework on this rotation was investigated by repeating the analysis for a heptaMB$^+$ cation in the H-SSZ-13 framework, which has the same chabazite topology as H-SAPO-34, but a different chemical composition, leading to a higher acid strength. The results suggested that there is no influence of these catalyst properties on the rotation of the aromatic intermediate.

Nevertheless, Brønsted acidity is known to be an important aspect of the MTO catalyst. Since the methanol was found to be protonated during a methylation reaction[59], the proton mobility in the H-SAPO-34 pores was investigated. Therefore, the dependence of the probability of the H-SAPO-34 framework to deprotonate on the water loading was analyzed, which showed an increase of the probability at higher water content due to the formation of protonated water clusters. Furthermore, the influence of the acid strength was examined by comparison of the H-SAPO-34 results with the simulation of heptaMB$^+$ in the H-SSZ-13 framework, which clearly showed an increase in the deprotonation probability. Additionally, the influence of a higher water loading on the formation of protonated methanol was considered, since water and methanol are found to adsorb competitively.[59] A decrease of the protonation of methanol was found at higher water content.

Lastly, the relative stability of the intermediates in the side-chain cycle were compared to the stability obtained via static calculations reported by De Wispelaere et al.[64] Here, a clear difference was observed, since the enthalpy obtained via the static calculations resulted in a destabilization of the cationic intermediates relative to HMB, while the average potential energies from the dynamic calculations show a stabilization. Furthermore, the influence of an increased loading of water in the catalyst pores on the stability of the aromatic intermediates was examined via comparison of the average potential energies when three guest molecules are present in the catalyst pores to the average potential energies obtained when eight extra water molecules are added. This addition of water led to a destabilization of the cationic intermediates compared to the results at low water content, except for heptaMB$^+$.

In the second part of this thesis, the dependency of the free energy barriers of the reactions in the side-chain mechanism on the water loading was studied via metadynamics simulations at 623 K. Additionally, the water influence on the competition between the side-chain and paring mechanism was considered by evaluating the free energy barrier of the onset of the paring mechanism. The simulation of the reaction cycles was started from HMB, since it is identified as a crucial HP species[21,68] and it was used as the starting point for the static calculations.[64]

The first step in both mechanisms is the methylation of HMB, which showed a decrease of the free energy barrier from 82 kJ/mol to 72 kJ/mol with an increase of eight water molecules in the catalyst unit cell. This decrease of the reaction barrier was thought to be caused by a decreased probability of the formation of protonated methanol due to the competition with water, which was discussed in the first part of the thesis. This might lead to destabilization of the protonated methanol at increased water loading and thus to a decrease of the barrier. Since two mechanisms are suggested for the methylation reaction, the concerted and stepwise mechanism, competition between both can be assessed via simulations in which the mechanism is not imposed. Therefore, a MTD simulation was executed with three collective variables in which the importance of methoxide species, the intermediate in the stepwise mechanism, in methylation reactions was considered. Though the simulations did not reach complete convergence yet, the available results suggested methoxide species as a viable intermediate, meaning that at the simulated conditions, the concerted and stepwise methylation mechanisms can compete.

The side-chain and paring mechanism differ in their second reaction step, therefore the competition between both mechanism can be analyzed by comparing the free energy barrier of both reactions. The next step in the side-chain mechanism is the deprotonation of the heptaMB$^+$ cation. MD simulations showed that at high temperature HMMC spontaneously protonates forming the heptaMB$^+$ cation, which was confirmed by the free energy surface obtained by the MTD simulations. Furthermore, the free energy barrier of this reaction decreases from 91 kJ/mol at low water content to 77 kJ/mol at high water loading, which might be due to a stabilization of the formed H_3O^+ by the formation of a cluster with the additional water. The onset reaction of the competing paring mechanism, the ring contraction of heptaMB$^+$, is suggested to be a two step reaction. First, the 6-ring contracts to form a 5- and 3-ring and subsequently one of the bonds of the 3-ring break forming a isopropyl chain on the 5-ring. In this thesis, only the free energy barrier of the first reaction is considered, though some interference of the second step was found during the 1D simulation, since the formation of an isopropyl group was sampled at higher simulation times, which might have led to a spurious decrease of the reaction barrier. Nevertheless, an estimate of the forward free energy barrier could be obtained from the 2D simulation at high water content. A barrier of 124 kJ/mol was found, which is higher than the barrier for the competing deprotonation of heptaMB$^+$ at high water content, suggesting the side-chain cycle as prevailing mechanism in H-SAPO-34.

Next, the influence of water on the subsequent side-chain cycle reactions was examined. The reaction occurring after the deprotonation of heptaMB$^+$ is the methylation of HMMC. The influence of water on this reaction could not be determined, since no results were available at high water content. However, the importance of the stepwise methylation could be determined via the comparisons of the methylation with methanol and a methoxide species. The similar resulting barriers, 34 kJ/mol for methanol and 38 kJ/mol for methoxide, suggest that methoxide species are plausible intermediates. The low free energy barriers suggest HMMC as an unstable intermediate, which was confirmed by the fact that no 50 ps production run for the AIMD simulations could be obtained, since HMMC was spontaneously protonated forming heptaMB$^+$.

The next three steps in the side-chain cycle are methyl jumps by which the gem-methyl group migrates to the ethyl group, weakening the C-C bond that breaks in the ethylene elimination. Analysis of the free energy profiles shows that the stability of the different intermediates in these methyl jumps and the free energy barriers between them were found to be shifted by the addition of water, although a direct (de)stabilization was not found, because water does not directly interact with the reacting aromatic intermediate.

The last considered reaction is the elimination of ethylene for which characteristics for a low barrier were suggested by De Wispelaere et al.[64] Two conditions, namely a sp^3 carbon center of the organic intermediate weakening the breaking C-C bond and stabilizing non-bonding interactions forming an alkylbenzene-like complex, were found to be fulfilled during the AIMD simulations. On the other hand, the third condition, the assistance of water, could be analyzed by comparing the free energy barriers obtained from the MTD simulations at low and high water content. Some difficulties were encountered, since an ethyl adsorbed at the BAS was found as a stable intermediate. This led to a unphysical decrease of the free energy barrier, rendering the results less useful to define the barrier quantitatively. Nevertheless, an estimate of the barrier could be obtained via the energy profile after the first recrossing, before the aberrant event occurred. This led to a barrier of 141 kJ/mol. Furthermore, the adsorbed ethyl was not found at high water content, such that a more certain barrier could be obtained. Here, a barrier of 116 kJ/mol was found, which is significantly lower than the low water content case. This decrease could not be attributed to an assistance of water, rather the loss of the orientation between the ethyl chain and the aromatic ring at low water content was suggested to increase the barrier.

Based on the results presented here, it is clear that water has a significant influence on some key aspects of the MTO process. First, a higher water loading leads to a volume contraction, though this was not found to have an influence on the mobility of the aromatic intermediate. Furthermore, the addition of water led to an increased framework deprotonation and a decreased methanol protonation, which might lead to a delay in the MTO process. On the other hand, water stabilized H_3O^+ formed during the deprotonation of heptaMB$^+$, leading to a decrease of the barrier. So water has both promoting and delaying effects. Unfortunately, the effect of water on the competition between the paring and side-chain mechanism could not be determined. Nevertheless, the side-chain mechanism could be established as the prevailing mechanism at high water content.

Though extra insight into the mechanism governing the MTO process is obtained, there is still a lot of research necessary to unravel the exact mechanism. A better understanding of the mechanism can be obtained via additional theoretical simulations. Based on the results presented here on the side-chain cycle, extra simulations could be started to get more certainty on the obtained results. For example, the role of the adsorbed ethyl group and ethoxide species in the ethylene elimination reactions could be examined further via multidimensional MTD simulations, explicitly accounting for ethoxide formation.

In literature, the importance of properly accounting for the nuclear quantum effects (NQE) when simulating proton transfer in water has been emphasized. Because protons have a low mass, an error is introduced due to the approximation of the nuclei as classical particles.[135,136] These NQE were not accounted for in this thesis, but it could be interesting to examine the effect of the NQE on simulations performed herein, since proton transfer is found to be important in the MTO process.

Next to the investigation of the side-chain mechanism, an examination of the entire paring cycle might unravel the feasibility of this mechanism. Here, the use of dynamic simulations can have an important role, since these can account for realistic reaction conditions and for the interaction with guest molecules as was shown in this thesis. Furthermore, the influence of acidity via the comparison of H-SAPO-34 with H-SSZ-13 might lead to additional insight. All these considerations emphasize that there are still a lot of questions regarding the MTO process. The gaps in the knowledge of the reaction mechanism can potentially be bridged by further joint experimental and theoretical research.

Appendix A

Orientation of the aromatic ring in the catalyst cage

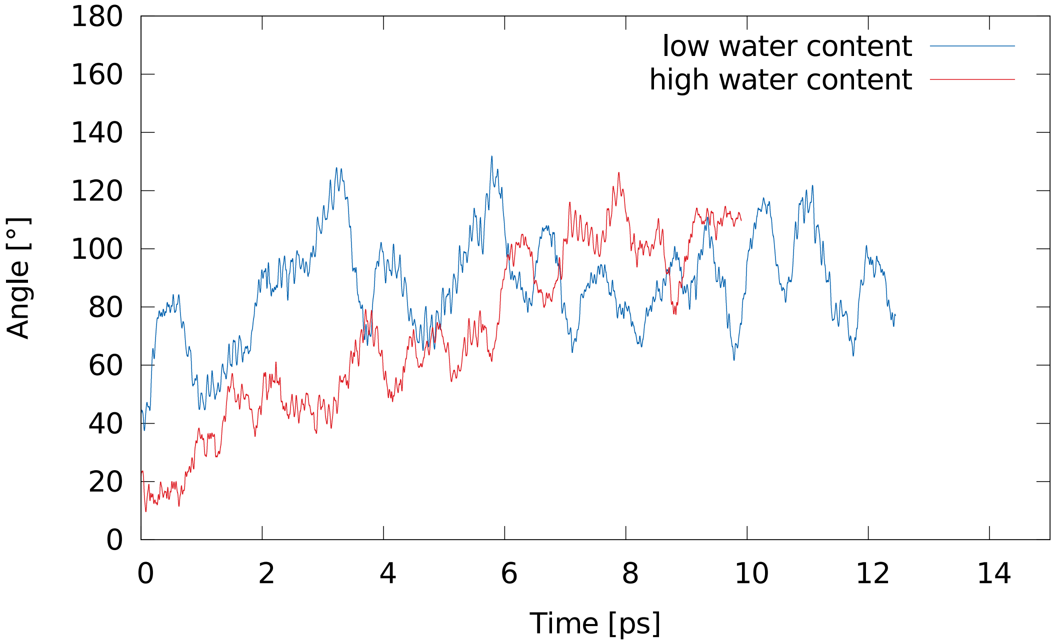

Figure A.1: Angle between the normal of the plane of the aromatic ring and the normal of the plane of the catalyst framework indicated in Figure 5.3, as function of time for the AIMD simulation of heptaMB$^+$ at 623 K and 1 atm.

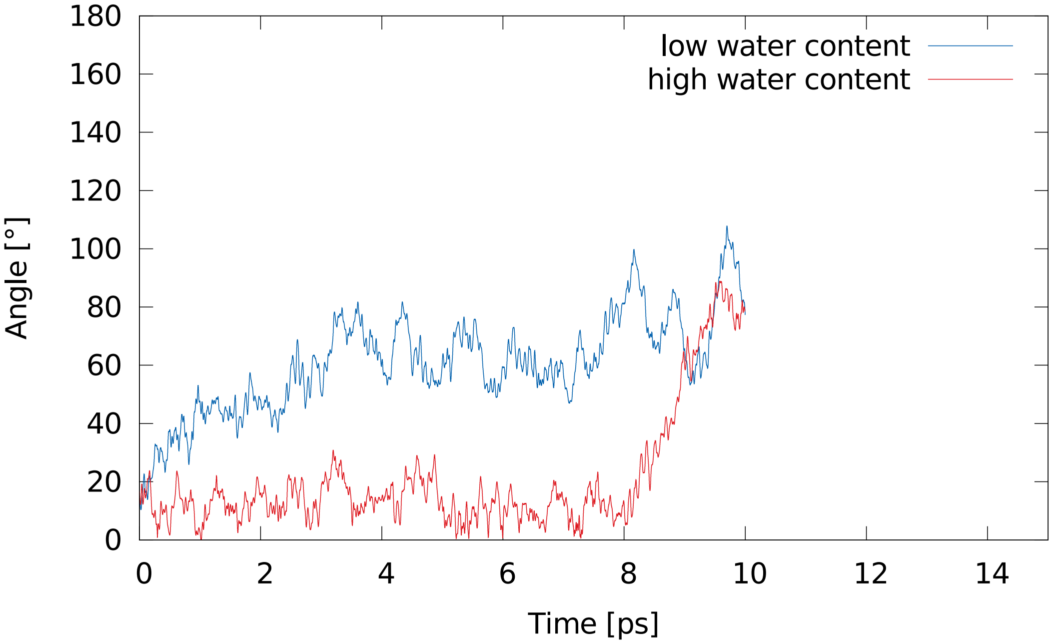

Figure A.2: Angle between the normal of the plane of the aromatic ring and the normal of the plane of the catalyst framework indicated in Figure 5.3, as function of time for the AIMD simulation of R_{JMe1} at 623 K and 1 atm.

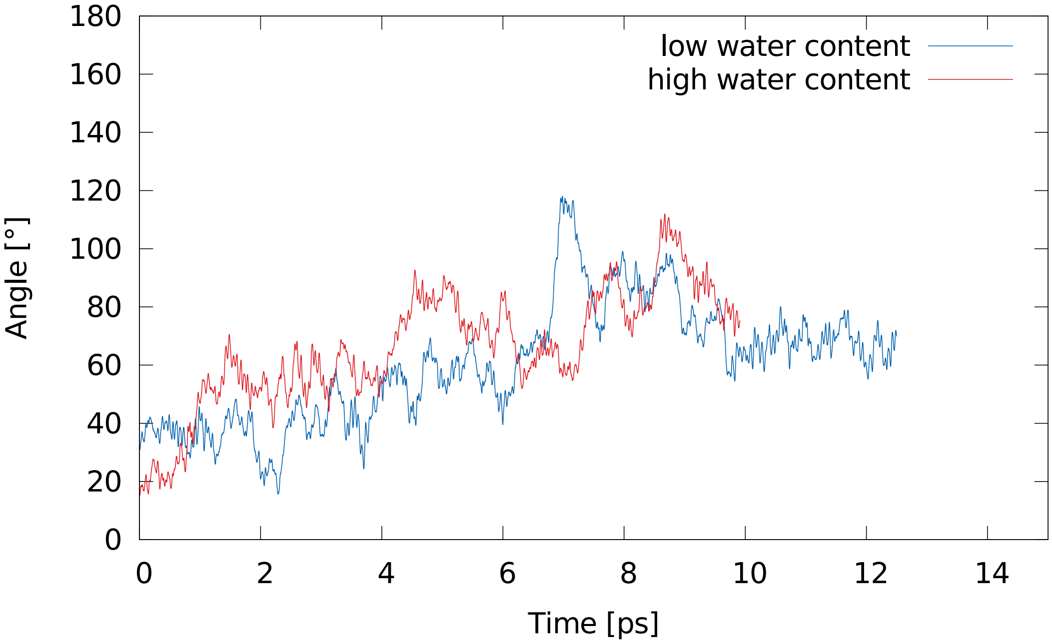

Figure A.3: Angle between the normal of the plane of the aromatic ring and the normal of the plane of the catalyst framework indicated in Figure 5.3, as function of time for the AIMD simulation of R_{JMe2} at 623 K and 1 atm.

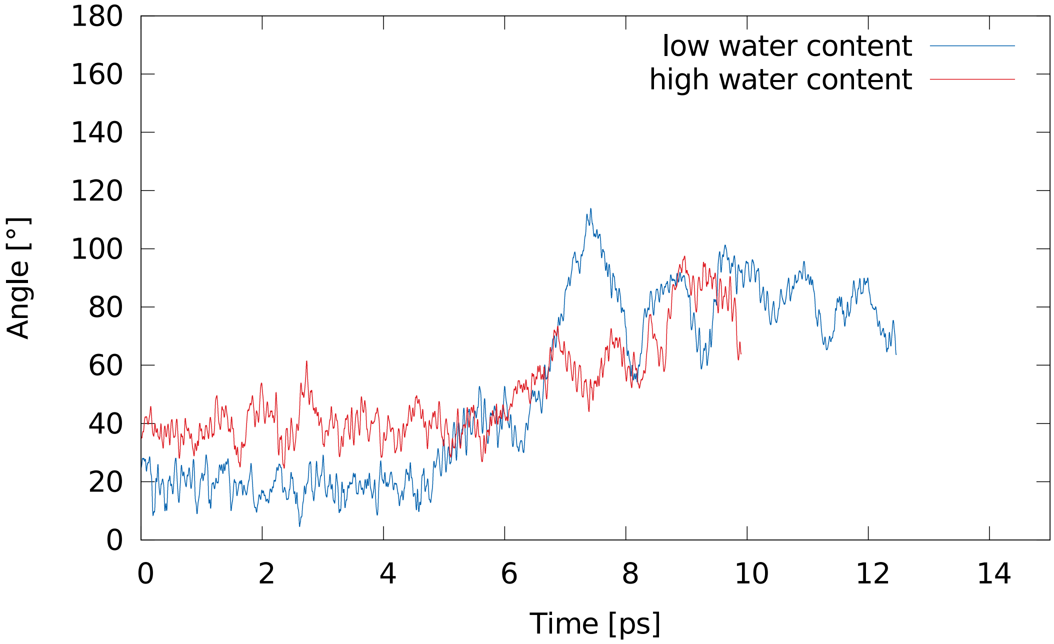

Figure A.4: Angle between the normal of the plane of the aromatic ring and the normal of the plane of the catalyst framework indicated in Figure 5.3, as function of time for the AIMD simulation of R_{JMe3} at 623 K and 1 atm.

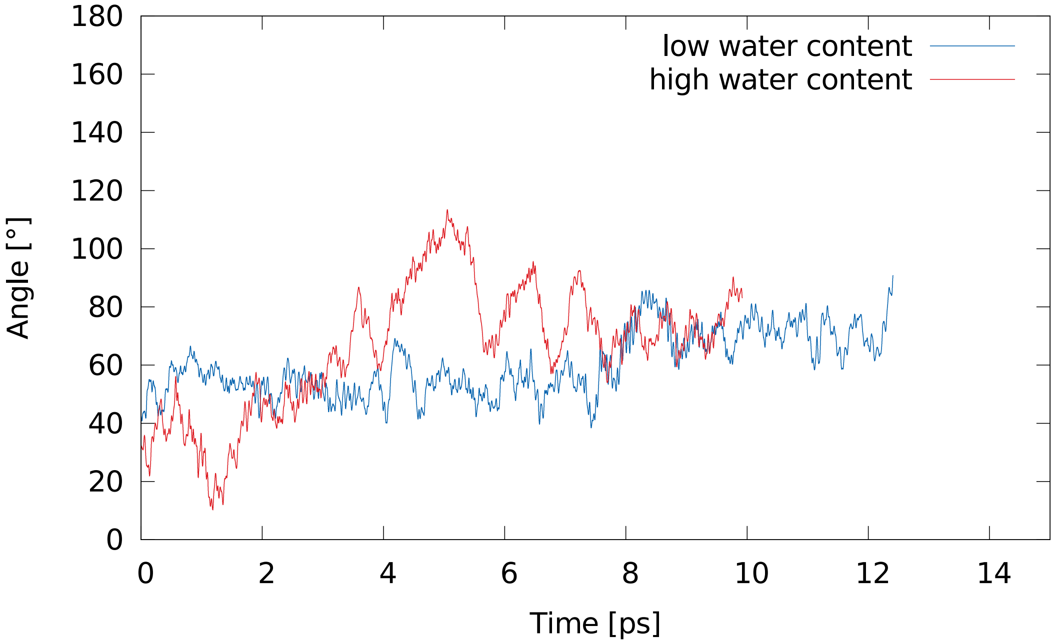

Figure A.5: Angle between the normal of the plane of the aromatic ring and the normal of the plane of the catalyst framework indicated in Figure 5.3, as function of time for the AIMD simulation of R_{EthEli} at 623 K and 1 atm.

Appendix B

Convergence of the framework deprotonation fractions

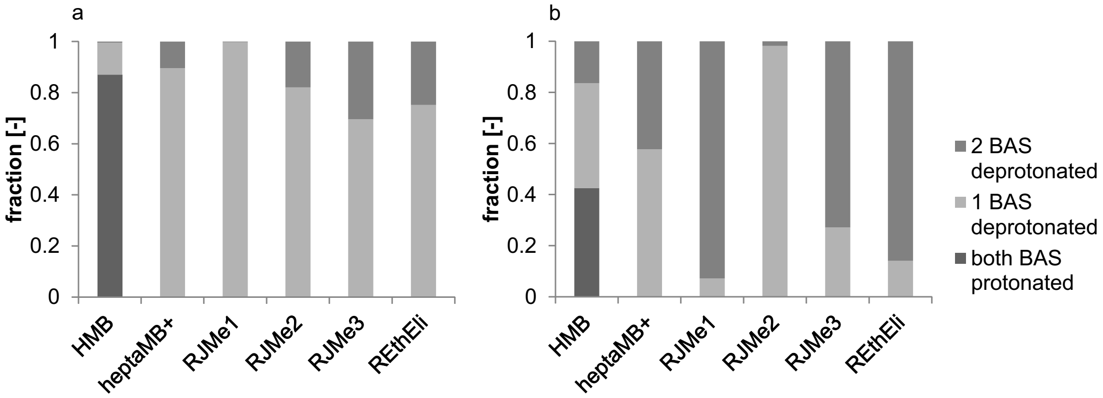

Figure B.1: Fraction of the 30 ps AIMD simulation at 623 K and 1 atm in which the Brønsted acid sites of the H-SAPO-34 framework are (de)protonated for low water content (a) and high water content (b).

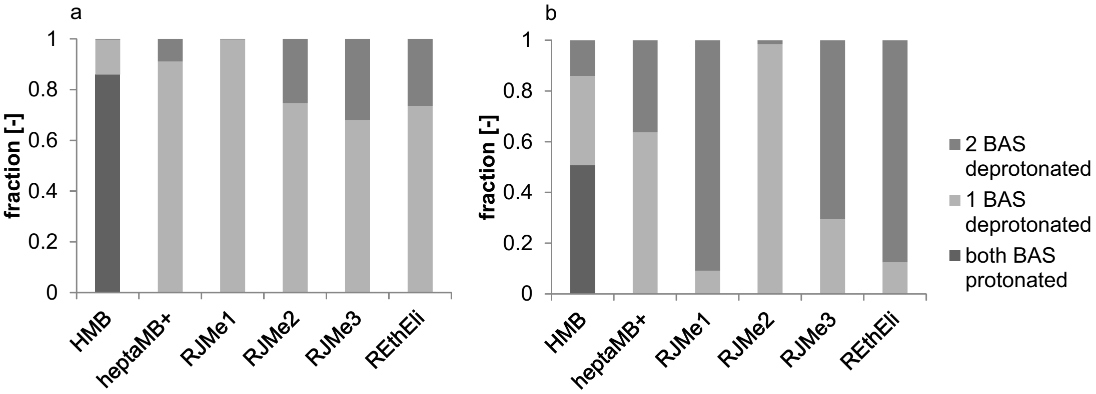

Figure B.2: Fraction of the 35 ps AIMD simulation at 623 K and 1 atm in which the Brønsted acid sites of the H-SAPO-34 framework are (de)protonated for low water content (a) and high water content (b).

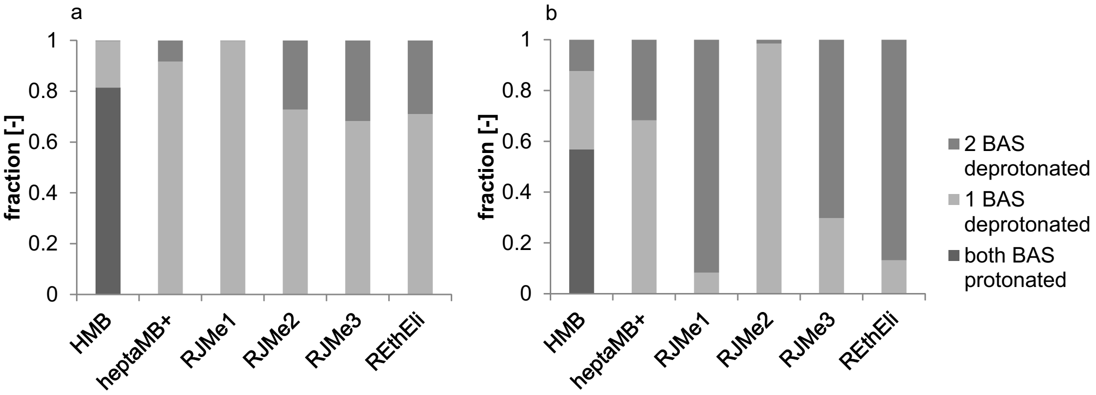

Figure B.3: Fraction of the 40 ps AIMD simulation at 623 K and 1 atm in which the Brønsted acid sites of the H-SAPO-34 framework are (de)protonated for low water content (a) and high water content (b).

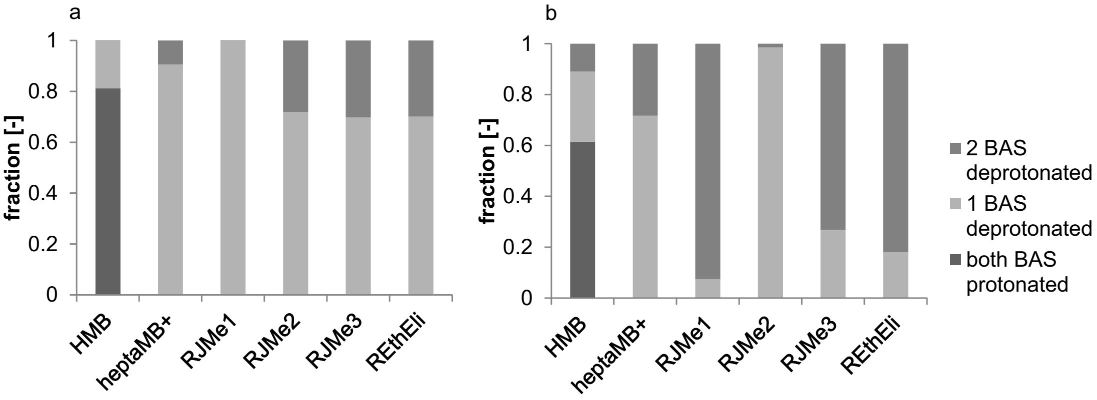

Figure B.4: Fraction of the 45 ps AIMD simulation at 623 K and 1 atm in which the Brønsted acid sites of the H-SAPO-34 framework are (de)protonated for low water content (a) and high water content (b).

Appendix C

Calculation of the uncertainty on the potential energy profile

For the comparison of the relative stability of the intermediates of the side-chain mechanism the average potential energy is taken over the 50 ps production runs of the AIMD simulations at 623 K and 1 atm for each intermediate. There is thus an uncertainty in these results, which is estimated as follows.

The estimation is started by calculating the average potential energy at different times along the simulation, namely from 0 - 25 ps , 0 - 30 ps , ... and 0 - 50 ps, leading to the averages given in Table C.1 and C.2 for low and high water content, respectively.

Table C.1: Average potential energy in kJ/mol for the different intermediates of the side-chain cycle over the production run of the AIMD simulation at 623 K and 1 atm at low water content.

Intermediate	**25 ps**	**30 ps**	**35 ps**	**40 ps**	**45 ps**	**50 ps**
HMB	-3819067	-3819081	-3819084	-3819090	-3819093	-3819101
heptaMB$^+$	-3819147	-3819148	-3819146	-3819149	-3819149	-3819150
R$_{JMe1}$	-3819173	-3819177	-3819187	-3819192	-3819196	-3819199
R$_{JMe2}$	-3819196	-3819202	-3819206	-3819206	-3819210	-3819210
R$_{JMe3}$	-3819160	-3819169	-3819178	-3819176	-3819173	-3819175
R$_{EthEli}$	-3819212	-3819211	-3819217	-3819214	-3819213	-3819216

Table C.2: Average potential energy in kJ/mol for the different intermediates of the side-chain cycle over the production run of the AIMD simulation at 623 K and 1 atm at high water content.

Intermediate	**25 ps**	**30 ps**	**35 ps**	**40 ps**	**45 ps**	**50 ps**
HMB	-4181401	-4181400	-4181396	-4181404	-4181408	-4181407
heptaMB$^+$	-4181454	-4181459	-4181462	-4181461	-4181461	-4181462
R$_{JMe1}$	-4181443	-4181449	-4181452	-4181449	-4181451	-4181454
R$_{JMe2}$	-4181435	-4181431	-4181430	-4181427	-4181429	-4181433
R$_{JMe3}$	-4181434	-4181436	-4181437	-4181444	-4181447	-4181451
R$_{EthEli}$	-4181480	-4181484	-4181490	-4181488	-4181487	-4181486

Subsequently, for each intermediate, the difference between its average potential energy and the average potential energy of the corresponding simulation of HMB is taken (So the first row is subtracted from all other rows). So for each part of the simulation, an average potential energy relative to the simulation of HMB is obtained for each intermediate, leading to the values given in Table C.3 and Table C.4. From these relative potential energies, a standard deviation is calculated. The relative average potential energies at 50 ps are plotted together with the standard deviations, which are used as the error bars, in Figure 5.14.

Table C.3: Average potential energy relative to the simulation of HMB in kJ/mol for the different intermediates of the side-chain cycle over the production run of the AIMD simulation at 623 K and 1 atm at low water content.

Intermediate	**25 ps**	**30 ps**	**35 ps**	**40 ps**	**45 ps**	**50 ps**	ST.DEV.
HMB	0	0	0	0	0	0	0
heptaMB$^+$	-80	-67	-62	-60	-56	-49	11
R$_{JMe1}$	-107	-96	-103	-103	-103	-98	4
R$_{JMe2}$	-129	-122	-122	-116	-116	-108	7
R$_{JMe3}$	-93	-89	-93	-86	-80	-73	8
R$_{EthEli}$	-146	-131	-132	-124	-120	-115	11

Table C.4: Average potential energy relative to the simulation of HMB in kJ/mol for the different intermediates of the side-chain cycle over the production run of the AIMD simulation at 623 K and 1 atm at high water content.

Intermediate	**25 ps**	**30 ps**	**35 ps**	**40 ps**	**45 ps**	**50 ps**	**ST.DEV.**
HMB	0	0	0	0	0	0	0
heptaMB$^+$	-53	-59	-66	-58	-53	-55	5
R_{JMe1}	-42	-49	-56	-46	-42	-47	5
R_{JMe2}	-34	-31	-34	-23	-21	-26	6
R_{JMe3}	-33	-36	-41	-41	-39	-44	4
R_{EthEli}	-80	-84	-94	-85	-78	-78	6

Appendix D

Summary of the extra computational details of the metadynamics simulations

D.1 Methylation of HMB

Table D.1: Collective variables and the quadratic walls applied to them in the MTD simulations of the methylation of HMB, discussed in Section 6.1.

CV	**r_0 [Å]**	**Position**	**K[a] [kJ/mol]**	**Direction**	**hills**
CV1	2.0	0.01	262550	attractive	yes
CV2	2.0	0.008	2625500	attractive	yes
CVextra1	1.0	0.03	262550	attractive	no
CVextra2	1.0	0.03	262550	attractive	no
CV3	2.0	-	-	-	yes

[a] The quadratic potential is defined as $K(CV\text{-}position)^2$

Table D.2: Unit cell dimensions used during the metadynamics simulations of the methylation of HMB.

	a [Å]	b [Å]	c [Å]	α [°]	β [°]	γ [°]
no water content	14.0459	14.0875	14.9751	89.3912	89.4265	120.0022
low water content	14.1964	14.1259	14.8852	90.1375	90.0210	119.2900
high water content	14.0003	14.3649	14.8665	90.7687	90.3745	120.6415

D.2 Deprotonation of heptaMB$^+$

Table D.3: Collective variables and the quadratic walls applied to them in the MTD simulations of the deprotonation of heptaMB$^+$, discussed in Section 6.2.1.

CV	**r_0 [Å]**	**Position**	**K^a [kJ/mol]**	**Direction**	**hills**
CV1	1.2	-	-	-	yes
CV2	1.2	0.05	262550	attractive	yes
CVextra1	1.2	0.1	262550	attractive	no
CVextra2	1.2	0.1	262550	attractive	no

^{a} The quadratic potential is defined as K(CV-position)^2

Table D.4: Unit cell dimensions used during the metadynamics simulations of the deprotonation and ring contraction of heptaMB$^+$.

	a [Å]	b [Å]	c [Å]	α [°]	β [°]	γ [°]
low water content	14.2676	14.2187	14.9660	90.3233	89.8742	120.8376
high water content	14.0007	14.1944	14.9024	89.7705	90.2219	118.8699

D.3 Ring contraction of heptaMB$^+$

Table D.5: Collective variables and the quadratic walls applied to them in the 2D MTD simulations of the ring contraction, discussed in Section 6.2.2.

CV	**r_0 [Å]**	**Position**	**K[a] [kJ/mol]**	**Direction**	**hills**
CV1	2.0	-	-	-	yes
CV2	2.0	-	-	-	yes
CVextra1	2.0	0.55	262550	repulsive	no

[a] The quadratic potential is defined as K(CV-position)^2

Table D.6: Collective variables and the quadratic walls applied to them in the 1D MTD simulations of the ring contraction, discussed in Section 6.2.2.

CV	**r_0 [Å]**	**Position**	**K[a] [kJ/mol]**	**Direction**	**hills**
CV1	2.0	-	-	-	yes
CV2	2.0	1.2	262550	attractive	no
CVextra1	2.0	0.55	262550	repulsive	no

[a] The quadratic potential is defined as K(CV-position)^2

D.4 Methylation of HMMC

Table D.7: Collective variables and the quadratic walls applied to them in the MTD simulations of the methylation of HMMC with methanol, discussed in Section 6.3.

CV	**r_0 [Å]**	**Position**	**K[a] [kJ/mol]**	**Direction**	**hills**
CV1	2.0	-	-	-	yes
CV2	2.0	0.075	262550	attractive	yes

[a] The quadratic potential is defined as K(CV-position)^2

Table D.8: Collective variables and the quadratic walls applied to them in the MTD simulations of the methylation of HMMC with a methoxide species, discussed in Section 6.3.

CV	**r_0 [Å]**	**Position**	**K^a [kJ/mol]**	**Direction**	**hills**
CV1	2.0	-	-	-	yes
CV2	2.0	-	-	-	yes

^{a} The quadratic potential is defined as K(CV-position)^2

D.5 Methyl jumps

Table D.9: Collective variables and the quadratic walls applied to them in the MTD simulations of methyl jumps, discussed in Section 6.4.

CV	**r_0 [Å]**	**Position**	**K^a [kJ/mol]**	**Direction**	**hills**
CV1a	2.0	-	-	-	yes
CV1b	2.0	-	-	-	yes
CVextra	2.0	0.35	262550	repulsive	no

^{a} The quadratic potential is defined as K(CV-position)^2

Table D.10: Unit cell dimensions used during the metadynamics simulations of the methyl jumps.

	a [Å]	b [Å]	c [Å]	α [°]	β [°]	γ [°]
First jump						
low water content	13.8998	14.1560	15.0898	89.7528	90.0625	118.6915
high water content	14.2561	13.9660	15.0214	90.2464	90.3409	119.4417
Second jump						
low water content	14.2238	13.9803	14.9723	90.2170	90.4215	119.3415
high water content	14.0714	14.1350	15.0686	90.1701	89.7123	119.3683
Third jump						
low water content	14.1562	14.0196	14.9804	90.4122	89.9298	118.9783
high water content	14.1541	13.9874	15.0067	90.2988	89.8660	118.6782

D.6 Ethylene elimination

Table D.11: Collective variables and the quadratic walls applied to them in the MTD simulations of the ethylene elimination, discussed in Section 6.5.2.

CV	$\mathbf{r_0}$ **[Å]**	**Position**	**K**^{a} **[kJ/mol]**	**Direction**	**hills**
CV1a	1.2	-	-	-	yes
CV1b	1.2	0.05	262550	attractive	yes
CVextra^b	2.0	0.1	262550	attractive	no

[a] The quadratic potential is defined as $K(CV\text{-}position)^2$

[b] This wall was only applied in the low water content case

Table D.12: Unit cell dimensions used during the metadynamics simulations of the ethylene elimination.

	a [Å]	b [Å]	c [Å]	α [°]	β [°]	γ [°]
low water content	14.0420	14.3413	14.9178	90.3542	90.0236	120.4554
high water content	14.0095	13.9717	14.9476	90.0548	90.0765	117.9045

Appendix E

Collective variables of HMB methylation

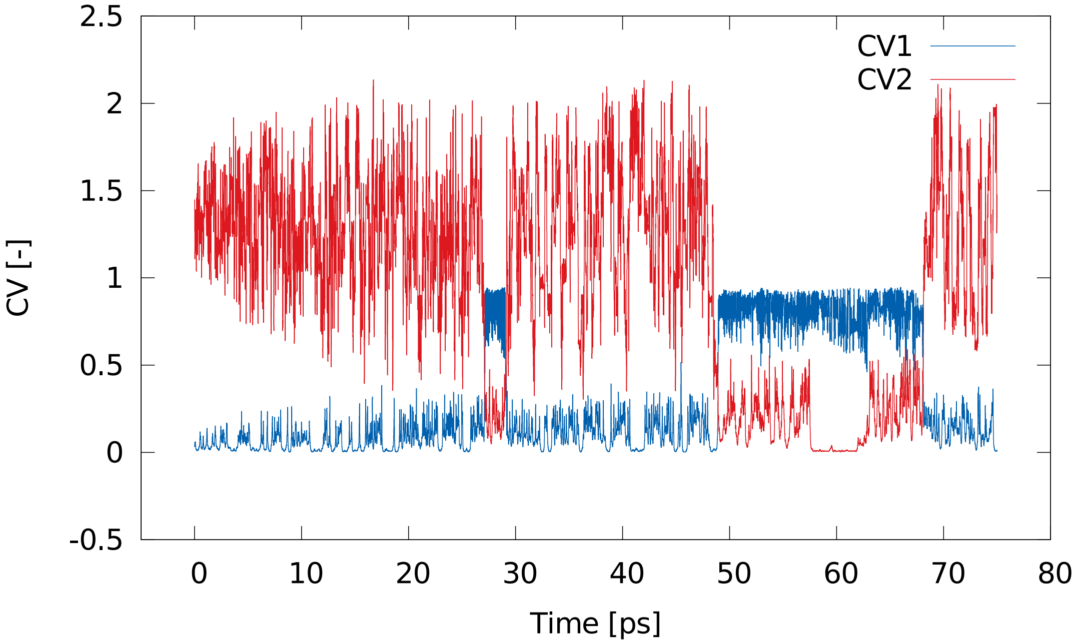

Figure E.1: The collective variables used for the methylation of HMB, which were defined in Figure 6.2, with no water content in function of the metadynamics simulation time.

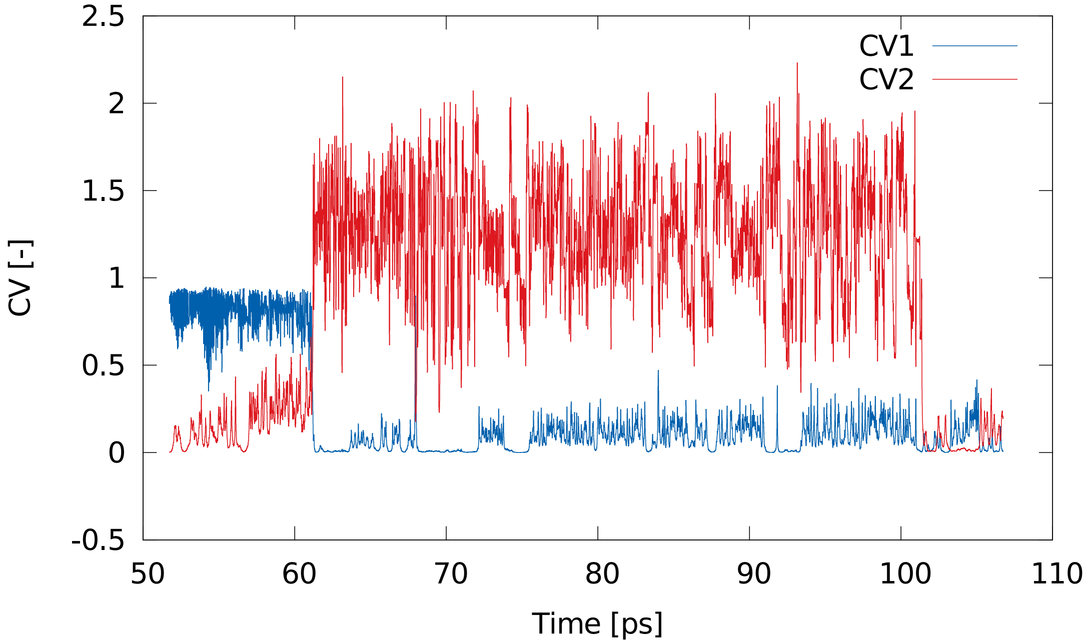

Figure E.2: The collective variables used for the methylation of HMB, which were defined in Figure 6.2, with low water content in function of the metadynamics simulation time.

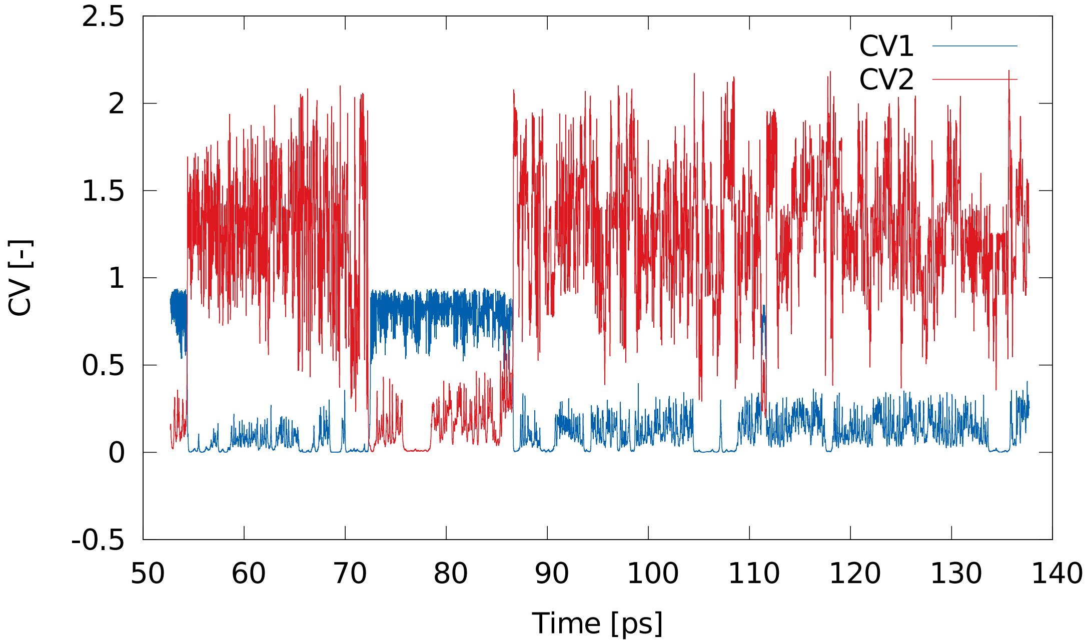

Figure E.3: The collective variables used for the methylation of HMB, which were defined in Figure 6.2, with high water content in function of the metadynamics simulation time.

Appendix F

One dimensional free energy surfaces of the methyl jumps

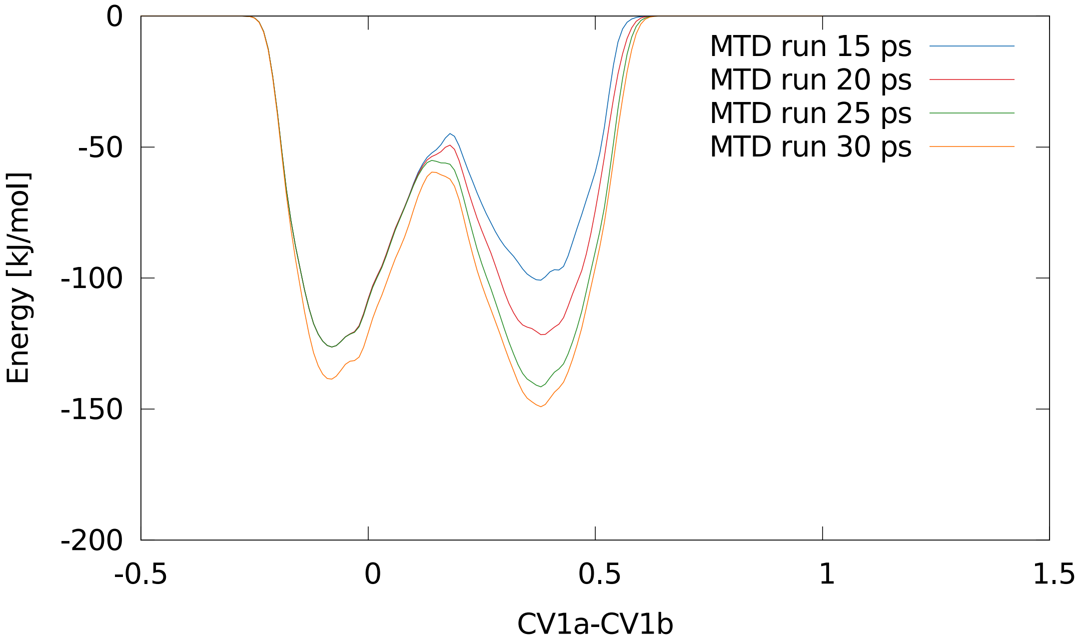

Figure F.1: 1D free energy profile of the first methyl jump in the high water content case at 623 K.

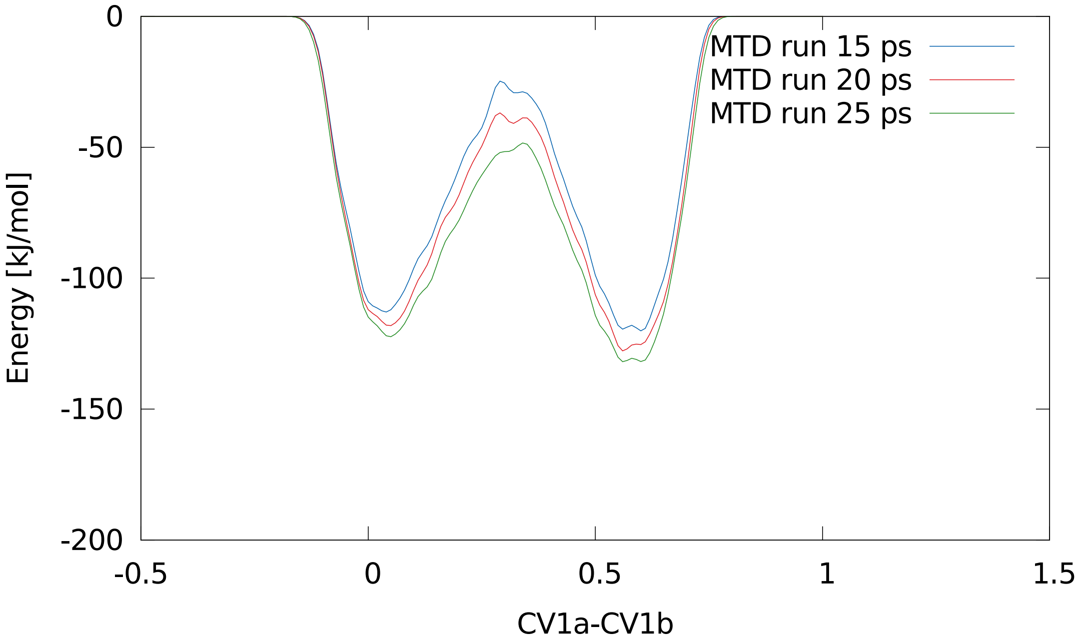

Figure F.2: 1D free energy profile of the second methyl jump in the low water content case at 623 K.

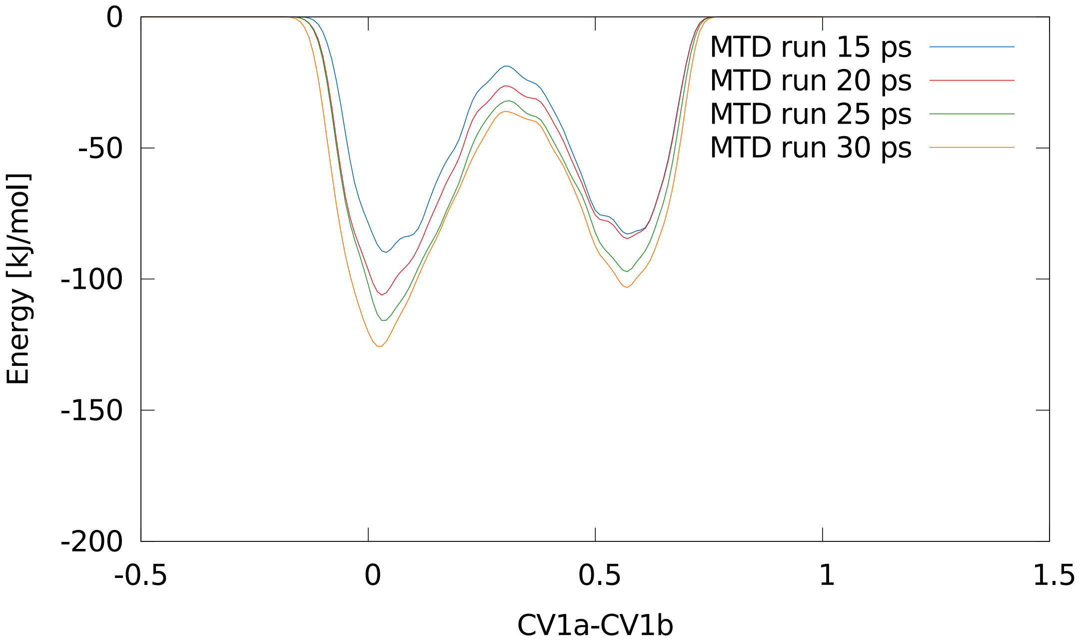

Figure F.3: 1D free energy profile of the second methyl jump in the high water content case at 623 K.

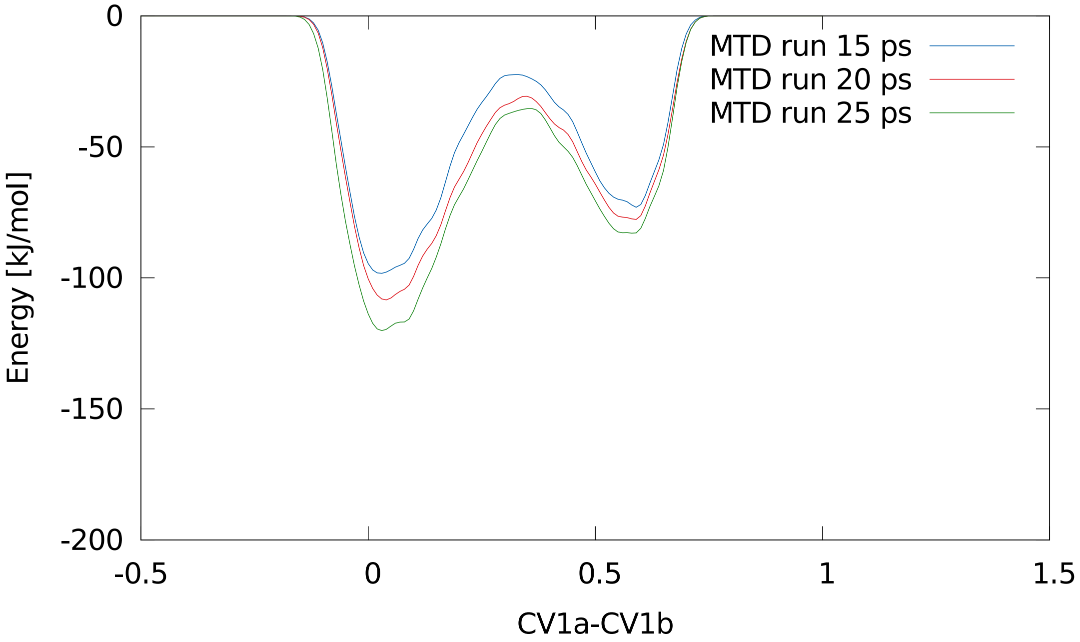

Figure F.4: 1D free energy profile of the third methyl jump in the low water content case at 623 K.

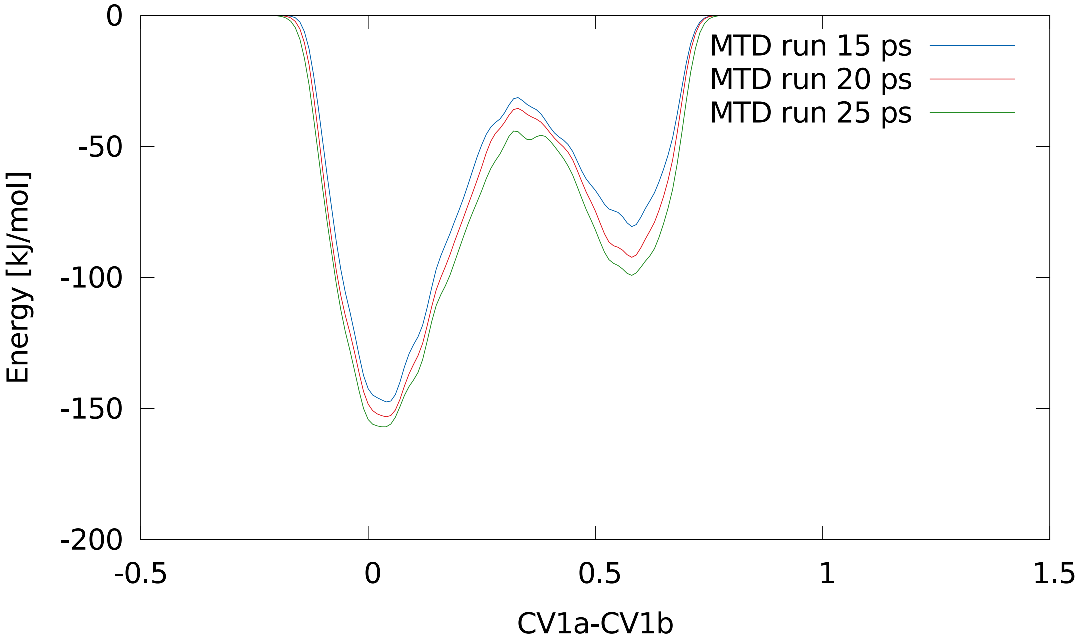

Figure F.5: 1D free energy profile of the third methyl jump in the high water content case at 623 K.

Appendix G

Poster NCCC

This appendix contains the poster which was presented on March 2 and 3 2015 at the 16th Netherlands' Catalysis and Chemistry Conference (NCCC), Noordwijkerhout (NL), as KNCV selected student.

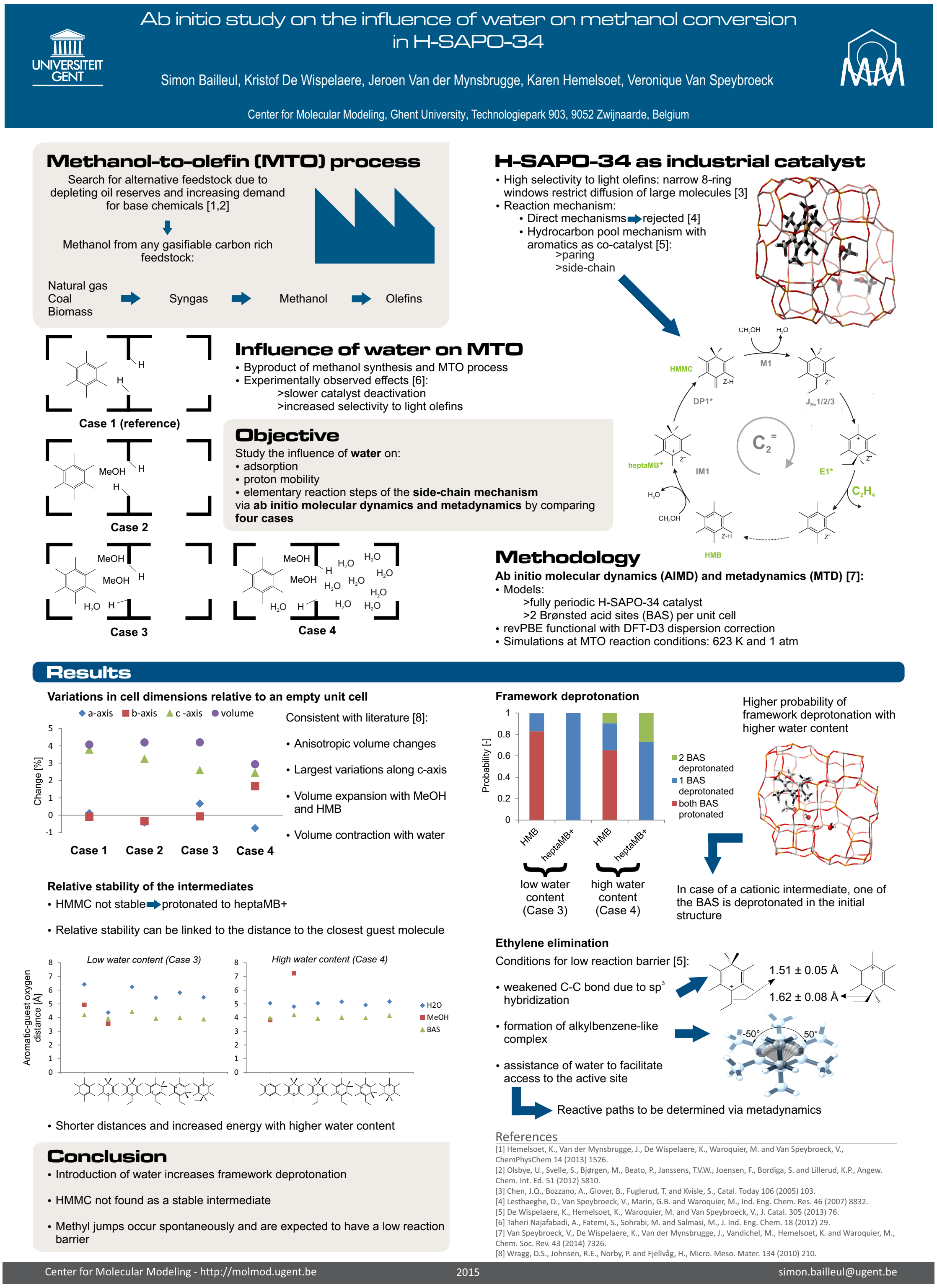

Ab initio study on the influence of water on methanol conversion in H-SAPO-34

Simon Bailleul, Kristof De Wispelaere, Jeroen Van der Mynsbrugge, Karen Hemelsoet, Veronique Van Speybroeck

Center for Molecular Modeling, Ghent University, Technologiepark 903, 9052 Zwijnaarde, Belgium

Methanol-to-olefin (MTO) process

Search for alternative feedstock due to depleting oil reserves and increasing demand for base chemicals [1,2]

Methanol from any gasifiable carbon rich feedstock:

Natural gas
Coal
Biomass
→ Syngas → Methanol → Olefins

H-SAPO-34 as industrial catalyst

- High selectivity to light olefins: narrow 8-ring windows restrict diffusion of large molecules [3]
- Reaction mechanism:
  - Direct mechanisms → rejected [4]
  - Hydrocarbon pool mechanism with aromatics as co-catalyst [5]:
    >paring
    >side-chain

Influence of water on MTO

- Byproduct of methanol synthesis and MTO process
- Experimentally observed effects [6]:
  >slower catalyst deactivation
  >increased selectivity to light olefins

Objective

Study the influence of **water** on:
- adsorption
- proton mobility
- elementary reaction steps of the **side-chain mechanism**

via **ab initio molecular dynamics and metadynamics** by comparing **four cases**

Methodology

Ab initio molecular dynamics (AIMD) and metadynamics (MTD) [7]:
- Models:
  >fully periodic H-SAPO-34 catalyst
  >2 Brønsted acid sites (BAS) per unit cell
- revPBE functional with DFT-D3 dispersion correction
- Simulations at MTO reaction conditions: 623 K and 1 atm

Results

Variations in cell dimensions relative to an empty unit cell

Consistent with literature [8]:
- Anisotropic volume changes
- Largest variations along c-axis
- Volume expansion with MeOH and HMB
- Volume contraction with water

Relative stability of the intermediates
- HMMC not stable → protonated to heptaMB+
- Relative stability can be linked to the distance to the closest guest molecule
- Shorter distances and increased energy with higher water content

Framework deprotonation

low water content (Case 3)

high water content (Case 4)

Higher probability of framework deprotonation with higher water content

In case of a cationic intermediate, one of the BAS is deprotonated in the initial structure

Ethylene elimination

Conditions for low reaction barrier [5]:
- weakened C-C bond due to sp^3 hybridization
- formation of alkylbenzene-like complex
- assistance of water to facilitate access to the active site

1.51 ± 0.05 Å

1.62 ± 0.08 Å

Reactive paths to be determined via metadynamics

Conclusion

- Introduction of water increases framework deprotonation
- HMMC not found as a stable intermediate
- Methyl jumps occur spontaneously and are expected to have a low reaction barrier

References
[1] Hemelsoet, K., Van der Mynsbrugge, J., De Wispelaere, K., Waroquier, M. and Van Speybroeck, V., ChemPhysChem 14 (2013) 1526.
[2] Olsbye, U., Svelle, S., Bjørgen, M., Beato, P., Janssens, T.V.W., Joensen, F., Bordiga, S. and Lillerud, K.P., Angew. Chem. Int. Ed. 51 (2012) 5810.
[3] Chen, J.Q., Bozzano, A., Glover, B., Fuglerud, T. and Kvisle, S., Catal. Today 106 (2005) 103.
[4] Lesthaeghe, D., Van Speybroeck, V., Marin, G.B. and Waroquier, M., Ind. Eng. Chem. Res. 46 (2007) 8832.
[5] De Wispelaere, K., Hemelsoet, K., Waroquier, M. and Van Speybroeck, V., J. Catal. 305 (2013) 76.
[6] Taheri Najafabadi, A., Fatemi, S., Sohrabi, M. and Salmasi, M., J. Ind. Eng. Chem. 18 (2012) 29.
[7] Van Speybroeck, V., De Wispelaere, K., Van der Mynsbrugge, J., Vandichel, M., Hemelsoet, K. and Waroquier, M., Chem. Soc. Rev. 43 (2014) 7326.
[8] Wragg, D.S., Johnsen, R.E., Norby, P. and Fjellvåg, H., Micro. Meso. Mater. 134 (2010) 210.

Center for Molecular Modeling - http://molmod.ugent.be 2015 simon.bailleul@ugent.be

List of Figures

List of Tables

Bibliography

[1] R. W. Bentley, "Global oil & gas depletion: an overview," *Energy Policy*, vol. 30, pp. 189–205, Feb. 2002.

[2] A. Corma, S. Iborra, and A. Velty, "Chemical Routes for the Transformation of Biomass into Chemicals," *Chem. Rev.*, vol. 107, pp. 2411–2502, June 2007.

[3] C. Briens, J. Piskorz, and F. Berruti, "Biomass valorization for fuel and chemicals production - A review," *Int. J. Chem. React. Eng.*, vol. 6, p. R2, 2008. WOS:000256301700006.

[4] P. Spath and D. Dayton, "Preliminary Screening –Technical and Economic Assessment of Synthesis Gas to Fuels and Chemicals with Emphasis on the Potential for Biomass-Derived Syngas," Dec. 2003.

[5] S. Levine, G. Taylor, D. Arthur, and M. Tolleth, "Understanding crude oil and product markets," Sept. 2014.

[6] P. McKendry, "Energy production from biomass (part 3): gasification technologies," *Bioresource Technology*, vol. 83, pp. 55–63, May 2002.

[7] A. V. Bridgwater, "Renewable fuels and chemicals by thermal processing of biomass," *Chemical Engineering Journal*, vol. 91, pp. 87–102, Mar. 2003.

[8] T. Y. Ahmed, M. M. Ahmad, S. Yusup, A. Inayat, and Z. Khan, "Mathematical and computational approaches for design of biomass gasification for hydrogen production: A review," *Renewable and Sustainable Energy Reviews*, vol. 16, pp. 2304–2315, May 2012.

[9] P. Mondal, G. S. Dang, and M. O. Garg, "Syngas production through gasification and cleanup for downstream applications – Recent developments," *Fuel Processing Technology*, vol. 92, pp. 1395–1410, Aug. 2011.

[10] R. Warnecke, "Gasification of biomass: comparison of fixed bed and fluidized bed gasifier," *Biomass and Bioenergy*, vol. 18, pp. 489–497, June 2000.

[11] J. Zhang, R. Wu, G. Zhang, C. Yao, Y. Zhang, Y. Wang, and G. Xu, "Recent Studies on Chemical Engineering Fundamentals for Fuel Pyrolysis and Gasification in Dual Fluidized Bed," *Ind. Eng. Chem. Res.*, vol. 52, pp. 6283–6302, May 2013.

[12] C.-h. Liao, M. Summers, R. Seiser, R. Cattolica, and R. Herz, "Simulation of a pilot-scale dual-fluidized-bed gasifier for biomass," *Environ. Prog. Sustainable Energy*, vol. 33, pp. 732–736, Oct. 2014.

[13] F. Trippe, M. Fröhling, F. Schultmann, R. Stahl, and E. Henrich, "Techno-economic assessment of gasification as a process step within biomass-to-liquid (BtL) fuel and chemicals production," *Fuel Processing Technology*, vol. 92, pp. 2169–2184, Nov. 2011.

[14] S. Abrol and C. M. Hilton, "Modeling, simulation and advanced control of methanol production from variable synthesis gas feed," *Computers & Chemical Engineering*, vol. 40, pp. 117–131, May 2012.

[15] F. J. Keil, "Methanol-to-hydrocarbons: process technology," *Microporous and Mesoporous Materials*, vol. 29, pp. 49–66, June 1999.

[16] U. Olsbye, S. Svelle, M. Bjørgen, P. Beato, T. V. W. Janssens, F. Joensen, S. Bordiga, and K. P. Lillerud, "Conversion of Methanol to Hydrocarbons: How Zeolite Cavity and Pore Size Controls Product Selectivity," *Angew. Chem. Int. Ed.*, vol. 51, pp. 5810–5831, June 2012.

[17] S. A. Tabak and S. Yurchak, "Conversion of methanol over ZSM-5 to fuels and chemicals," *Catalysis Today*, vol. 6, pp. 307–327, Jan. 1990.

[18] J. Q. Chen, A. Bozzano, B. Glover, T. Fuglerud, and S. Kvisle, "Recent advancements in ethylene and propylene production using the UOP/Hydro MTO process," *Catalysis Today*, vol. 106, no. 1–4, pp. 103–107, 2005.

[19] A. Taheri Najafabadi, S. Fatemi, M. Sohrabi, and M. Salmasi, "Kinetic modeling and optimization of the operating condition of MTO process on SAPO-34 catalyst," *Journal of Industrial and Engineering Chemistry*, vol. 18, pp. 29–37, Jan. 2012.

[20] J. F. Haw, W. Song, D. M. Marcus, and J. B. Nicholas, "The Mechanism of Methanol to Hydrocarbon Catalysis," *Acc. Chem. Res.*, vol. 36, no. 5, pp. 317–326, 2003.

[21] K. Hemelsoet, J. Van der Mynsbrugge, K. De Wispelaere, M. Waroquier, and V. Van Speybroeck, "Unraveling the Reaction Mechanisms Governing Methanol-to-Olefins Catalysis by Theory and Experiment," *ChemPhysChem*, vol. 14, no. 8, pp. 1526–1545, 2013.

[22] V. V. Speybroeck, K. D. Wispelaere, J. V. d. Mynsbrugge, M. Vandichel, K. Hemelsoet, and M. Waroquier, “First principle chemical kinetics in zeolites: the methanol-to-olefin process as a case study,” *Chem. Soc. Rev.*, vol. 43, no. 21, pp. 7326–7357, 2014.

[23] M. Stöcker, “Methanol-to-hydrocarbons: catalytic materials and their behavior,” *Microporous and Mesoporous Materials*, vol. 29, pp. 3–48, June 1999.

[24] D. Lesthaeghe, V. Van Speybroeck, G. B. Marin, and M. Waroquier, “Understanding the Failure of Direct C–C Coupling in the Zeolite-Catalyzed Methanol-to-Olefin Process,” *Angewandte Chemie International Edition*, vol. 45, pp. 1714–1719, Mar. 2006.

[25] D. Lesthaeghe, V. Van Speybroeck, G. B. Marin, and M. Waroquier, “The Rise and Fall of Direct Mechanisms in Methanol-to-Olefin Catalysis: An Overview of Theoretical Contributions,” *Ind. Eng. Chem. Res.*, vol. 46, pp. 8832–8838, Dec. 2007.

[26] R. M. Dessau and R. B. LaPierre, “On the mechanism of methanol conversion to hydrocarbons over HZSM-5,” *Journal of Catalysis*, vol. 78, pp. 136–141, Nov. 1982.

[27] R. M. Dessau, “On the H-ZSM-5 catalyzed formation of ethylene from methanol or higher olefins,” *Journal of Catalysis*, vol. 99, pp. 111–116, May 1986.

[28] T. Mole, G. Bett, and D. Seddon, “Conversion of methanol to hydrocarbons over ZSM-5 zeolite: An examination of the role of aromatic hydrocarbons using 13carbon- and deuterium-labeled feeds,” *Journal of Catalysis*, vol. 84, pp. 435–445, Dec. 1983.

[29] B. E. Langner, “Reactions of methanol on zeolites with different pore structures,” *Applied Catalysis*, vol. 2, pp. 289–302, Apr. 1982.

[30] I. M. Dahl and S. Kolboe, “On the Reaction-Mechanism for Propene Formation in the Mto Reaction Over Sapo-34,” *Catal. Lett.*, vol. 20, no. 3-4, pp. 329–336, 1993. WOS:A1993LU35400017.

[31] I. M. Dahl and S. Kolboe, “On the Reaction Mechanism for Hydrocarbon Formation from Methanol over SAPO-34: I. Isotopic Labeling Studies of the Co-Reaction of Ethene and Methanol,” *Journal of Catalysis*, vol. 149, pp. 458–464, Oct. 1994.

[32] I. M. Dahl and S. Kolboe, “On the Reaction Mechanism for Hydrocarbon Formation from Methanol over SAPO-34: 2. Isotopic Labeling Studies of the Co-reaction of Propene and Methanol,” *Journal of Catalysis*, vol. 161, pp. 304–309, June 1996.

[33] Ø. Mikkelsen, P. O. Rønning, and S. Kolboe, "Use of isotopic labeling for mechanistic studies of the methanol-to-hydrocarbons reaction. Methylation of toluene with methanol over H-ZSM-5, H-mordenite and H-beta," *Microporous and Mesoporous Materials*, vol. 40, pp. 95–113, Nov. 2000.

[34] B. Arstad and S. Kolboe, "Methanol-to-hydrocarbons reaction over SAPO-34. Molecules confined in the catalyst cavities at short time on stream," *Catalysis Letters*, vol. 71, pp. 209–212, Feb. 2001.

[35] B. Arstad and S. Kolboe, "The Reactivity of Molecules Trapped within the SAPO-34 Cavities in the Methanol-to-Hydrocarbons Reaction," *J. Am. Chem. Soc.*, vol. 123, no. 33, pp. 8137–8138, 2001.

[36] J. F. Haw and D. M. Marcus, "Well-defined (supra)molecular structures in zeolite methanol-to-olefin catalysis," *Top Catal*, vol. 34, pp. 41–48, May 2005.

[37] W. Song, D. M. Marcus, H. Fu, J. O. Ehresmann, and J. F. Haw, "An Oft-Studied Reaction That May Never Have Been: Direct Catalytic Conversion of Methanol or Dimethyl Ether to Hydrocarbons on the Solid Acids HZSM-5 or HSAPO-34," *J. Am. Chem. Soc.*, vol. 124, no. 15, pp. 3844–3845, 2002.

[38] Y. Jiang, W. Wang, V. R. Reddy Marthala, J. Huang, B. Sulikowski, and M. Hunger, "Effect of organic impurities on the hydrocarbon formation via the decomposition of surface methoxy groups on acidic zeolite catalysts," *Journal of Catalysis*, vol. 238, pp. 21–27, Feb. 2006.

[39] M. Vandichel, D. Lesthaeghe, J. V. d. Mynsbrugge, M. Waroquier, and V. Van Speybroeck, "Assembly of cyclic hydrocarbons from ethene and propene in acid zeolite catalysis to produce active catalytic sites for MTO conversion," *Journal of Catalysis*, vol. 271, pp. 67–78, Apr. 2010.

[40] S. R. Blaszkowski and R. A. van Santen, "Theoretical Study of C–C Bond Formation in the Methanol-to-Gasoline Process," *J. Am. Chem. Soc.*, vol. 119, no. 21, pp. 5020–5027, 1997.

[41] N. Tajima, T. Tsuneda, F. Toyama, and K. Hirao, "A New Mechanism for the First Carbon–Carbon Bond Formation in the MTG Process: A Theoretical Study," *J. Am. Chem. Soc.*, vol. 120, no. 32, pp. 8222–8229, 1998.

[42] D. Lesthaeghe, V. Van Speybroeck, G. B. Marin, and M. Waroquier, "What role do oxonium ions and oxonium ylides play in the ZSM-5 catalysed methanol-to-olefin process?," *Chemical Physics Letters*, vol. 417, pp. 309–315, Jan. 2006.

[43] C. Lo, C. A. Giurumescu, R. Radhakrishnan, and B. L. Trout, "Methanol coupling in the zeolite chabazite studied via Car-Parrinello molecular dynamics," *Mol. Phys.*, vol. 102, pp. 281–288, Feb. 2004. WOS:000220894300007.

[44] C. S. Lo, R. Radhakrishnan, and B. L. Trout, "Application of transition path sampling methods in catalysis: A new mechanism for bond formation in the methanol coupling reaction in chabazite," *Catalysis Today*, vol. 105, pp. 93–105, July 2005.

[45] N. Y. Chen and W. J. Reagan, "Evidence of autocatalysis in methanol to hydrocarbon reactions over zeolite catalysts," *Journal of Catalysis*, vol. 59, pp. 123–129, Aug. 1979.

[46] S. Svelle, P. O. Rønning, and S. Kolboe, "Kinetic studies of zeolite-catalyzed methylation reactions: 1. Coreaction of [12c]ethene and [13c]methanol," *Journal of Catalysis*, vol. 224, pp. 115–123, May 2004.

[47] S. Svelle, P. O. Rønning, U. Olsbye, and S. Kolboe, "Kinetic studies of zeolite-catalyzed methylation reactions. Part 2. Co-reaction of [12c]propene or [12c]n-butene and [13c]methanol," *Journal of Catalysis*, vol. 234, pp. 385–400, Sept. 2005.

[48] S. Svelle, F. Joensen, J. Nerlov, U. Olsbye, K.-P. Lillerud, S. Kolboe, and M. Bjørgen, "Conversion of Methanol into Hydrocarbons over Zeolite H-ZSM-5: Ethene Formation Is Mechanistically Separated from the Formation of Higher Alkenes," *J. Am. Chem. Soc.*, vol. 128, no. 46, pp. 14770–14771, 2006.

[49] S. Teketel, U. Olsbye, K.-P. Lillerud, P. Beato, and S. Svelle, "Selectivity control through fundamental mechanistic insight in the conversion of methanol to hydrocarbons over zeolites," *Microporous and Mesoporous Materials*, vol. 136, pp. 33–41, Dec. 2010.

[50] R. F. Sullivan, C. J. Egan, G. E. Langlois, and R. P. Sieg, "A New Reaction That Occurs in the Hydrocracking of Certain Aromatic Hydrocarbons," *J. Am. Chem. Soc.*, vol. 83, no. 5, pp. 1156–1160, 1961.

[51] M. Bjørgen, U. Olsbye, D. Petersen, and S. Kolboe, "The methanol-to-hydrocarbons reaction: insight into the reaction mechanism from [12c]benzene and [13c]methanol coreactions over zeolite H-beta," *Journal of Catalysis*, vol. 221, pp. 1–10, Jan. 2004.

[52] T. Mole, J. A. Whiteside, and D. Seddon, "Aromatic co-catalysis of methanol conversion over zeolite catalysts," *Journal of Catalysis*, vol. 82, pp. 261–266, Aug. 1983.

[53] A. Sassi, M. A. Wildman, H. J. Ahn, P. Prasad, J. B. Nicholas, and J. F. Haw, “Methylbenzene Chemistry on Zeolite HBeta: Multiple Insights into Methanol-to-Olefin Catalysis,” *J. Phys. Chem. B*, vol. 106, no. 9, pp. 2294–2303, 2002.

[54] A. Sassi, M. A. Wildman, and J. F. Haw, “Reactions of Butylbenzene Isomers on Zeolite HBeta: Methanol-to-Olefins Hydrocarbon Pool Chemistry and Secondary Reactions of Olefins,” *J. Phys. Chem. B*, vol. 106, no. 34, pp. 8768–8773, 2002.

[55] D. Lesthaeghe, A. Horré, M. Waroquier, G. B. Marin, and V. Van Speybroeck, “Theoretical Insights on Methylbenzene Side-Chain Growth in ZSM-5 Zeolites for Methanol-to-Olefin Conversion,” *Chem. Eur. J.*, vol. 15, no. 41, pp. 10803–10808, 2009.

[56] S. Svelle, M. Visur, U. Olsbye, Saepurahman, and M. Bjørgen, “Mechanistic Aspects of the Zeolite Catalyzed Methylation of Alkenes and Aromatics with Methanol: A Review,” *Top Catal*, vol. 54, pp. 897–906, Sept. 2011.

[57] V. Van Speybroeck, J. Van der Mynsbrugge, M. Vandichel, K. Hemelsoet, D. Lesthaeghe, A. Ghysels, G. B. Marin, and M. Waroquier, “First Principle Kinetic Studies of Zeolite-Catalyzed Methylation Reactions,” *J. Am. Chem. Soc.*, vol. 133, pp. 888–899, Feb. 2011.

[58] J. Van der Mynsbrugge, M. Visur, U. Olsbye, P. Beato, M. Bjørgen, V. Van Speybroeck, and S. Svelle, “Methylation of benzene by methanol: Single-site kinetics over H-ZSM-5 and H-beta zeolite catalysts,” *Journal of Catalysis*, vol. 292, pp. 201–212, Aug. 2012.

[59] S. L. C. Moors, K. De Wispelaere, J. Van der Mynsbrugge, M. Waroquier, and V. Van Speybroeck, “Molecular Dynamics Kinetic Study on the Zeolite-Catalyzed Benzene Methylation in ZSM-5,” *ACS Catal.*, vol. 3, no. 11, pp. 2556–2567, 2013.

[60] W. Song, H. Fu, and J. F. Haw, “Supramolecular Origins of Product Selectivity for Methanol-to-Olefin Catalysis on HSAPO-34,” *J. Am. Chem. Soc.*, vol. 123, no. 20, pp. 4749–4754, 2001.

[61] V. Van Speybroeck, K. Hemelsoet, K. De Wispelaere, Q. Qian, J. Van der Mynsbrugge, B. De Sterck, B. M. Weckhuysen, and M. Waroquier, “Mechanistic Studies on Chabazite-Type Methanol-to-Olefin Catalysts: Insights from Time-Resolved UV/Vis Microspectroscopy Combined with Theoretical Simulations,” *ChemCatChem*, vol. 5, pp. 173–184, Jan. 2013.

[62] C.-M. Wang, Y.-D. Wang, H.-X. Liu, Z.-K. Xie, and Z.-P. Liu, “Catalytic activity and selectivity of methylbenzenes in HSAPO-34 catalyst for the methanol-to-olefins conversion from first principles,” *Journal of Catalysis*, vol. 271, pp. 386–391, May 2010.

[63] C.-M. Wang, Y.-D. Wang, Z.-K. Xie, and Z.-P. Liu, "Methanol to Olefin Conversion on HSAPO-34 Zeolite from Periodic Density Functional Theory Calculations: A Complete Cycle of Side Chain Hydrocarbon Pool Mechanism," *J. Phys. Chem. C*, vol. 113, no. 11, pp. 4584–4591, 2009.

[64] K. De Wispelaere, K. Hemelsoet, M. Waroquier, and V. Van Speybroeck, "Complete low-barrier side-chain route for olefin formation during methanol conversion in H-SAPO-34," *Journal of Catalysis*, vol. 305, pp. 76–80, 2013.

[65] D. M. McCann, D. Lesthaeghe, P. W. Kletnieks, D. R. Guenther, M. J. Hayman, V. Van Speybroeck, M. Waroquier, and J. F. Haw, "A Complete Catalytic Cycle for Supramolecular Methanol-to-Olefins Conversion by Linking Theory with Experiment," *Angewandte Chemie International Edition*, vol. 47, pp. 5179–5182, June 2008.

[66] M. Bjørgen, F. Joensen, K.-P. Lillerud, U. Olsbye, and S. Svelle, "The mechanisms of ethene and propene formation from methanol over high silica H-ZSM-5 and H-beta," *Catalysis Today*, vol. 142, pp. 90–97, Apr. 2009.

[67] Z.-M. Cui, Q. Liu, W.-G. Song, and L.-J. Wan, "Insights into the Mechanism of Methanol-to-Olefin Conversion at Zeolites with Systematically Selected Framework Structures," *Angewandte Chemie International Edition*, vol. 45, no. 39, pp. 6512–6515, 2006.

[68] B. P. C. Hereijgers, F. Bleken, M. H. Nilsen, S. Svelle, K.-P. Lillerud, M. Bjørgen, B. M. Weckhuysen, and U. Olsbye, "Product shape selectivity dominates the Methanol-to-Olefins (MTO) reaction over H-SAPO-34 catalysts," *Journal of Catalysis*, vol. 264, no. 1, pp. 77–87, 2009.

[69] "Database of Zeolite Structures; url: http://www.iza-structure.org/databases/."

[70] D. S. Wragg, R. E. Johnsen, P. Norby, and H. Fjellvåg, "The adsorption of methanol and water on SAPO-34: in situ and ex situ X-ray diffraction studies," *Microporous and Mesoporous Materials*, vol. 134, no. 1–3, pp. 210–215, 2010.

[71] D. S. Wragg, M. G. O'Brien, F. L. Bleken, M. Di Michiel, U. Olsbye, and H. Fjellvåg, "Watching the Methanol-to-Olefin Process with Time- and Space-Resolved High-Energy Operando X-ray Diffraction," *Angew. Chem. Int. Ed.*, vol. 51, pp. 7956–7959, Aug. 2012.

[72] M. Zokaie, D. S. Wragg, A. Grønvold, T. Fuglerud, J. H. Cavka, K. P. Lillerud, and O. Swang, "Unit cell expansion upon coke formation in a SAPO-34 catalyst: A combined experimental and computational study," *Microporous and Mesoporous Materials*, vol. 165, pp. 1–5, Jan. 2013.

[73] D. Chen, K. Moljord, and A. Holmen, “A methanol to olefins review: Diffusion, coke formation and deactivation on SAPO type catalysts,” *Microporous and Mesoporous Materials*, vol. 164, pp. 239–250, Dec. 2012.

[74] K. Hemelsoet, Q. Qian, T. De Meyer, K. De Wispelaere, B. De Sterck, B. M. Weckhuysen, M. Waroquier, and V. Van Speybroeck, “Identification of Intermediates in Zeolite-Catalyzed Reactions by In Situ UV/Vis Microspectroscopy and a Complementary Set of Molecular Simulations,” *Chem. Eur. J.*, vol. 19, pp. 16595–16606, Dec. 2013.

[75] K. Hemelsoet, A. Nollet, V. Van Speybroeck, and M. Waroquier, “Theoretical Simulations Elucidate the Role of Naphthalenic Species during Methanol Conversion within H-SAPO-34,” *Chem. Eur. J.*, vol. 17, pp. 9083–9093, Aug. 2011.

[76] F. Bleken, M. Bjørgen, L. Palumbo, S. Bordiga, S. Svelle, K.-P. Lillerud, and U. Olsbye, “The Effect of Acid Strength on the Conversion of Methanol to Olefins Over Acidic Microporous Catalysts with the CHA Topology,” *Top Catal*, vol. 52, pp. 218–228, Apr. 2009.

[77] Q. Qian, J. Ruiz-Martínez, M. Mokhtar, A. M. Asiri, S. A. Al-Thabaiti, S. N. Basahel, H. E. van der Bij, J. Kornatowski, and B. M. Weckhuysen, “Single-Particle Spectroscopy on Large SAPO-34 Crystals at Work: Methanol-to-Olefin versus Ethanol-to-Olefin Processes,” *Chem. Eur. J.*, vol. 19, pp. 11204–11215, Aug. 2013.

[78] “Single-Particle Spectroscopy of Alcohol-to-Olefins over SAPO-34 at Different Reaction Stages: Crystal Accessibility and Hydrocarbons Reactivity,” vol. 6.

[79] Q. Qian, C. Vogt, M. Mokhtar, A. M. Asiri, S. A. Al-Thabaiti, S. N. Basahel, J. Ruiz-Martínez, and B. M. Weckhuysen, “Combined Operando UV/Vis/IR Spectroscopy Reveals the Role of Methoxy and Aromatic Species during the Methanol-to-Olefins Reaction over H-SAPO-34,” *ChemCatChem*, pp. n/a–n/a, Oct. 2014.

[80] J. Van der Mynsbrugge, S. L. C. Moors, K. De Wispelaere, and V. Van Speybroeck, “Insight into the Formation and Reactivity of Framework-Bound Methoxide Species in H-ZSM-5 from Static and Dynamic Molecular Simulations,” *ChemCatChem*, vol. 6, pp. 1906–1918, July 2014.

[81] H. Schulz, “”Coking” of zeolites during methanol conversion: Basic reactions of the MTO-, MTP- and MTG processes,” *Catalysis Today*, vol. 154, pp. 183–194, Sept. 2010.

[82] M. Bjørgen, S. Svelle, F. Joensen, J. Nerlov, S. Kolboe, F. Bonino, L. Palumbo, S. Bordiga, and U. Olsbye, “Conversion of methanol to hydrocarbons over zeolite

H-ZSM-5: On the origin of the olefinic species," *Journal of Catalysis*, vol. 249, pp. 195–207, July 2007.

[83] S. Svelle, U. Olsbye, F. Joensen, and M. Bjørgen, "Conversion of Methanol to Alkenes over Medium- and Large-Pore Acidic Zeolites: Steric Manipulation of the Reaction Intermediates Governs the Ethene/Propene Product Selectivity," *J. Phys. Chem. C*, vol. 111, no. 49, pp. 17981–17984, 2007.

[84] D. Lesthaeghe, B. De Sterck, V. Van Speybroeck, G. B. Marin, and M. Waroquier, "Zeolite Shape-Selectivity in the gem-Methylation of Aromatic Hydrocarbons," *Angewandte Chemie International Edition*, vol. 46, no. 8, pp. 1311–1314, 2007.

[85] S. Teketel, W. Skistad, S. Benard, U. Olsbye, K. P. Lillerud, P. Beato, and S. Svelle, "Shape Selectivity in the Conversion of Methanol to Hydrocarbons: The Catalytic Performance of One-Dimensional 10-Ring Zeolites: ZSM-22, ZSM-23, ZSM-48, and EU-1," *ACS Catal.*, vol. 2, no. 1, pp. 26–37, 2011.

[86] W. Dai, X. Wang, G. Wu, N. Guan, M. Hunger, and L. Li, "Methanol-to-Olefin Conversion on Silicoaluminophosphate Catalysts: Effect of Brønsted Acid Sites and Framework Structures," *ACS Catal.*, vol. 1, no. 4, pp. 292–299, 2011.

[87] Y. Kumita, J. Gascon, E. Stavitski, J. A. Moulijn, and F. Kapteijn, "Shape selective methanol to olefins over highly thermostable DDR catalysts," *Applied Catalysis A: General*, vol. 391, pp. 234–243, Jan. 2011.

[88] F. Zhou, P. Tian, Z. Liu, G. Liu, F. Chang, and J. Li, "Synthesis of ZSM-34 and Its Catalytic Properties in Methanol-to-Olefins Reaction," *Chinese Journal of Catalysis*, vol. 28, pp. 817–822, Sept. 2007.

[89] L. Zhang, C. Yang, X. Meng, B. Xie, L. Wang, L. Ren, S. Ma, and F.-S. Xiao, "Organotemplate-Free Syntheses of ZSM-34 Zeolite and Its Heteroatom-Substituted Analogues with Good Catalytic Performance," *Chem. Mater.*, vol. 22, no. 10, pp. 3099–3107, 2010.

[90] X. Yin, D. Y. C. Leung, J. Chang, J. Wang, Y. Fu, and C. Wu, "Characteristics of the Synthesis of Methanol Using Biomass-Derived Syngas," *Energy Fuels*, vol. 19, pp. 305–310, Jan. 2005.

[91] S. Bordiga, L. Regli, C. Lamberti, A. Zecchina, M. Bjørgen, and K. P. Lillerud, "FTIR Adsorption Studies of H2O and CH3OH in the Isostructural H-SSZ-13 and H-SAPO-34: Formation of H-Bonded Adducts and Protonated Clusters," *J. Phys. Chem. B*, vol. 109, pp. 7724–7732, Apr. 2005.

[92] L. Marchese, J. Chen, P. A. Wright, and J. M. Thomas, “Formation of hydronium at the Broensted site in SAPO-34 catalysts,” *J. Phys. Chem.*, vol. 97, pp. 8109–8112, Aug. 1993.

[93] L. Smith, A. K. Cheetham, R. E. Morris, L. Marchese, J. M. Thomas, P. A. Wright, and J. Chen, “On the Nature of Water Bound to a Solid Acid Catalyst,” *Science*, vol. 271, pp. 799–802, Feb. 1996.

[94] V. Termath, F. Haase, J. Sauer, J. Hutter, and M. Parrinello, “Understanding the Nature of Water Bound to Solid Acid Surfaces. Ab Initio Simulation on HSAPO-34,” *J. Am. Chem. Soc.*, vol. 120, pp. 8512–8516, Aug. 1998.

[95] A. Zheng, B. Han, B. Li, S.-B. Liu, and F. Deng, “Enhancement of BrÃ¸nsted acidity in zeolitic catalysts due to an intermolecular solvent effect in confined micropores,” *Chem. Commun.*, vol. 48, pp. 6936–6938, June 2012.

[96] K. Chen, J. Damron, C. Pearson, D. Resasco, L. Zhang, and J. L. White, “Zeolite Catalysis: Water Can Dramatically Increase or Suppress Alkane C–H Bond Activation,” *ACS Catal.*, vol. 4, pp. 3039–3044, Sept. 2014.

[97] X. Wu and R. G. Anthony, “Effect of feed composition on methanol conversion to light olefins over SAPO-34,” *Applied Catalysis A: General*, vol. 218, pp. 241–250, Sept. 2001.

[98] S. M. Alwahabi and G. F. Froment, “Single Event Kinetic Modeling of the Methanol-to-Olefins Process on SAPO-34,” *Ind. Eng. Chem. Res.*, vol. 43, no. 17, pp. 5098–5111, 2004.

[99] A. J. Marchi and G. F. Froment, “Catalytic conversion of methanol to light alkenes on SAPO molecular sieves,” *Applied Catalysis*, vol. 71, pp. 139–152, Apr. 1991.

[100] K. Wondergem, J. R. Martinez, and B. M. Weckhuysen, *The Effect of Water on Methanol-to-Olefins Reactions Studied by Advanced in situ Microspectroscopy.* PhD thesis, Utrecht University, Jan. 2014.

[101] V. Van Speybroeck, “Course notes molecular modeling of industrial processes,” 2014.

[102] P. Hohenberg and W. Kohn, “Inhomogeneous Electron Gas,” *Phys. Rev.*, vol. 136, pp. B864–B871, Nov. 1964.

[103] T. Deconinck, V. Van Speybroeck, K. Hemelsoet, K. De Wispelaere, S. L. C. Moors, and J. Van der Mynsbrugge, *Dynamic ab initio study towards new hydro carbon pool cycles for MTO-conversion in H-SAPO-5.* PhD thesis, Universiteit Gent, 2014.

[104] J. P. Perdew, K. Burke, and M. Ernzerhof, "Generalized Gradient Approximation Made Simple," *Phys. Rev. Lett.*, vol. 77, pp. 3865–3868, Oct. 1996.

[105] S. Grimme, J. Antony, S. Ehrlich, and H. Krieg, "A consistent and accurate ab initio parametrization of density functional dispersion correction (DFT-D) for the 94 elements H-Pu," *The Journal of Chemical Physics*, vol. 132, p. 154104, Apr. 2010.

[106] G. Gece, "The use of quantum chemical methods in corrosion inhibitor studies," *Corrosion Science*, vol. 50, pp. 2981–2992, Nov. 2008.

[107] C. Dykstra, G. Frenking, K. Kim, and G. Scuseria, *Theory and Applications of Computational Chemistry: The First Forty Years.* Elsevier, Oct. 2011.

[108] A. Alparone, V. Librando, and Z. Minniti, "Validation of semiempirical PM6 method for the prediction of molecular properties of polycyclic aromatic hydrocarbons and fullerenes," *Chemical Physics Letters*, vol. 460, pp. 151–154, July 2008.

[109] G. Lippert, J. Hutter, and M. Parrinello, "The Gaussian and augmented-plane-wave density functional method for ab initio molecular dynamics simulations," *Theor Chem Acc*, vol. 103, pp. 124–140, Dec. 1999.

[110] J. VandeVondele, M. Krack, F. Mohamed, M. Parrinello, T. Chassaing, and J. Hutter, "Quickstep: Fast and accurate density functional calculations using a mixed Gaussian and plane waves approach," *Computer Physics Communications*, vol. 167, pp. 103–128, Apr. 2005.

[111] I. L. C. Buurmans and B. M. Weckhuysen, "Heterogeneities of individual catalyst particles in space and time as monitored by spectroscopy," *Nature Chemistry*, vol. 4, pp. 873–86, Nov. 2012.

[112] R. Car and M. Parrinello, "Unified Approach for Molecular Dynamics and Density-Functional Theory," *Phys. Rev. Lett.*, vol. 55, pp. 2471–2474, Nov. 1985.

[113] T. D. Kühne, M. Krack, F. R. Mohamed, and M. Parrinello, "Efficient and Accurate Car-Parrinello-like Approach to Born-Oppenheimer Molecular Dynamics," *Phys. Rev. Lett.*, vol. 98, p. 066401, Feb. 2007.

[114] D. Frenkel and B. Smit, *Understanding Molecular Simulation: From Algorithms to Applications.* Academic Press, Oct. 2001.

[115] G. Bussi, D. Donadio, and M. Parrinello, "Canonical sampling through velocity rescaling," *The Journal of Chemical Physics*, vol. 126, p. 014101, Jan. 2007.

[116] S. Nosé, “A molecular dynamics method for simulations in the canonical ensemble,” *Molecular Physics*, vol. 52, pp. 255–268, June 1984.

[117] S. Nosé, “A unified formulation of the constant temperature molecular dynamics methods,” *The Journal of Chemical Physics*, vol. 81, pp. 511–519, July 1984.

[118] G. J. Martyna, D. J. Tobias, and M. L. Klein, “Constant pressure molecular dynamics algorithms,” *The Journal of Chemical Physics*, vol. 101, pp. 4177–4189, Sept. 1994.

[119] T. Bučko, L. Benco, O. Dubay, C. Dellago, and J. Hafner, “Mechanism of alkane dehydrogenation catalyzed by acidic zeolites: Ab initio transition path sampling,” *The Journal of Chemical Physics*, vol. 131, p. 214508, Dec. 2009.

[120] L. Benco, T. Bucko, and J. Hafner, “Dehydrogenation of propane over ZnMOR. Static and dynamic reaction energy diagram,” *Journal of Catalysis*, vol. 277, pp. 104–116, Jan. 2011.

[121] T. Bučko, L. Benco, J. Hafner, and J. G. Ángyán, “Monomolecular cracking of propane over acidic chabazite: An ab initio molecular dynamics and transition path sampling study,” *Journal of Catalysis*, vol. 279, pp. 220–228, Apr. 2011.

[122] A. Laio and M. Parrinello, “Escaping free-energy minima,” *PNAS*, vol. 99, pp. 12562–12566, Oct. 2002.

[123] M. Iannuzzi, A. Laio, and M. Parrinello, “Efficient Exploration of Reactive Potential Energy Surfaces Using Car-Parrinello Molecular Dynamics,” *Phys. Rev. Lett.*, vol. 90, p. 238302, June 2003.

[124] T. Bucko, “Ab initio calculations of free-energy reaction barriers,” *J. Phys.: Condens. Matter*, vol. 20, p. 064211, Feb. 2008.

[125] B. Ensing, A. Laio, M. Parrinello, and M. L. Klein, “A Recipe for the Computation of the Free Energy Barrier and the Lowest Free Energy Path of Concerted Reactions,” *J. Phys. Chem. B*, vol. 109, pp. 6676–6687, Apr. 2005.

[126] G. Lippert, J. Hutter, and M. Parrinello, “A hybrid Gaussian and plane wave density functional scheme,” *Molecular Physics*, vol. 92, pp. 477–488, Oct. 1997.

[127] K. Yang, J. Zheng, Y. Zhao, and D. G. Truhlar, “Tests of the RPBE, revPBE, τ-HCTHhyb, ωB97x-D, and MOHLYP density functional approximations and 29 others against representative databases for diverse bond energies and barrier heights in catalysis,” *The Journal of Chemical Physics*, vol. 132, p. 164117, Apr. 2010.

[128] S. Goedecker, M. Teter, and J. Hutter, "Separable dual-space Gaussian pseudopotentials," *Phys. Rev. B*, vol. 54, pp. 1703–1710, July 1996.

[129] W. Humphrey, A. Dalke, and K. Schulten, "VMD: Visual molecular dynamics," *Journal of Molecular Graphics*, vol. 14, pp. 33–38, Feb. 1996.

[130] N. E. R. Zimmermann, S. Jakobtorweihen, E. Beerdsen, B. Smit, and F. J. Keil, "In-Depth Study of the Influence of Host–Framework Flexibility on the Diffusion of Small Gas Molecules in One-Dimensional Zeolitic Pore Systems," *J. Phys. Chem. C*, vol. 111, pp. 17370–17381, Nov. 2007.

[131] K. De Wispelaere, B. Ensing, A. Ghysels, E. J. Meijer, and V. Van Speybroeck, "Complex Reaction Environments and Competing Reaction Mechanisms in Zeolite Catalysis: Insights from Advanced Molecular Dynamics," *Chem. Eur. J.*, pp. n/a–n/a, 2015.

[132] A. Laio and F. L. Gervasio, "Metadynamics: a method to simulate rare events and reconstruct the free energy in biophysics, chemistry and material science," *Rep. Prog. Phys.*, vol. 71, p. 126601, Dec. 2008.

[133] I.-C. Lin and M. E. Tuckerman, "Enhanced Conformational Sampling of Peptides via Reduced Side-Chain and Solvent Masses," *J. Phys. Chem. B*, vol. 114, pp. 15935–15940, Dec. 2010.

[134] B. Arstad, S. Kolboe, and O. Swang, "Theoretical Study of the Heptamethylbenzenium Ion. Intramolecular Isomerizations and C2, C3, C4 Alkene Elimination," *J. Phys. Chem. A*, vol. 109, pp. 8914–8922, Oct. 2005.

[135] M. Ceriotti, J. Cuny, M. Parrinello, and D. E. Manolopoulos, "Nuclear quantum effects and hydrogen bond fluctuations in water," *PNAS*, vol. 110, pp. 15591–15596, Sept. 2013.

[136] M. Ceriotti, J. More, and D. E. Manolopoulos, "i-PI: A Python interface for ab initio path integral molecular dynamics simulations," *Computer Physics Communications*, vol. 185, pp. 1019–1026, Mar. 2014.